Bernhard Reithofer BSc

A CONCEPT FOR A MINITURIZED 3D TIME-OF-FLIGHT (TOF) CAMERA FOR USE IN MOBILE PHONES AND TABLETS

MASTER'S THESIS

to achieve the university degree of

Diplom-Ingenieur

Master's degree program: Electrical Engineering

submitted to

Graz University of Technology

Supervisor

Univ.-Prof. Dipl.-Ing. Dr.techn. Bernd Deutschmann

Institute of Electronics

Dipl.-Ing. Mario Manninger
ams AG

Graz, September 2015

AFFIDAVIT

I declare that I have authored this thesis independently, that I have not used other than the declared sources/resources, and that I have explicitly indicated all material which has been quoted either literally or by content from the sources used. The text document uploaded to TUGRAZonline is identical to the present master‘s thesis dissertation.

Date

Signature

Abstract

The ability to capture the world around of us in three-dimensional perspective has always been fascinating for humankind. In the recent years, a technology called Time-of-Flight (TOF) has reached the attention of engineers. Thanks to its unique possibility of high integration into dedicated CMOS process nodes, high performance and low cost imagers have been proposed in the last years. Because of this trend, immense opportunities are grown in several fields of application like in customer electronics, industrial, automotive, health care, and entertainment.

The work in hand provides a standalone view on Time-of-Flight from the engineer's as well as from the marketing perspective and shows the capability of this exiting technology. State-of-the-Art TOF imagers are being reviewed and a concept for a miniaturized TOF camera for use in mobile phones and tablets is proposed. Because of its importance in product design, one chapter is dedicated to electromagnetic interferences (EMI). Furthermore, this thesis focuses on the economic perspective of TOF product development.

To my beloved wife Marizela and son Tarik and my loving parents,

Table of Contents

1 Introduction ... 1
1.1 Motivation ... 1
1.2 Fields of Application for Time-of-Flight Image Sensors ... 3
1.3 Time-of-Flight System ... 4
1.4 Classification of Solid-State TOF Image Sensors ... 6
1.5 Optical Modulation Techniques ... 7
1.6 TOF Measurement Techniques ... 8
1.6.1 Direct TOF (D-TOF) ... 8
1.6.2 Indirect TOF (I-TOF) ... 9
1.7 Pixel Photodetector Principles ... 10
1.7.1 SPAD based Detectors ... 10
1.7.1.1 Photon Detection Probability (PDP) ... 13
1.7.1.2 Dead Time ... 14
1.7.1.3 Noise Sources in SPAD ... 15
1.7.1.4 Timing Jitter ... 15
1.7.1.5 Trade-off in SPAD Operation and Design ... 16
1.7.2 In-Pixel Photo-Mixing Devices ... 17
1.7.2.1 Demodulation Contrast ... 19
1.7.2.2 Fill Factor ... 19
1.7.2.3 Quantum Efficiency ... 19
1.7.2.4 Responsivity ... 19
1.7.2.5 Charge-Coupled Device (CCD) ... 20
1.7.2.6 Photonic Mixer Devices (PMD) ... 21
1.7.2.7 Current Assisted Photonic Demodulators (CAPD) ... 22
1.7.2.8 Pinned-Photodiode Demodulators ... 23
2 State-of-the-Art TOF Image Sensors ... 26
2.1 Literature Research on TOF Sensors ... 26
2.1.1 SPAD based Sensor Solutions ... 26
2.1.2 In Pixel based Sensor solutions ... 32
2.2 ST Microelectronics VL6180 ... 40
2.2.1 Performance of LG G3 using VL6180 Autofocus with TOF ... 41
2.2.1.1 Measurement Setup ... 41
2.2.1.2 Measurement Results ... 42
2.2.1.3 Diagrams ... 43
2.3 PMD CamBoard pico ... 44

2.3.1 Review on PMD CamBoard pico ... 46
2.4 Others ... 49
3 Concept Requirements ... 53
3.1 Technology Decision ... 53
4 SPAD based TOF Camera System ... 55
4.1 Block Diagram of a SPAD TOF System ... 55
4.2 Partitioning for a SPAD based system ... 55
4.2.1 Illumination System ... 56
4.2.1.1 Average and Peak Power ... 61
4.2.2 Time to Digital Converter ... 62
4.2.3 Readout ... 67
4.3 Pixel Architecture Concept ... 70
5 Electromagnetic Interference (EMI) ... 74
6 Economy ... 80
6.1 TOF Product Cost and Price ... 81
6.1.1 Fixed Costs ... 81
6.1.2 Variable Costs ... 82
6.1.3 Pricing ... 85
6.1.3.1 Price Skimming ... 85
6.1.3.2 Price Penetration ... 86
6.1.3.3 Gross Profit Margin Target ... 86
7 Conclusion ... 88
8 Prospect ... 89
9 Appendix ... 90
10 Bibliography ... 92

List of Figures

Figure 1: Product-requirement matrix 2
Figure 2: Typical TOF fields of application (right side) apply to three basic functions of TOF (left side) 3
Figure 3: Basic TOF system 5
Figure 4: Classification of system on chip (SoC) TOF image sensors [2], modified 6
Figure 5: Light source pulsed modulated 7
Figure 6: Light source sinusoidal modulated 7
Figure 7: Direct TOF pulsed [3] 8
Figure 8: Direct TOF modulated [3] 8
Figure 9: Indirect 4TG TOF pulsed [3] 9
Figure 10: Indirect 4TG TOF modulated [3] 9
Figure 11: Steady-state characteristics of APDs and SPAD with Geiger mode [3] 11
Figure 12: Passive quenched SPAD circuit [3], modified 11
Figure 13: I-V characteristics of SPAD with Geiger mode 12
Figure 14: Active quenching circuit with circuit oscillation prevention (dotted box) [4] 13
Figure 15: CMOS SPAD design 13
Figure 16: SPAD PDP performance comparison [9] 14
Figure 17: Instrument response function of a SPAD at 670 nm [12] 15
Figure 18: Ideal model of a demodulation pixel [3] 17
Figure 19: Correlation function with four sampled values [3] 18
Figure 20: Four-time gated operation principle [3], modified 18
Figure 21: Cross section and potential profile of a basic two-tap CCD element [16], modified 20
Figure 22: Simplified 2-gate surface channel PMD structure [19], modified 21
Figure 23: PMD modulation process [20] 21
Figure 24: Cross section of a basic CAPD demodulator [21] 22
Figure 25: Cross section of a pinned photodiode detector [29], modified 24
Figure 26: Pinned photodiode with a four-transistor (APS) configuration [29] 24
Figure 27: Spectral responsivity of a pinned photodiode [30] 25
Figure 28: Chip architecture with parallel read-out mechanism [34] 27
Figure 29: Cross section of a macro pixel [35] 27
Figure 30: Chip die with system blocks [36] 28
Figure 31: Depth map and profile (in millimeters) of a human face [13] 29
Figure 32: Imager architecture of a 128x128-pixel SPAD based sensor [38] 29
Figure 33: Photomicrograph of the device die, showing 32x32-pixel SPAD array and parallel histogram conversion [9] 30
Figure 34: TOF depth map and original picture of two scenes 32
Figure 35: Microphotograph of the 1.55Mpixel sensor with approx. 70mm² total die size [42] 33
Figure 36: Colored distance representation of the scene, obtained with Z-pixels (480×360). Because of 20MHz modulation frequency, the distance and hence the color range repeats every 7.5m [42] 33
Figure 37: Depth map of a scene using 16 fps with external ADC [45] 34

Figure 38: Colored 3D depth map obtained by a 32x32-pixel CAPD TOF 3D-imager [55] 38
Figure 39 Cross section of the ST VL-6180 sensor 40
Figure 40: Estimated time over distance curves with and without TOF assistance 41
Figure 41: Schematic illustration of the measurement setup including their components 42
Figure 42: Non-laboratory testing environment 42
Figure 43: Measured timings for the LG G3 as a function of the distance 43
Figure 44: Probability of capturing focused pictures as a function of the distance 43
Figure 45: PMD CamBoard pico [62] 44
Figure 46: Block diagram of the PMD Cam board pico device [62], modified 45
Figure 47: Imaging capability of the PMD device 46
Figure 48: Picture quality with no software improvements using 100µs integration time 47
Figure 49: Improved picture quality with 1ms integration time 47
Figure 50: Reflected signal captured from a black target (black wall) 47
Figure 51: Captured image under high ambient light >1klux, 1ms integration time, at a modulation frequency of 30MHz and distance to the scene of 30cm 48
Figure 52: Test behind window glass, distance to the object 40cm 49
Figure 53: Teardown pictures of the Creative Senz 3D camera 50
Figure 54: Illumination source of the Senz 3D consists of an edge-emitting LED 50
Figure 55: Maximum distance sensing a grey card 50
Figure 56: Using a Macbeth Color Checker for evaluation at 40cm 51
Figure 57: Wrong gesture detection using Creative Senz 3D 51
Figure 58: SPAD based TOF sensor 55
Figure 59: Partitioning of the TOF system showing detection, readout and processing blocks 56
Figure 60: VCSEL based illumination system 56
Figure 61: Common-cathode VCSEL driver in 65nm CMOS [68] 57
Figure 62: Structure of the laser diode driver [69] 58
Figure 63: Common anode VCSEL driver [70] 58
Figure 64: Schematic of the VCSEL driver stage [71] 59
Figure 65: Spectral width of a VCSEL compared to a LED, showing the temperature variation [74] 60
Figure 66: Basic Vernier delay line [77] 62
Figure 67: Coarse-fine TDC block diagram 63
Figure 68: external clock TDC with coarse-fine converters [81] 63
Figure 69: coarse-fine principle with reverse start-stop configuration [81] 64
Figure 70: Power consumption as a function of the enabled pixel [81] 64
Figure 71: Block diagram of the proposed ring oscillator TDC [82] 65
Figure 72: Operation principle in TCSPC mode [82] 65
Figure 73: Power consumption of the 32x32-pixel TDC array as a function of the active pixels [82] 66
Figure 74: Block diagram of the 11-bit ring oscillator based TDC [84] 66
Figure 75: Fully parallel readout structure [86] 67
Figure 76: Schematic of an event-driven readout [87] 68

Figure 77: Pixel based random access readout [78] ... 68
Figure 78: Block diagram of a column based rolling shutter system readout [78] ... 69
Figure 79: Readout schemes for SPAD based TOF sensors, whereby (ED) means event-driven and (RS) stands for rolling shutter mechanism [85] ... 69
Figure 80: Concept for a macro pixel array with four SPADs using one TDC ... 70
Figure 81: Fully parallel single-pixel concept ... 71
Figure 82: Structure of a 2x2-macro pixel array ... 72
Figure 83: Structure of a 3x3-single pixel concept ... 73
Figure 84: Comparison table of the pixel concepts to another approach assuming a detector array of 1024 SPADs ... 73
Figure 85: Ideal square waved pulses compared to real pulse shape of a VCSEL (dotted lines) ... 74
Figure 86: Characteristics of trapezoidal-shaped pulses for approximation ... 74
Figure 87 Bode plot of the trapezoidal digital pulse [90] ... 75
Figure 88: Magnitude spectra of trapezoidal waveforms with different rise times, the fundamental frequencies are in both cases 100 MHz and the duty cycle is 50% ... 75
Figure 89: Comparison of the harmonic spectrum of two trapezoidal signals with different frequencies, the amplitude is 3V, the duty cycle is changed to 10% and the rise time is 100ps. ... 76
Figure 90: Impact of the duty cycle for a trapezoidal wave with constant Amplitude: 3V, rise time: 100ps, frequency: 100MHz and two different duty cycles 10% and 50%. ... 76
Figure 91: Overlap of the harmonics caused by a trapezoidal pulse (duty cycle: 10%, rise time: 100ps, Amplitude: 3V, frequency: 100MHz) and the frequency bands used in mobile phones ... 78
Figure 92: Value based perception [92], modified ... 80
Figure 93: Cost based perception [92], modified ... 80
Figure 94: From cost to value, a win-win situation ... 80
Figure 95: Fixed costs (NRE) calculation schema ... 81
Figure 96: Estimated die size of the ST VL-6180 with suppositious figures ... 82
Figure 97: Wafer pricing report [93] ... 82
Figure 98: Silicon EDGE dies per wafer estimator [95] ... 83
Figure 99: Increase on wafer diameters over the years [98] ... 85
Figure 100: TOF benchmarking parameters ... 89

List of Tables

Table 1: Trade-off in SPAD operation and design [5], edited ... 16
Table 2: Comparison of different CCD-pixel architectures [17] ... 20
Table 3: SPAD based sensor solutions ... 31
Table 4: Pinned-Photodiode based sensor solutions (1) ... 36
Table 5 Pinned-Photodiode based sensor solutions (2) ... 37
Table 6: CAPD and CCD based sensor solutions ... 39
Table 7: Specifications of ST-VL6180 device [58] ... 40
Table 8: Specifications CamBoard pico [61] ... 44
Table 9: Maximum range achieved by the PMD CamBoard pico, integration time was 1ms and the modulation frequency 30MHz ... 48
Table 10: Performance comparison table for commercial available TOF cameras [66], modified ... 52
Table 11: Decision profile with total ratings for SPAD and CAPD ... 54
Table 12: Performance comparison table of published VCSEL driver ... 59
Table 13: Performance comparison of VCSEL compared to LEDs and Edge-emitting laser [74] ... 60
Table 14: Overall performance parameter of the introduced TDCs ... 67
Table 15: Comparison of macro and single-pixel concept ... 71
Table 16: Trade-off in TOF using pulsed signals whereby a "-"indicates a negative and "+" a positive effect on a TOF system. ... 77
Table 17: Calculation scheme for the variable costs ... 84
Table 18: Benchmarking proposal gesture detection in mobile devices ... 89

Acknowledgments

To begin with, I would like to thank Univ.-Prof. Dipl.-Ing. Dr.techn. Bernd Deutschmann, TU Graz Institute of Electronics for his support during my thesis. Particularly with regard to his assistance in terms of electromagnetic compatibility. I am greatly indebted to Dipl.-Ing. Mario Manninger from ams AG, who raised the exciting subject of my thesis and gave me the grand opportunity to write the work in hand. Furthermore, I would like to say a big thank you to the entire TOF team primarily Dipl.-Ing Karl Ilzer and Dipl.-Ing. Dipl.-Ing(FH) Robert Kappel for their support. I gladly remember many fruitful meetings and discussions. It was always a motivational and pleasant morale in the team. Additionally, I would like to thank Dr. Kerry Glover for providing me his investigation results. Finally, I would like to express my gratitude to my beloved wife Marizela, my son Tarik, who assisted me emotionally, and not forgetting my parents who always supported me.

Acronyms

1D	One Dimensional
2D	Two Dimensional
3D	Three Dimensional
AC	Alternating Current
ALS	Ambient Light Sensor
APS	Active Pixel Sensor
CAPD	Current Assisted Photonic Demodulator
CCD	Charge-Coupled Devices
CMOS	Complementary Metal-Oxide-Semiconductor
COGS	Cost of Goods Sold
CS	Common Source
DC	Direct Current
DCR	Dark Count Rate
DL	Delay Line
DLL	Delay Locked Loop
DPW	Dies per Wafer
DSP	Digital Signal Processor
D-TOF	Direct Time-of-Flight
EMI	Electromagnetic Interferences
Fab	Wafer Factory
FLIM	Fluorescence-Lifetime Imaging Microscopy
FOM	Figure of Merit
FOV	Field of View
FRET	Förster Resonance Energy Transfer
FWHM	Full Width Half Maximum
GDW	Gross amount of Dies per Wafer
GPM	Gross Profit Margin
GPMT	Gross Profit Margin Target
IC	Integrated Circuit
ID	Identity
IEEE	Institute of Electrical and Electronics Engineers
IR	Infrared
ISP	Image Signal Processor
I-TOF	Indirect Time-of-Flight
LASER	Light Amplification by Stimulated Emission of Radiation
LED	Light Emitting Diode
MOS	Metal-Oxide-Semiconductor
NIR	Near Infrared

NMOS	N-type Metal-Oxide-Semiconductor
PCB	Printed Circuit Board
PCE	Power Conversion Efficiency
PDE	Photon Detection Efficiency
PDP	Photon Detection Probability
PDΔΣ	Phase Domain Delta Sigma
PEB	Premature Edge Breakdown
PLL	Phased Locked Loop
PMD	Photonic Mixing Devices
RADAR	Radio Detection and Ranging
RGB	Red Green Blue
ROI	Region of Interest
SF	Source Follower
SoC	System on Chip
SPAD	Singe Photon Avalanche Diode
SPSD	Single Photon Synchronous Detection
SRAM	Static Random Access Memory
SW	Storage Well
TCSPC	Time Correlated Single Photon Counting
TDC	Time-to-Digital-Converter
TG	Time Gate
TOF	Time-of-Flight
TV	Television
VCSEL	Vertical-Cavity Surface-Emitting Laser
VDL	Vernier Delay Line

1 Introduction

In the last years, a fascinating technological progress in 3D depth imaging and multi-pixel range finding sensors could be observed capturing our environment as we see them in the real world. Such systems using Time-of-Flight (TOF) or structured-light are well known in academic research over decades and are recently on the best way to revolutionize applications, such as in consumer electronics, robotics, biometrics, automotive, medical care, surveillance and many more fundamentally. In terms of performance, costs and size, 3D imaging cameras for consumer electronics are hardly realizable with standard image acquisition techniques like LIDAR, interferometry or triangulation that are based on either complex scanning systems or bulky stereo-systems. Instead a new age has begun with solid-state TOF 3D cameras leading to high-end sensor solutions with higher lateral resolutions, smaller process nodes, less power consumption and due to mass production the prices of 3D systems will be competitive to well-established 2D systems in the years to come.

1.1 Motivation

In almost every today's smart phone, tablet, laptop, netbook and TV, a 2D camera system is present. A 2D system has performance restrictions, as they cannot provide a depth map information like a 3D camera. Furthermore, human 3D vision is an ambition in several applications and can be best served by 3D TOF cameras. As the ams AG has a leading role in high end mixed signal and optical IC's since years the time has come to roll out the first IC based on TOF approach. In mobile phones and tablets, there are several fields of application attractive to be served by Time-of-Flight. First, the proximity sensing market where the ams AG has much experience and still offers a sensor based on the photodiode principle. In this connection, a benefit of TOF can be a higher range and accuracy as well as a higher immunity against ambient light. Second the camera autofocus market-segment where ST Microsystems launched their TOF chip ST-VL6180 based on SPAD technology in the LG G3 phone. Using TOF for gesture recognition is a promising choice and it leads to a completely new way of human interaction as already existing devices like PMDs CamBoard pico or the structured light approach Microsoft Kinect demonstrates. According to the high market potential of TOF solutions in consumer electronics, an advanced and competitive TOF solution for ams AG has to be found. Of course, a basic rangefinder application is a concept requirement. However, the question this thesis should give an answer on is which TOF sensor technology has the best potential in terms of low cost, low power, high performance, small form factor and scalability to serve basic 1D (range finding) as well as 2D and 3D camera applications. A surveying product-requirement matrix is given in Figure 1.

	Proximity	Camera AF	Rangefinder	3D-Camera	Other Capability
Photodiode	ams				Gesture recognition
SPAD + histogramming	ams	ams	ams	ams	Industrial, Automotive, FLIM, FRET
SPAD + Sequential Readout	ST Microsystems, Blackberry	ST Microsystems			
CAPD		License $		Softkinetic/ Intel	
PMD		License $		PMD/ Google	

Figure 1: Product-requirement matrix

Figure 1 gives an overview of targeting fields of application depending on the TOF detector principle regarding competitors and in-house development.

This thesis is organized in six main chapters. The first chapter will give an overview on fields of application for TOF image sensors, an introduction of Time-of-Flight technology including working principles of TOF cameras and a review on the main pixel photodetector principles used in TOF. The second chapter will focus on State-of-the-Art TOF image sensors. Herein based on literature research, publications on TOF image sensors will be reviewed and several comparative performance tables given. After that, practical-knowledge of two different TOF fields of application will be collected. First, the camera autofocus performance of the LG G3 phone based on TOF will be analyzed and second, a gesture recognition TOF camera PMD CamBoard pico will be tested. In the third chapter, concept requirements for an ams TOF sensor solution will be given. Leading in chapter four and five to a block diagram of a suggested TOF system and a description of the main building blocks. A focus will be put on the emitter side of the TOF system especially in context to electromagnetic interferences and the size and power consumption of the main building blocks will be estimated. Furthermore a performance estimation of the detector array will be given. In order to give a perspective on costs and price for a TOF system, chapter six is dedicated to the important economic topic. The concluding chapter seven will give some conclusions and future perspectives. An outlook on a future work is also summarized in the final chapter.

1.2 Fields of Application for Time-of-Flight Image Sensors

With the rise of mobile phones and tablets, ways of user control applications have totally changed. Have been in the past hardware buttons for each control application, are there today software controlled pixel sensitive displays so called touch screens. Withal due to interacting it is still necessary to touch the surface. This implicates many drawbacks e.g. blind spots when the user hand during interaction hides some of the information or the surface gets dirty and in further consequence not any more able to operate. The explained drawbacks can be prevented and many other advantages implemented when using TOF in a contactless gesture controlled display. Furthermore, with the increase of possible applications in mobile phones and tablets the ability to capture three-dimensional data brings incredible new opportunities in several fields of applications. Thereby the knowledge to process and display the “z” coordinate reliable is an essential aspect. Especially low cost three-dimensional Time-of-Flight solutions have a tremendous potential to open a wide field of additional applications and solutions e.g. smart TV’s, home automation, interactive digital signage, gaming, robotics and medical technologies, security, automotive and industrial.

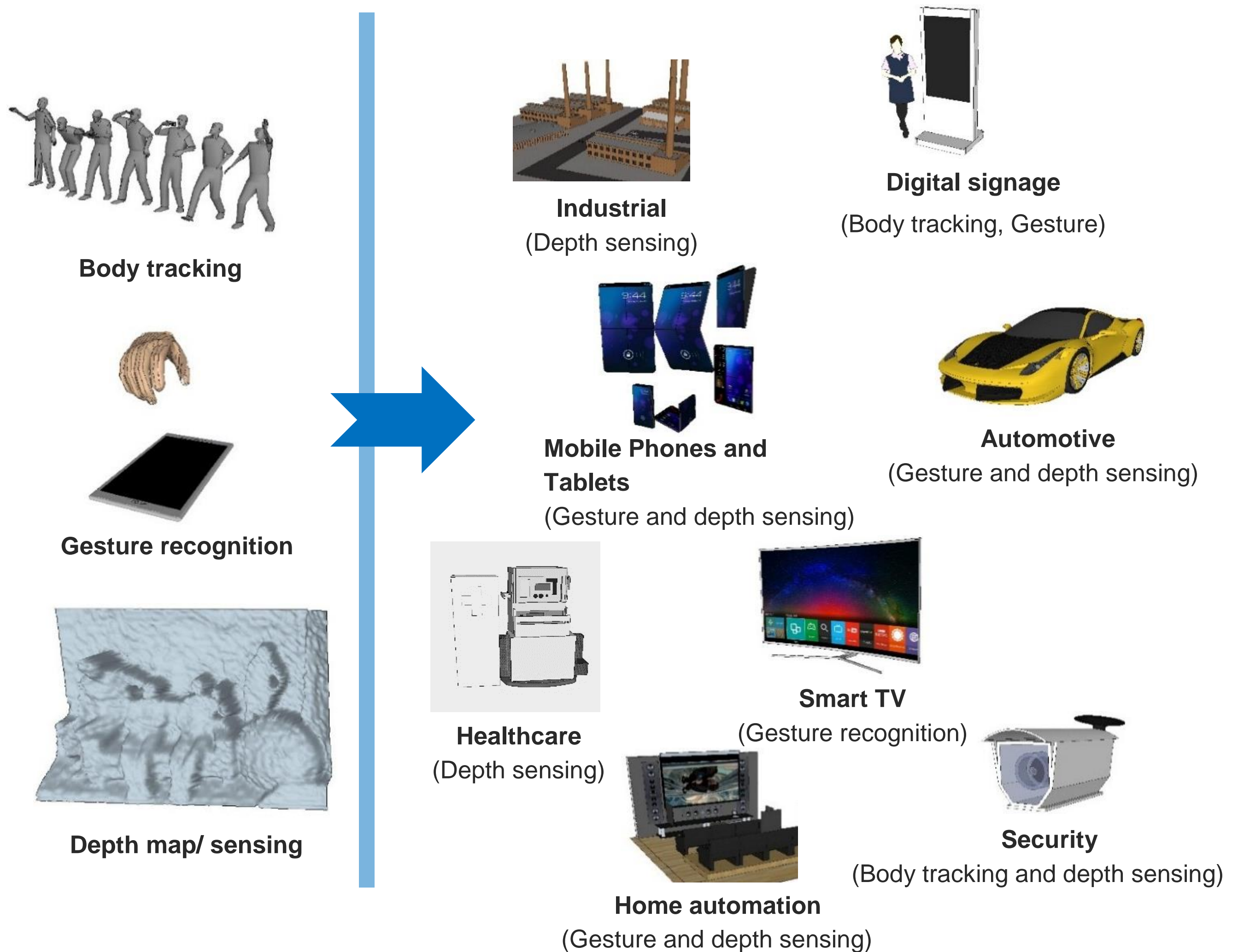

Figure 2: Typical TOF fields of application (right side) apply to three basic functions of TOF (left side)

As shown in Figure 2 all TOF fields of application e.g. mobile phones and tablets, automotive, security etc. apply at least one of the basic TOF functions body tracking, gesture recognition and depth map sensing. This means for example, body tracking is a basic application in the security sector as well as gesture recognition for user interfaces like mobile phones and tablets. In further consequence, each field of application has its specific requirements. A specification in industrial applications is a high accurate distance measurement as well as low noise and robustness. Lowest power consumption might not be a key factor in this case. A completely different guideline exist in battery-powered applications like in mobile phones and tablets. A low power consuming TOF device is a strict requirement in this particular case because the customer will not buy it when it sensibly effects the battery operation. Millimeter accuracy is for gesture recognition in user interfaces not a demand. Instead, operation under variable and high ambient light conditions. In healthcare and security a wide observation angle, expressed in "TOF language" field of view (FOV) is an important requirement. Especially, in fluorescence-life-time-imaging (FLIM), a pico-second resolution is of high significance. In Figure 2, there are only some fields of application mentioned. However, Time-of-Flight opens an incredible scope for future developments.

1.3 Time-of-Flight System

To begin with, a classification of active optical range sensor methods was proposed by Paul J. Besl in 1988. In [1], Besl distinguished six different principles namely (1) radar, (2) triangulation, (3) moiré, (4) holographic, interferometry, (5) focusing, and (6) diffraction. Beside of (1) all other imaging techniques are well described in literature and will not be touched in this thesis. First experiments with radio detection and ranging (radar) date back to Hulsmeyer in 1904, where he investigated the round trip time of radio waves reflected on ships. The fundamental equation for radar is as follows:

$$v\tau = 2d \tag{1}$$

The equation contains following parameters: "v" the velocity of the signal propagation in a specific medium, the round trip time "τ" for a signal to hit the object and return and the range named as distance "d" to the object. Assuming the signal is descended from a light source and the medium is air the commonly used synonymous to radar is Time-of-Flight (TOF).

$$z = \frac{c}{2}\ \tau_{TOF} \tag{1.1}$$

With a given speed of light (c=2.9979 x 10^8 m/s) the time (τ_{TOF}) can be measured accurately from the light source to the object and return to the photodetector. Hence, the distance z to the object can be calculated in such a classical Direct-TOF (D-TOF) measurement with the renamed radar equation (1.1). A D-TOF system requires a precise stopwatch triggered on the emitter light pulse generation and stops when the light echo is detected. Because of the timing restrictions, a D-TOF system is dedicated to SPAD-based TOF systems. An alternative TOF measurement is the Indirect TOF (I-TOF), where there is no need of a precise stopwatch but of pixels that are able to detect and demodulate a received optical signal simultaneously. Such a system is used in in-pixel photo-mixing devices. Details about measurement techniques and implementation will be described in the following chapters.

A typical solid-state TOF system (Figure 3) consists of several building blocks:

- Pulsed/modulated light source
- Optical diffusor on the emitter side
- Optical band-pass and lens on the detector side
- Photodetector, sensor (array of pixels)
- Sensor interface

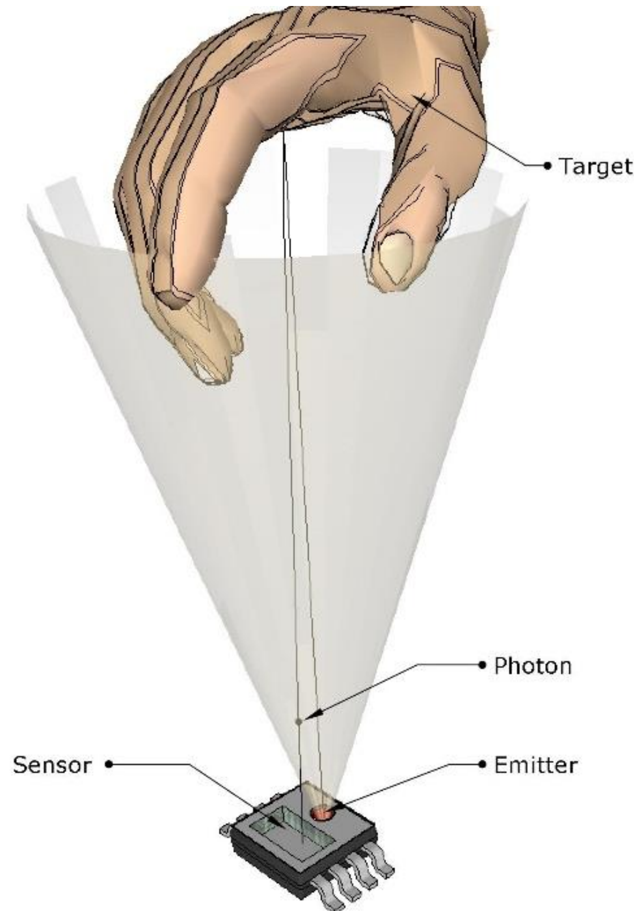

Figure 3: Basic TOF system

A light source, typically based on LASER or LED emits pulsed or modulated light mainly in the invisible infrared spectrum, an optical diffusor is used to illuminate the scene in a wide angle, an optical band-pass adapted to the wavelength ensures a high background light rejection, a photodetector sensor array (pixels) is used to measure, in a direct or indirect way, the transit time of the photons going from the emitter to the target e.g. hand and backwards and finally a capable interface provides power supply, biasing voltage, current signals and a read out bus for 3D data readout and external processing.

1.4 Classification of Solid-State TOF Image Sensors

Solid-state TOF sensors can be classified by the following attributes. The optical modulation of the emitting light source and the TOF measurement principle. The technology in which the semiconductor is built and finally the principle of the pixel photodetector. In Figure 4 an overview is given:

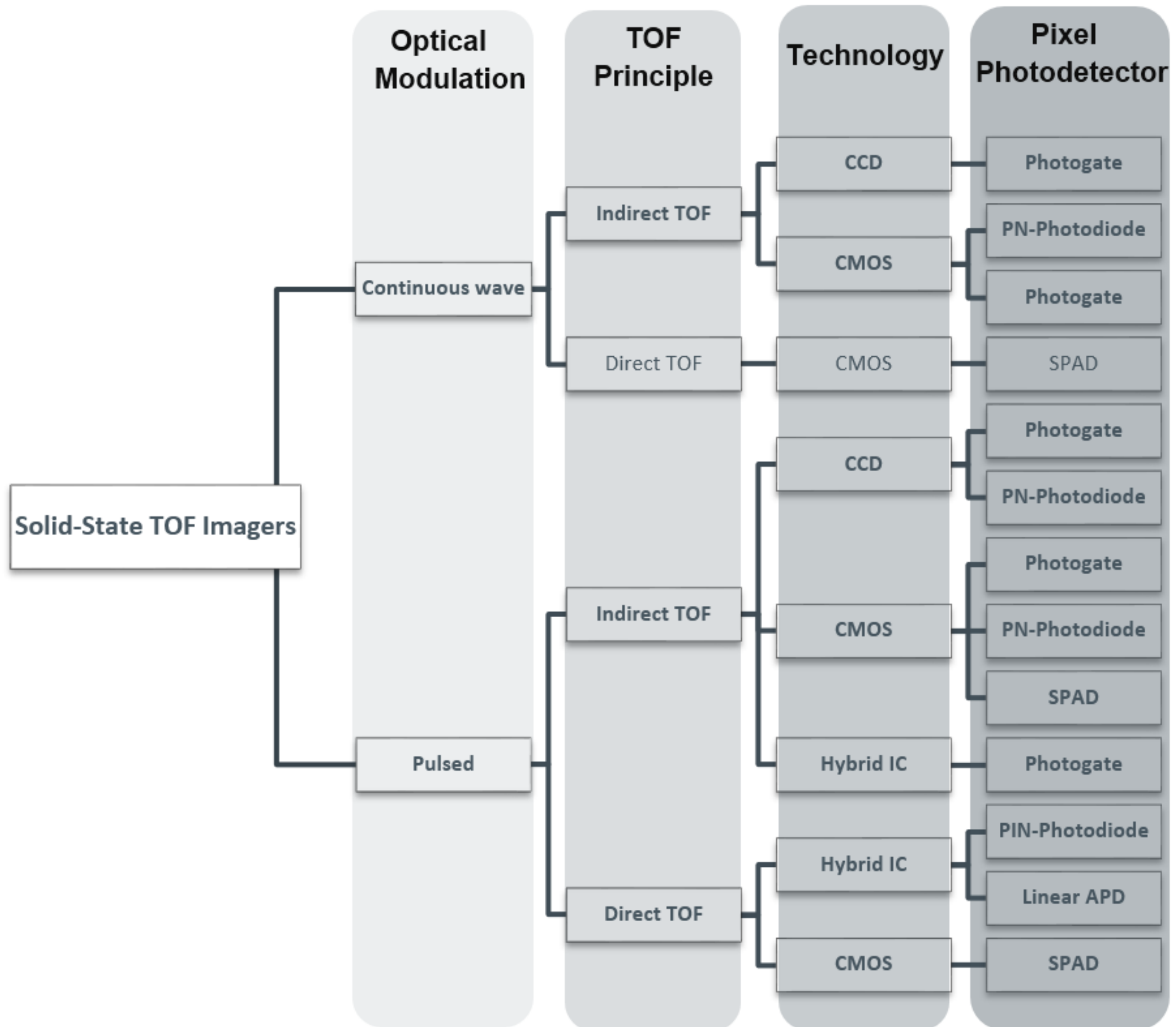

Figure 4: Classification of system on chip (SoC) TOF image sensors [2], modified

1.5 Optical Modulation Techniques

A TOF light source can be either modulated pulsed (Figure 5) like a squared wave or continuously (Figure 6) like a sine wave. Which modulation technique is deployed depends mainly on the timing constraints of the TOF system and in further consequence on the costs of the emitter unit. For a pulsed modulated light, vertical-cavity surface-emitting lasers (VCSELs) as well as edge-emitting lasers are used to generate short pulses with a pulse width in order of some tens of a picosecond to few nanoseconds. On the other hand, light-emitting diodes (LEDs) are most commonly used when the timing constraints are not that accurately. Because of their slower modulation ability, LEDs are often used with sinusoidal modulated light.

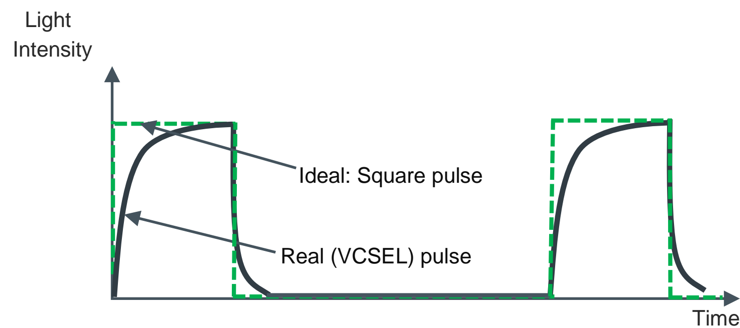

Figure 5: Light source pulsed modulated

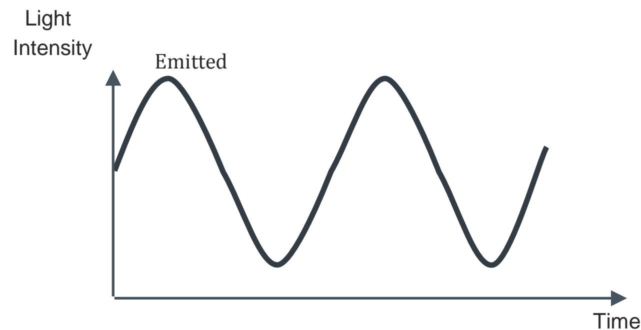

Figure 6: Light source sinusoidal modulated

1.6 TOF Measurement Techniques

1.6.1 Direct TOF (D-TOF)

In this solution, the round trip time is extrapolated directly, either out of the travel time between the transmitting and receiving photons (Figure 7), or out of the phase shift between the modulated light of the emitted and received sine wave (Figure 8).

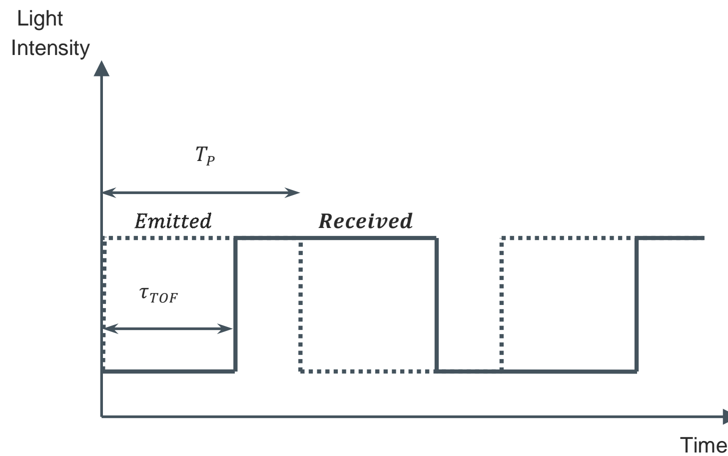

Figure 7: Direct TOF pulsed [3]

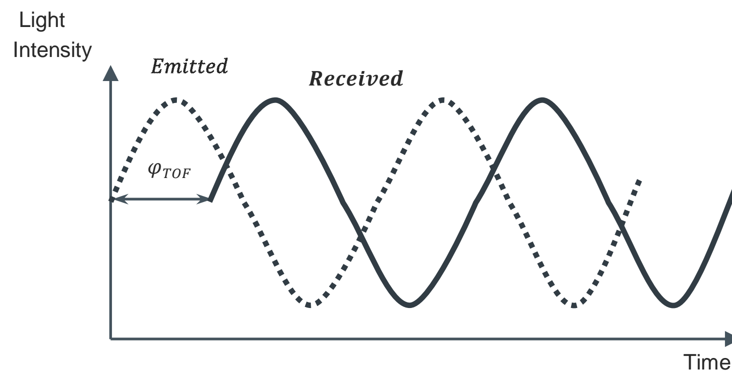

Figure 8: Direct TOF modulated [3]

If the travel time between the transmitting and receiving photons is measured (Direct TOF pulsed) and the speed of light is given as a constant with $c \cong 3 \cdot 10^8$m/s the distance to the target can be then determined by the following equation:

$$\text{Measured distance} = \frac{\text{Photon travel time}}{2} \cdot \text{Speed of Light} \tag{1.2}$$

$$z = \frac{\tau_{TOF}}{2} \cdot c \tag{1.3}$$

This shows that a measured photon travel time of 6.6ps corresponds to a distance of 1mm. Therefore, the basic challenge of every D-TOF system is obviously the realization of a high accuracy time measurement.
In “Direct TOF modulated”, the distance can be extracted by the following equation:

$$z = \frac{c}{4\pi f_m} \cdot \varphi_{TOF} \tag{1.4}$$

1.6.2 Indirect TOF (I-TOF)

The operation principle of I-TOF is to extrapolate the roundtrip time of the photons indirectly from a time-gated measurement of the light intensity using charge integrators or time-gated photon counters. In Figure 9 and Figure 10, the operation principle is given for a four-time-gated I-TOF. Each of the four time gates (TG) corresponds to a specific charge value. Both pulsed and modulated signal shapes are possible.

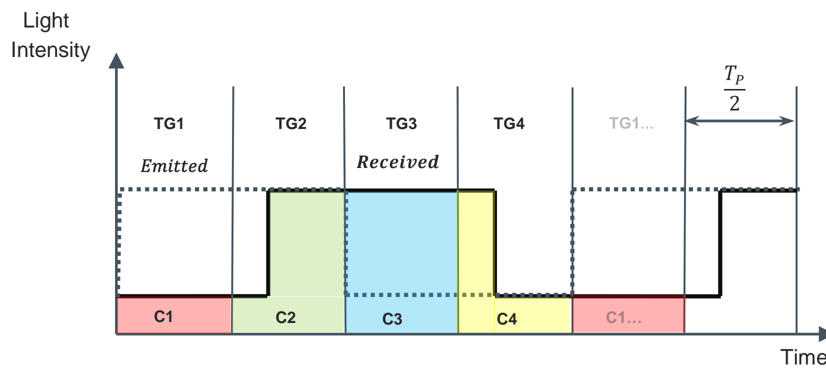

Figure 9: Indirect 4TG TOF pulsed [3]

Indirect 4TG TOF pulsed → $z=\frac{cT_p}{4}\cdot\left(1+\frac{C_3\text{-}C_1}{C_2\text{-}C_4}\right)$ (1.5)

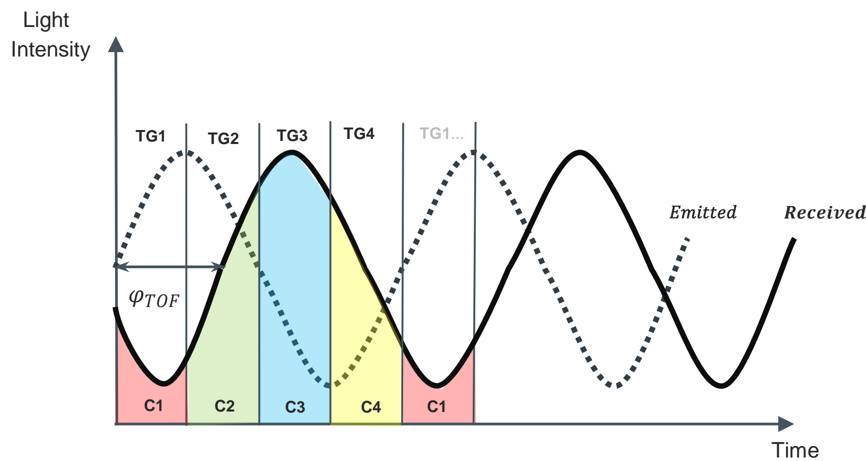

Figure 10: Indirect 4TG TOF modulated [3]

Indirect 4TG TOF modulated → $z=\frac{c}{4\pi f_m}\cdot\arctan\left(\frac{C_3\text{-}C_1}{C_4\text{-}C_2}\right)$ (1.6)

In an I-TOF, four-bucket, four-tap technique, the charge is integrated during four time intervals (TG1-TG4) of equal length within one modulation period (T). Assuming the light intensity is proportional to the intensity of the incident light, four charge packets C1-C4 are then acquired and have to be stored at four different spatial locations so called taps insight each pixel. The distance information can be extracted using either equation (1.5) for a pulsed signal or (1.6) for a sinusoidal signal. This four-bucket principle can be repeated over many periods leading to higher noise-immunity and it enables the sensor to detect low intensity signals. A further description of the four-time-gated acquisition technique will be given in chapter 1.7.2. A detailed description of the two time-gated acquisition technique is given in [3].

1.7 Pixel Photodetector Principles

The core of any scanner less solid-state TOF measuring system is represented by the photodetector or pixel array. Several photodetector principles exist and many full-custom detectors have been developed in the last decades for this class of system. Based on a proposal in [3] three groups of pixel photodetectors for 3D solid-state TOF as well as basic 1D or 2D applications can be stated:

- Single Photon Avalanche Diodes (SPAD's)
- In-pixel photo-mixing devices
- Pinned-Photodiodes

SPADs have the feature to operate in a steady-state mode with nearly infinite gain. When coupled to a proper processing circuit they are able to detect even single photons. A specific photo-mixing effect is used in in-pixel photo-mixing devices where the photo-generated charge is guided toward two or more electrodes. Pinned photodiodes coupled to processing circuitry recover the distance information from the photo-generated current by the photodiode.
In order to give an overview on TOF detector principles, this chapter will describe the main technologies used in TOF detectors today. In addition, a functional description to each technology will be given and performance parameters will be described.

1.7.1 SPAD based Detectors

Detectors based on single-photon avalanche diodes are able to capture photons with a very high time-of-arrival resolution. Timing resolutions in the order of a few tens of a picosecond are achievable [3]. In literature silicon SPADs are well developed and commercial available since years. They are used in several sciences where photon counting and time-correlated photon counting techniques are implemented. In physics, biology, chemistry or material sciences with fields of application, e.g. fluorescence-lifetime imaging microscopy (FLIM) or fluorescence-resonance energy transfer (FRET). In astronomy for laser ranging in space applications as well as in basic quantum mechanics and cryptography [4].
SPADs are used in a pseudo state mode where an excess bias voltage V_{EB} above the breakdown voltage V_{BD} is applied, as long as no carriers are present in the depletion region. Due to incoming photons, carriers are

generated and through the dependency of the electric field and material as well as ambient conditions, an avalanche occurs. If the electric field is high enough electrons and holes are causing ionization and the avalanche diode is working in Geiger mode where the optical gain is virtually infinite (see Figure 11).

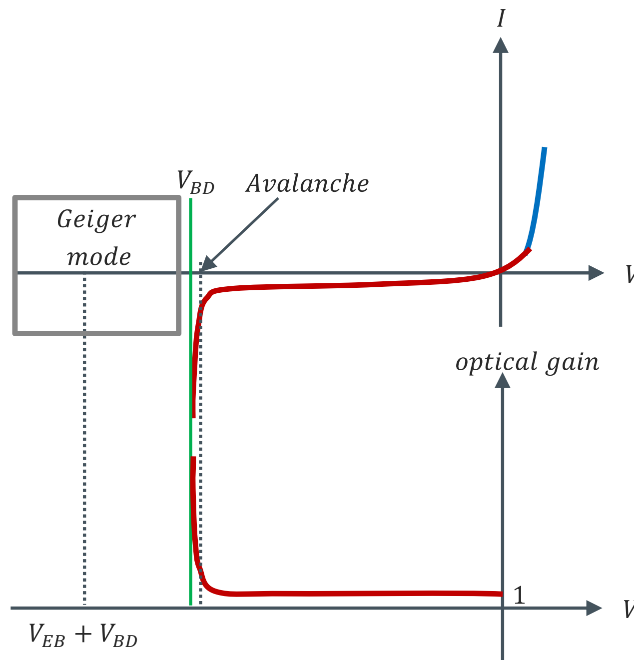

Figure 11: Steady-state characteristics of APDs and SPAD with Geiger mode [3]

In distinction of avalanche photodiodes (APDs) where a pulse of electric current is outputted synchronously to the arrival of single photons and then analyzed by an external circuit to get the time-of-arrival, SPADs are able to detect a series of photons with the inclusion of an active or passive quenching circuit [4]. A passive quenching circuit consists in the simplest way of a resistor in series to the SPAD. In Figure 12 an example of a circuit is shown where the resistor is realized by an NMOS transistor. A comparator is used to shape the incoming pulse to a square wave. To bring the SPAD into Geiger mode V_{EB} in addition to V_{BD} must be applied on the cathode side of the SPAD.

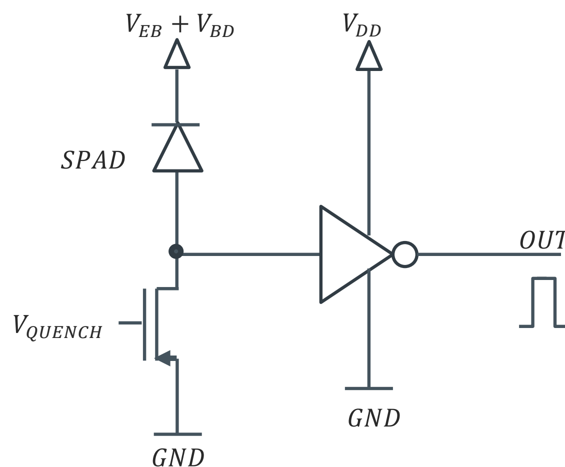

Figure 12: Passive quenched SPAD circuit [3], modified

A description of the functional behavior of the circuit is given in Figure 13.

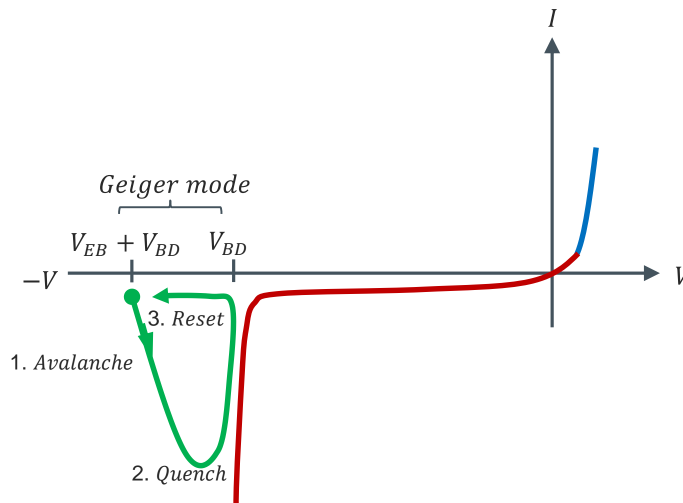

Figure 13: I-V characteristics of SPAD with Geiger mode

In the beginning when there are no free carriers in the junction, the applied voltage on the SPAD is the operation voltage $(V_{EB} + V_{BD})$. Depending on the incoming light intensity, either ionization occurs or not. If the ionization does not occur the incident photon is not detected. In the case of a significant ionization, a rapid buildup of free carriers will continue until its limited by space-charge phenomena [5]. Through a diffusion process, the avalanche will spread to other regions of the diode. The current across the SPAD increases and consequently the voltage across the diode will decreases depending on the parasitic capacitance and the quenching resistor. If the voltage across the SPAD reaches the excess bias voltage level, the SPAD is quenched. After a short period of time (dead time) where the voltage is recharged through a current flow from the quenching resistor into the parasitic capacitance of the diode, the SPAD is able to detect another carrier [3].

In an active quenching circuit (Figure 14), the SPAD voltage or current is compared with a threshold signal to identify an avalanche. After an avalanche is detected, a fast comparator whose output switches the bias voltage source to breakdown voltage (V_{BD}), thereby quenching the avalanche. After an accurately controlled hold-off time, the bias voltage is switched back to SPAD operating level. The basic advantage for an active quenching circuit is given by a fast transition from the quenched state to operating state and a short and well-defined dead time [4].

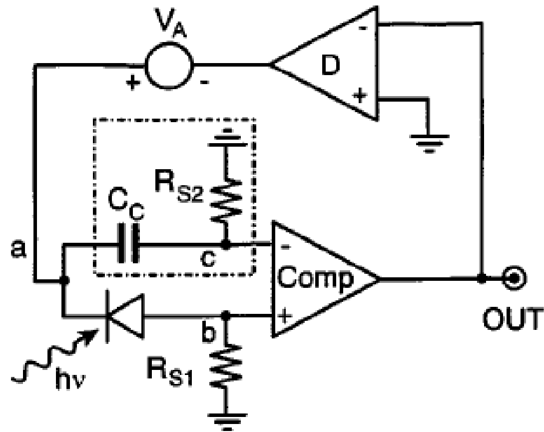

Figure 14: Active quenching circuit with circuit oscillation prevention (dotted box) [4]

For SPAD design it is essential to implement junctions that can be reversed biased at high voltages. Therefore, it is necessary to have a good knowledge of the process and layers available. In literature several CMOS SPAD designs with process nodes from 65nm [6] to 0.35µm [7] can be found. In [3] and [5] the most common structures are investigated. All of them target a reduction of the electric field or the increase of the breakdown voltage at the edges of the junction in order to prevent the premature edge breakdown (PEB). A cross section of a possible CMOS SPAD design is given in Figure 15.

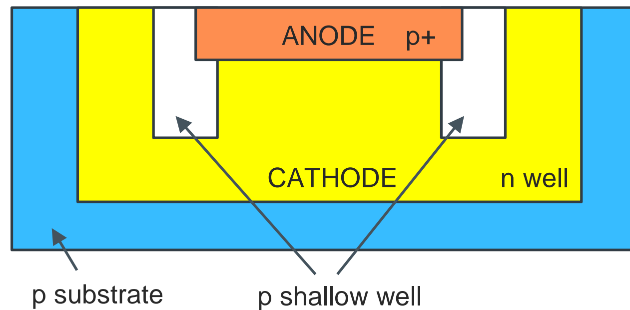

Figure 15: CMOS SPAD design

For the characterization of SPAD some performance parameters are important which will be described as follows.

1.7.1.1 Photon Detection Probability (PDP)

The sensitivity measured as Photon detection probability (PDP) or Photon detection efficiency (PDE) describes the probability of detecting a single photon hitting the SPADs surface in a given wavelength. PDP is defined in [8] with following equation:

$$\mathrm{PDP}(\lambda) = \frac{\text{Total avalanche breakdown counts} - \text{Dark count rate}}{\text{Number of impinging photons}} \tag{1.7}$$

In literature, PDE is used as SPAD sensitivity factor:

$$\mathrm{PDE} = \text{Fill Factor} \cdot \mathrm{PDP} \tag{1.8}$$

Where the Fill Factor is defined as:

$$\text{Fill Factor} = \frac{Pixel\ light\ sensitive\ area}{Total\ pixel\ area} \tag{1.9}$$

PDP/PDE is strongly dependent on the wavelength and the excess bias voltage V_{EB}. A low PDP may be a limiting constraint for some applications. As can be seen in Figure 16 the highest PDP is mostly in the visible range. In the near infrared spectrum (800nm -1000nm) PDPs are usually below 10%. A SPAD PDP performance comparison figure is given below.

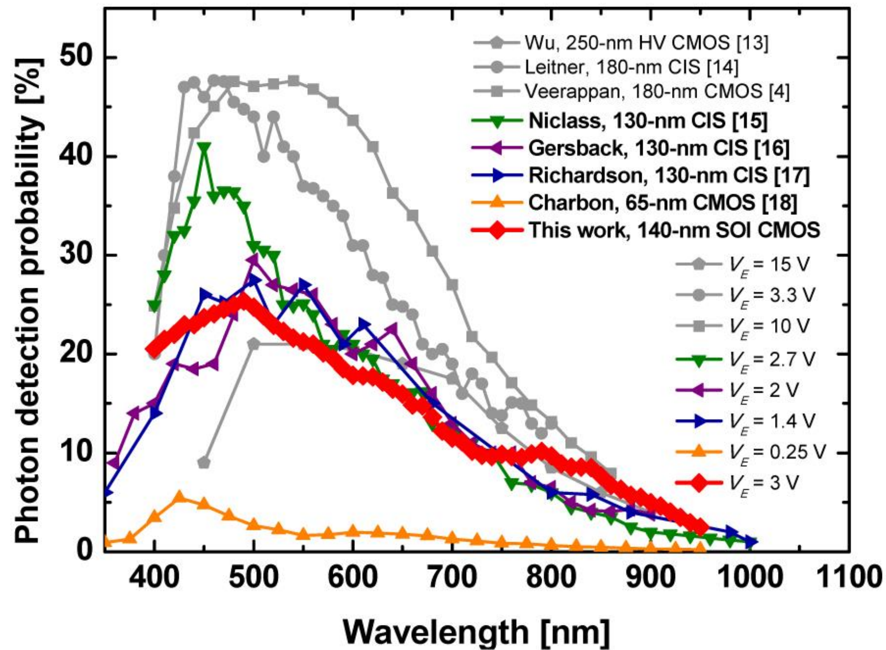

Figure 16: SPAD PDP performance comparison [9]

As stated in [8], PDP depends on the doping profile of the CMOS process. PDP improvements can be made by modifying the optical stack or applying post processing steps. A sensible SPAD in the near-infrared spectrum (NIR) and infrared spectrum (IR) spectrum can be reached when increasing the multiplication region.

1.7.1.2 Dead Time

As previously described the applied voltage to a SPAD is $V_{EB} + V_{BD}$. Due to the virtually infinite gain an avalanche immediately occurs if a photon hits the SPAD surface. A quenching circuit lowers the SPAD bias voltage to stop the avalanche followed by a recharge phase where the SPAD is returned into sensing mode. During the quenching and recharge time the SPAD is not sensitive to detect another photon. This short period of time is also called dead time. Niclass proposed a definition of dead time in [2] as the moment a photon that triggers an event is absorbed until the moment the SPAD recovers 90% of its nominal excess bias voltage (V_{EB}). A low dead time is desirable in 3D-Imaging applications because it restricts the dynamic range of the image sensor.

1.7.1.3 Noise Sources in SPAD

In terms of noise, uncorrelated noise and correlated noise sources can be distinguished. The main uncorrelated noise occurs due to ambient light and tunneling effects. The probability for tunneling effects increase with the magnitude of the electric field. The main correlated noise is afterpulsing probability. During an avalanche some carriers may be captured by trapping centers. If such a carrier is reemitted into the multiplication region the probability of an after pulse increases [10]. Such random avalanches lead to a dead time for the SPAD in the scale of some tens of nanoseconds. Afterpulsing probability is a limiting factor in terms of dead time reduction and it increases with fabrication defects. Other correlated noise sources are optical and electrical crosstalk [3]. An important noise factor in SPAD is Dark Count Rate (DCR). It counts both to uncorrelated and correlated noise. Uncorrelated DCR emerges because of thermal carrier generation effects are Poisson-distributed and increase with temperature. It is also depended on V_{EB} . On the other hand, correlated DCR occurs when carriers which are captured during an avalanche in deep energy levels of the junction depletion layer retrigger an avalanche and generate afterpulsing [4].

1.7.1.4 Timing Jitter

The SPAD timing jitter or timing resolution is defined between the true arrival time of the photons on the SPAD surface and the actual detection time from the detectors electrical output pulse. It is usually reported as the full width at half maximum (FWHM) value of the instrumental response [11]. A typically timing jitter histogram is shown in Figure 17.

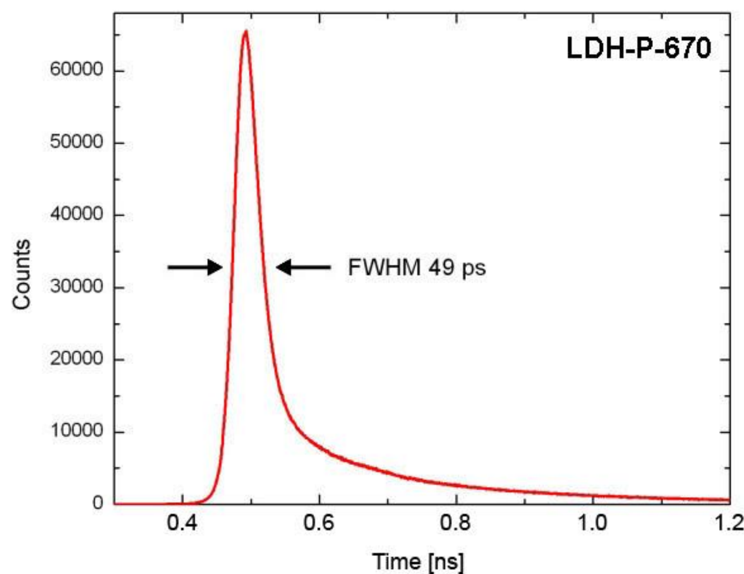

Figure 17: Instrument response function of a SPAD at 670 nm [12]

Though timing jitter is of great importance for TOF-based 3D vision [13], improvements are possible by increasing the excess bias voltage. In case of a higher V_{EB} the depletion width increases. Therefore, only photons of longer wavelengths can be absorbed, giving a sharper pulse shape and a lower FWHM. On the other hand with smaller V_{EB}, saturation occurs, giving a lager pulse shape and higher timing jitter.

1.7.1.5 Trade-off in SPAD Operation and Design

As it was shown in the previous section there is a complex trade-offs between SPAD operation performance and SPAD design. The correlation between several factors in a p+ -n SPAD surrounded by a p-doped guard ring in an n-well substrate can be seen below:

		SPAD Performance Parameter									
		PDP (red)	Timing jitter (red)	PDP (blue)	Timing jitter (blue)	Low costs	V_{bd}	DCR (corr.)	DCR (uncorr.)	Dyn.Rng.	Fill factor
Process/Design Parameter	Increase Junction depth	+	+	−	−						
	Increase Deep well depth	+	+			−					
	Increase Deep well doping	−	−				+	−	−		
	Increase V_{eb}	+	+	+	+			−	−	−	
	Increase Diode area		−		−	−		−	−		+
	Active Quench								+		−
	Increase dead time								+	−	

Table 1: Trade-off in SPAD operation and design [5], edited

As can be seen in Table 1 many tradeoffs exist in SPAD design. For example signifies an active quenching circuit a desired decrease in DCR with the drawback of a reduced fill factor. On the other hand, a higher fill factor is only achievable due to increasing diode area, leading to undesired higher timing jitter and DCR. An increase on junction depth has a positive effect on the PDP and the timing jitter in the red spectral range but a negative effect on the PDP and the timing jitter in the blue spectral range. The table can be also considered in an opposite way e.g. a low cost SPAD can be implemented when a design is chosen with less deep well depth and small diode area respectively die wastage.

1.7.2 In-Pixel Photo-Mixing Devices

In the early 90s, a breakthrough in 3D imaging systems was observed with pixels that are able to detect and demodulate a received optical signal simultaneously. Thereby each pixel performs demodulation of the incoming light wave including the functions:

- Light detection
- Fast shutter or correlation
- Charge storage for multiple accumulations

In literature, they are known as lock-in pixels, correlation pixels or demodulation pixels [3]. An ideal demodulation pixel can be modeled as shown in Figure 18.

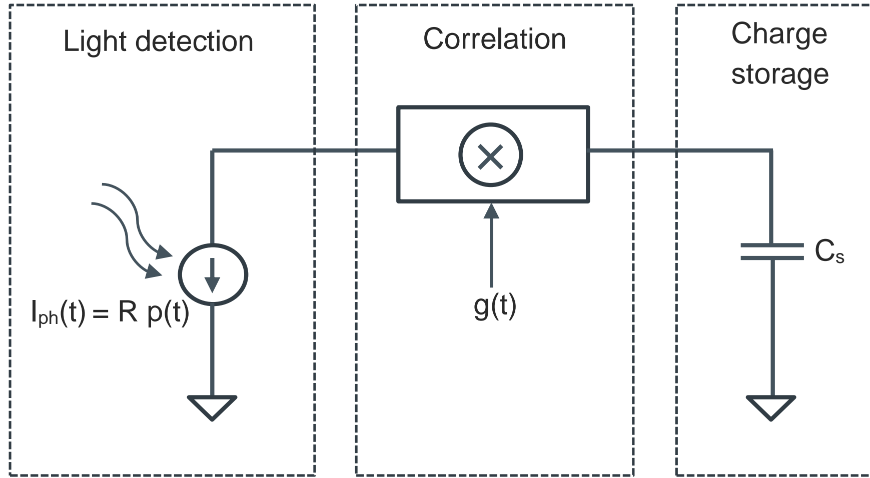

Figure 18: Ideal model of a demodulation pixel [3]

The light detection is described with a photo-current generator whereby the photocurrent ($I_{ph}(t)$) is a function of the optical power incident on the pixel p(t) and the detector responsivity (R). Next, the correlation or charge-flux control gate is dependent on the sampling function g(t) which can be a complex non-linear function of time but usually it has a square waved shape. Finally, the charge storage is performed by the storage capacitor (C_s) [3]. The mathematical description of the correlation function $c(\tau)$ between p(t) and g(t) is given by:

$$c(\tau) = lim_{T\to\infty} \frac{1}{T} \int_0^T p(t) \cdot g(t+\tau) dt \tag{2}$$

Where τ is defined by the delay between p(t) and g(t).

The output voltage on C_s, after an integration time of T_{int} is proportional to the previously defined correlation function and can be expressed as:

$$V(\tau) = \frac{R}{C_s} \int_0^{T_{int}} p(t) \cdot g(t+\tau) dt = \frac{R \cdot T_{int}}{C_s} \cdot c(\tau) \tag{2.1}$$

Assuming a square waved sampling function g(t) and a sinusoidal optical signal p(t), the correlation function $c(\tau)$ will be a sinus wave function as given below:

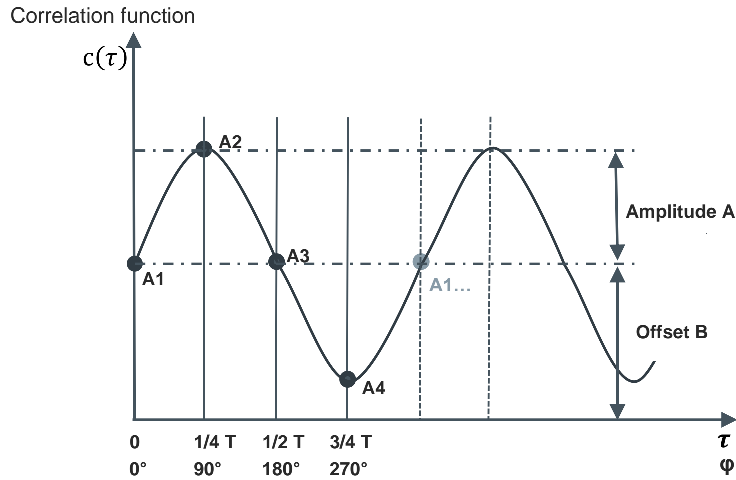

Figure 19: Correlation function with four sampled values [3]

This approach is used to calculate the phase delay (φ) the amplitude (A) and the offset (B), out of the four sampled values (A_1-A_4) of the correlation function (Figure 19), using following equations:

$$\varphi=\arctan\left(\frac{A_1\text{-}A_3}{A_2\text{-}A_4}\right) \tag{2.2}$$

$$A=\frac{\sqrt{(A_1-A_3)^2+(A_2-A_4)^2}}{2} \tag{2.3}$$

$$B=\frac{A_1+A_2+A_3+A_4}{4} \tag{2.4}$$

With the calculated phase delay, the distance can be extracted using equation 1.4 in chapter 1.6.1.

Practically, a simultaneous acquisition is done using four-time-gated shutters. Therefore, one by one is activated for a time period equal T/4. During this time slot all photo-charges are transferred to the respective charge storage [3]. Such an operation principle is shown in Figure 20 and it is commonly used in I-TOF (c.f. chapter 1.6.2).

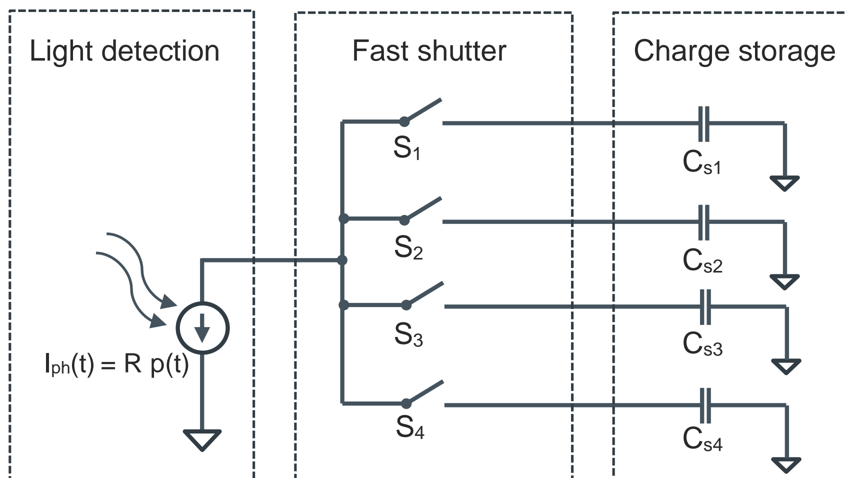

Figure 20: Four-time gated operation principle [3], modified

For the characterization of in-pixel photo mixing devices, some performance parameters are important which will be described as follows.

1.7.2.1 Demodulation Contrast

The demodulation contrast (C_d) describes the non-ideality of the shutter operation in a real device. Due to the influence of wavelength, frequency and angle of the incident light, carriers do not reach 100% the proper collection node within the integration time. This attribute can be described using following equation:

$$C_d = \frac{g_{max} - g_{min}}{g_{max} + g_{min}} \tag{2.5}$$

It must be distinguished from the overall demodulation contrast of an I-TOF system, defined as the ratio between amplitude A and offset B [3].

1.7.2.2 Fill Factor

A more generally used parameter for I-TOF as well as D-TOF sensors is called fill factor. It is defined as the ratio between the active area and the pixel area. Whereby the active area is understood as the light sensitive area and the pixel area that includes the light sensitive area as well as the demodulation, reset and readout unit [14].

1.7.2.3 Quantum Efficiency

In a TOF system, not all incident light hitting the pixel surface generates electrons. This process is mainly governed by probability. An expression describing the non-ideality of the conversion is called quantum efficiency and it is a function of wavelength. For a particular wavelength (λ), quantum efficiency is defined as the ratio between the number of electrons generated (n_e) and the number of photons hitting the active pixel area (n_p). Whereby n_e consists of the electrons generated by the modulated light from the emitter plus the ambient light [14]. Quantum efficiency is mathematically described by:

$$\eta(\lambda) = \frac{n_e}{n_p} \tag{2.6}$$

1.7.2.4 Responsivity

Another factor describing the efficiency of the photo-charge generation is called responsivity and it is defined as the ratio between the photo-current generated and the power incident on the active pixel area. Responsivity is given by the following equation:

$$R = \frac{\lambda \cdot q_e}{h \cdot c} \cdot \eta(\lambda) \tag{2.7}$$

Where the factors are the wavelength (λ), charge of a single electron (q_e), plank's constant (h), speed of light (c) and the quantum efficiency (η) [14].

1.7.2.5 Charge-Coupled Device (CCD)

One of the first publications of a sensor for 3D applications using CCD principle was a “lock-in” image sensor presented in [15]. Based on the I-TOF principle described in chapter 1.6.2, each pixel measures the mean brightness level (offset), phase φ and amplitude. Based on [3], CCD devices can be determined as central-gate demodulators. Such a CCD pixel is built up symmetrically with a photo-sensitive gate in the middle and two or more lateral transfer gates (Figure 21). A typical operation principle of a CCD pixel consists of two successive modes. In an integration phase, the generated electrons are accumulated in the pixel capacitances. Depending on the potential energy gradient that can be adjusted when applying a voltage on the left photo gate (pgl) or right photogate (pgr) the charges flow either to integration gate left (intgl) or to integration gate right (intgr). In a second phase or shift phase, the photo charges are transferred to the read out node, by lowering the potential barrier of the integration gates.

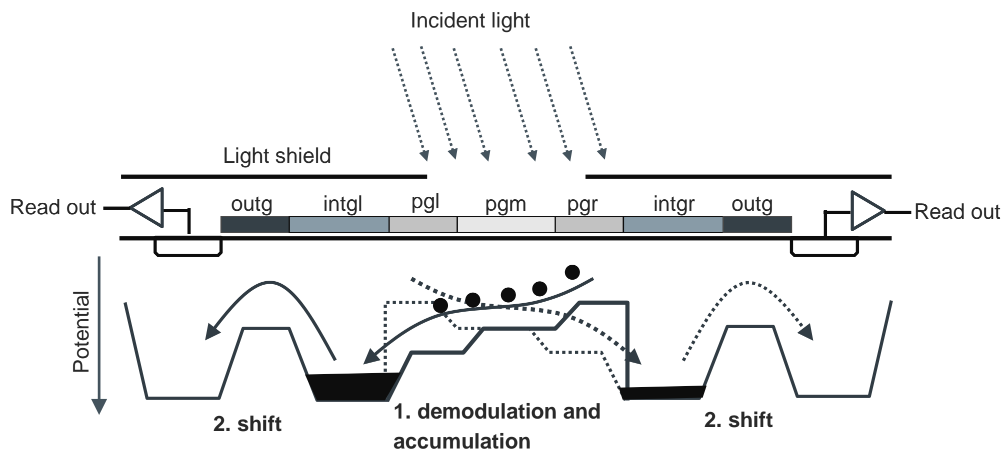

Figure 21: Cross section and potential profile of a basic two-tap CCD element [16], modified

In literature, several CCD pixel architectures are described. The most common structures are multi-tap, 4-tap or more accurately a double 2-tap, 2-tap and 1-tap CCD element. Assuming a double 2-tap structure is used providing four charge values (C1-C4) the distance information can be obtained using previous described I-TOF equations.

All these CCD demodulation pixels have their advantage and disadvantage as can be seen in Table 2 below.

Pixel structure	Storage sites	Photo sensitive area	Fill factor	Maximum demodulation frequency
Multitap-CCD	4 or more	45x15µm²	5.6%	500kHz
4-tap CCD	4	15x15µm²	6.6%	10-20MHz
1-tap CCD	1	21x13µm²	22.3%	>20MHz

Table 2: Comparison of different CCD-pixel architectures [17]

In terms of performance, a tradeoff between sensitivity and bandwidth is stated for CCD pixels. A smaller central gate leads to a lower pixel fill factor decreasing the sensitivity. On the other hand, a small central gate is needed to obtain a large demodulation bandwidth [17].

1.7.2.6 Photonic Mixer Devices (PMD)

A first PMD demodulation pixel structure was introduced by R. Schwarte et.al. in the 90s at University of Siegen, Germany where the pixel is implemented in dedicated CMOS/CCD technology [18]. In Figure 22, a typical PMD two-gate demodulation pixel is shown. Each pixel consists of two conductive and transparent MOS photogates. Both are equally illuminated by the incoming modulated optical signal (e.g. sinusoidal or square wave shaped). Next to them, there are two reversed biased diodes for photo-generated charge sensing respectively readout [19]. Its modulation process can be easily described using Figure 23.

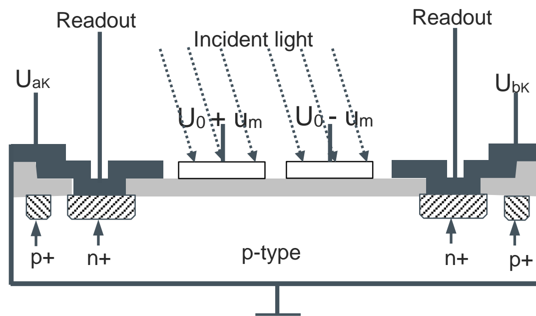

Figure 22: Simplified 2-gate surface channel PMD structure [19], modified

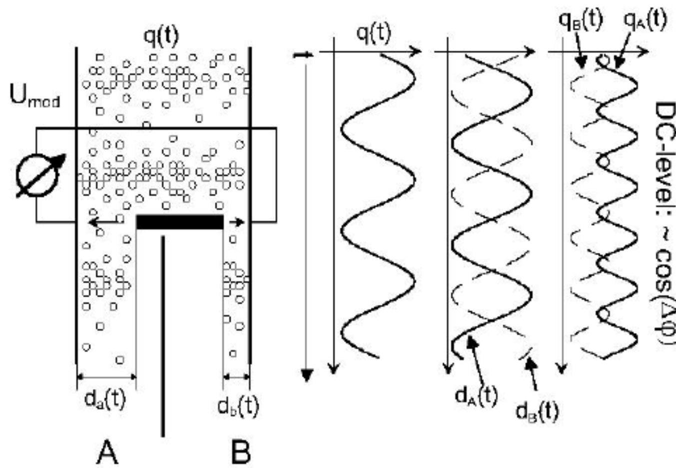

Figure 23: PMD modulation process [20]

The readout gates of the PMD are two equally sized bins A and B containing the photo-generated electrons. Equivalent to the induced electric field by the surface gates, a slider in scale of a bin is positioned above the bin apertures. Let us assume the slider covers bin A. In this particular case all charges flow into bin B and conversely. Hence, a maximum demodulation contrast of 50% is achievable. Typically the slider is modulated following an e.g. cosines signal. Then the count of electrons flowing into bin A is proportional to the modulation

signal of the slider multiplied with the charge intensity. Equally, the charges in bin B are proportional to the product of the charge intensity and the inverse modulation function. The generated photo-current of the PMD assuming a sinusoidal illumination can be described using following equation:

$$i_p(t) = S \cdot P_H + 0.5 \cdot S \cdot r \cdot P_{mod} \cdot (1 + cos(2\pi \cdot f_{mod} \cdot (t - \tau_{TOF}))) \quad (2.8)$$

Where S is the sensitivity, P_H is the background illumination, r is a reflection and damping factor, P_{mod} is the modulated light, f_{mod} is the modulation frequency and τ_{TOF} denotes the time of flight. The differential voltage between the readout gates A and B becomes:

$$U_{AB}(t) = K \cdot r \cdot P_{mod} \cdot t_{int} \cdot cos(\Delta\varphi_{TOF}) \quad (2.9)$$

With K as constant factor, t_{int} the integration time period, $\Delta\varphi_{TOF}$ the phase difference between emitted and received light. With a known phase delay $\Delta\varphi_{TOF}$ the distance information can be computed in a PMD device using equation (1.3) [20].

1.7.2.7 Current Assisted Photonic Demodulators (CAPD)

An alternative CMOS photo-detector structure with potential to increase both sensitivity and speed was first introduced in [21]. Compared to the previous photo detectors with drift zones and diffusion zones in CAPD a moderate drift field can be implemented by modulating the voltage applied to two p+ substrate contacts. This induces a majority current in the substrate, guiding the photo-generated electrons towards one of the two detection electrodes. Several different CAPD photo-detector structures can be found in [22]. A basic CAPD cross section is shown in Figure 24, having two modulation electrodes (V_{g1} and V_{g2}) and two detection electrodes (V_{d1} and V_{d2}).

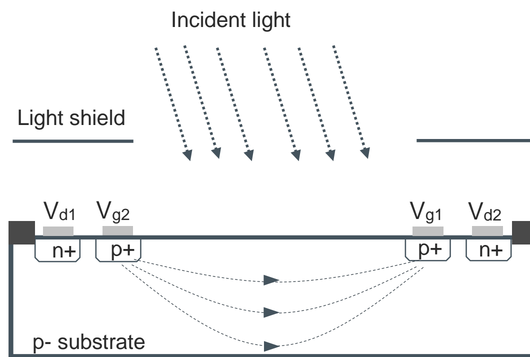

Figure 24: Cross section of a basic CAPD demodulator [21]

When light hits the photosensitive zone of the pixel and no voltage is applied between V_{g1} and V_{g2}, equal amounts of photo generated electrons are collected by V_{d1} and V_{d2}. If a sine-wave voltage is applied between V_{g1} and V_{g2} at the same frequency and in phase with the modulated light used to illuminate the scene, correlated amounts of the carriers generated by the incident light can be driven to the two different detecting electrodes, and the distance information can be extracted from the phase delay. Assuming that no photocurrent is leaking to adjacent pixels the current at the detection electrodes V_{d1} and V_{d2} can be written as:

$$I_{Vd1} = p_{Vd1} \cdot I_{total} \quad (3)$$

$$I_{Vd2} = (1 - p_{Vd1}) \cdot I_{total} \quad (3.1)$$

With $I_{total} = I_{Vd1} + I_{Vd2}$, the total photocurrent and p_{Vd1} is the part of I_{total} collected by V_{d1}. If the emitted light is sine wave modulated and the modulation voltage between V_{g1} and V_{g2} is sinusoidal with equal frequency and in phase with the emitted light, the collected currents can be rewritten as:

$$I_{Vd1} = \left[\frac{1}{2} + A_{Vd1}^{AC} \cdot \sin(2\pi f t)\right] \cdot [I_{total}^{DC} + I_{total}^{AC} \cdot \sin(2\pi f t - \varphi)] \quad (3.2)$$

$$I_{Vd2} = \left[\frac{1}{2} - A_{Vd1}^{AC} \cdot \sin(2\pi f t)\right] \cdot [I_{total}^{DC} + I_{total}^{AC} \cdot \sin(2\pi f t - \varphi)] \quad (3.3)$$

With A_{Vd1}^{AC} is the amplitude of the AC component of $p_{Vd1}$and I_{total}^{DC}, I_{total}^{AC} is the DC, AC component of I_{total}. Further f is the modulation frequency and φ the phase difference between the emitted and detected light.
The distance information can be achieved from I_{Vd1} and I_{Vd2} by low-pass filtering their AC components. This is done by integrating the obtained photocurrents. Two read-out schemes are possible either single ended or a differentially. With a given φ the distance to the target can be measured using equation (1.4).
An important performance parameter in TOF pixels is the previous described demodulation contrast. For a CAPD pixel the demodulation contrast can be expressed by the following equation:

$$C_D = A_{Vd1}^{AC} \cdot \frac{I_{total}^{AC}}{I_{total}^{DC}} \quad (3.4)$$

A more detailed description on CAPD can be found in [14], [23].

1.7.2.8 Pinned-Photodiode Demodulators

In TOF, sensors for measuring the distance to objects in a scene are also used pinned photodiodes. They have been developed in the 1980s within charge-coupled devices and have shown benefits in the area of color response and charge capacity [24]. A breakthrough for pinned photodiodes in solid-state image sensors was the integration into the image sensing element of an active pixel sensor (APS) in CMOS/CCD technology [25], achieving imaging performance exceeding CCDs. In [26] a review of the pinned photodiode development for CCD and CMOS image sensors is given, showing that several advancement have been done in the last decade. One of the most demanding tasks in their optimization is the design of the transfer gates to increase the charge transfer speed. The fastest transfer speed is obtained with a U-shaped transfer gate reaching a total charge transfer time less than 80ns [3]. In terms of noise and crosstalk, improvements have been made by implementing epitaxial technology. By using 3-7 microns of p-epitaxial layer on p+ substrate, diffusion of unwanted charges generated deep into the substrate can be prevented [26]. An important advantage of pinned photodiode is their low dark current. Thanks to a surface shielding p+ layer dark current as low as 50pA/cm² at

60°C can be achieved [27]. In a comparison of two pinned photodiode structures in standard 0.18 CMOS process presented in [28] is shown that even lower dark current in femto Ampere range is achievable.
The structure of a modern pinned photodiode used in TOF sensors is shown in Figure 25. The main elements are an n-type buried signal charge storage well (SW) region between a lower p-type layer and a p+ pinning layer at the top surface, two polysilicon transfer gates (G1 and G2) are extended to the central region of the device, so that a voltage difference applied at the gates creates a lateral electric field, and two n+ output floating diffusions (D1 and D2). Such a lateral electric field is beneficial to the device because it increases the charge transfer through the gates leading to a higher modulation frequency needed in TOF applications [29].

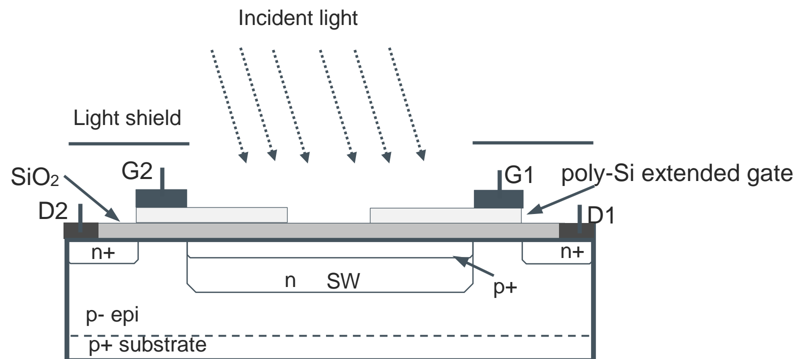

Figure 25: Cross section of a pinned photodiode detector [29], modified

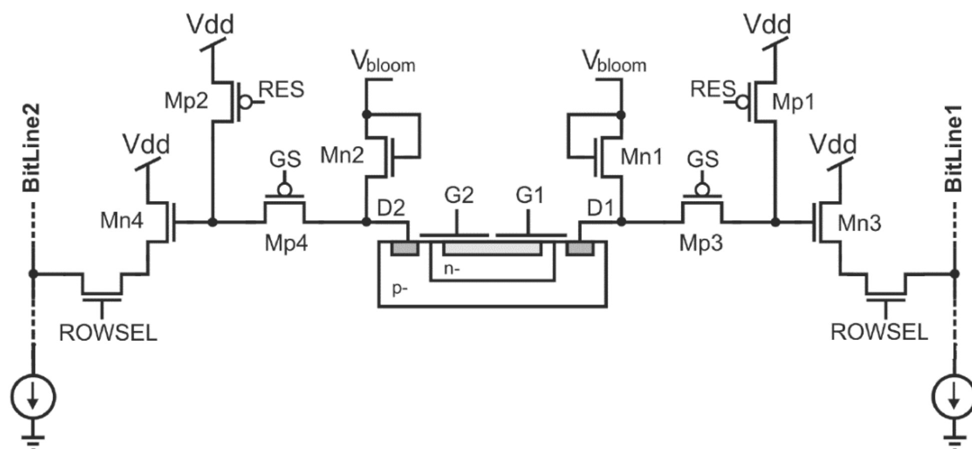

Figure 26: Pinned photodiode with a four-transistor (APS) configuration [29]

A functional description of the photo-demodulator integrated in a commonly used four-transistor (4T) APS configuration (Figure 26) is given as follows. At the beginning of the image acquisition, the floating diffusions are reset by the reset transistors Mp1 and Mp2. Next, the two transfer gates G1 and G2 are modulated so that the photo-generated charge in the pinned photodiode is completely transferred towards the collection nodes D1 and D2. To ensure a synchronous sampling of the de-modulated signal, a global shutter operation is implemented using transistors Mp3 and Mp4. In order to avoid blooming effects, when the full well capacity of the SW is exceeded and carriers diffuse away from the SW, two transistors Mn1 and Mn2 are diode-connected. Finally, the pixel is read out by selecting each row [29].

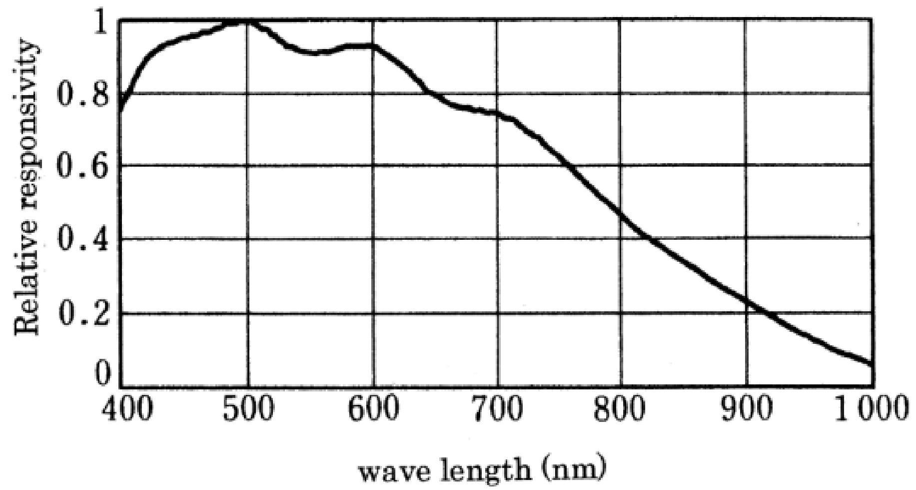

Figure 27: Spectral responsivity of a pinned photodiode [30]

A typical spectral responsivity of a pinned photodiode is given in Figure 27, showing that the maximum sensitivity is in the blue to green wavelength range. A requirement in TOF is a non-visible light source from this it follows that it is necessary to work in close to visible wavelength (e.g. 800nm).

2 State-of-the-Art TOF Image Sensors

In the last years, significant improvements have been made in order to achieve powerful, low-cost and compact 3D TOF devices. Especially the latest generation of sensors has shown, that 3D TOF cameras will have the potential to be indispensable for a numerous of applications. This chapter gives an account of recent State-of-the-Art developments in TOF technology published in literature especially in papers on Institute of Electrical and Electronics Engineers (IEEE) and discusses the strengths and weaknesses of several integrations based on this technology. Although commercially available TOF cameras will be reviewed.

2.1 Literature Research on TOF Sensors

The IEEE offers a comprehensive review on published approaches in subject to TOF. In the following chapters, publications of the last years have been consulted to describe the benefits of different TOF approaches. In succession these papers were organized by their photodetector principles leading to a breakdown of TOF sensor solutions.

2.1.1 SPAD based Sensor Solutions

SPAD-based image sensors enable fully digital distance computation with the consequence of generating high volumes of data which have to be managed. In literature, mainly four architectures exist which are differentiated by the processing and read-out unit namely: in-pixel, in-column, on chip or outside the image sensor (c.f. [31]). An in-pixel based SPAD architecture was introduced in a 128x96-pixel 3D image sensor fabricated by ST Microelectronics in a 0.13µm CMOS imaging process using a fully digital Phase-Domain Delta Sigma (PDΔΣ) approach [32]. The PDΔΣ architecture measures the phase difference between the envelope of the SPAD pulses and the outgoing light. A detailed description on PDΔΣ is given in [3]. Benefits of this architecture are mainly found in an increase in dynamic range and linearity compared to other phase domain approaches. The pixel profits from an optimized SPAD design in [33]. Indicating a median DCR, less than 100Hz with a pixel pitch of 44.65µm and 3.17% fill factor. Referred to [3] this approach has an excellent linearity of +/- 5mm in a 0.4- 2.4m range only limited by the photon pile up effect at short distances. Summarized, with such an SPAD based in-pixel sensor it is possible to manage a large volume of data produces by 3D Imagers without burden the host system.
Previously, C. Niclass et al. introduced a rangefinder and 3D-camera prototype with a 60x48-pixel image sensor in 0.35µm CMOS allowing the detection of light phase and intensity simultaneously [34]. The detection principle used in this imager is called Single-Photon-Synchronous Detection (SPSD) and it is almost equivalent to the process used in demodulation pixels described in chapter 1.7.2. In SPSD, the phase information is sampled directly by counting photons sequentially with a bank of counters (cf. [3]). In this approach, digital counters have the same function like analog storage capacitors. Because of the sampling nature in SPSD, constraints are given on the optical illumination system with restrictions in bandwidth. A significant development in this proposal is the simultaneously and independently acquisition performed in all pixels in combination with a full parallel read-out structure (Figure 28).

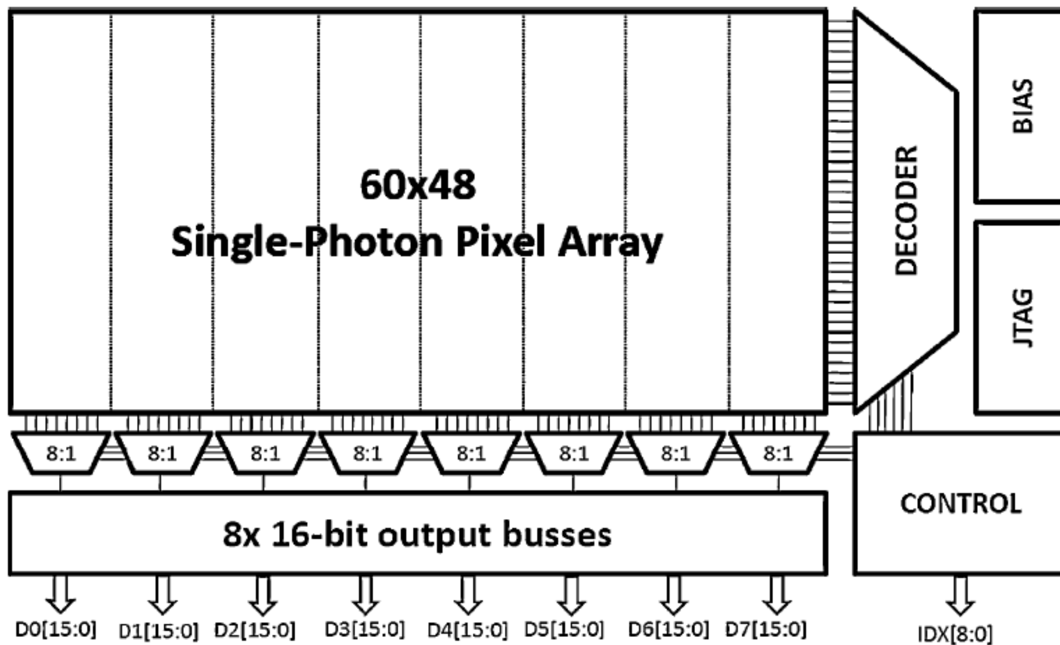

Figure 28: Chip architecture with parallel read-out mechanism [34]

With the use of a single clock, operating at 40 MHz, a frame acquisition and read-out time of 10.8µs, assuming a SPAD dead time of 40 ns, is stated for this approach. A drawback in this device is a low fill factor of 1%, which might be compensated using micro lenses [3].

Another SPAD based sensor, which should be reviewed because of its overall performance in terms of fill factor, distance range, relative precision, and operation under high ambient light, was introduced by C. Niclass et.al in [35]. The device was originally designed for automotive applications and because of its scanning mechanism, it is not feasible for many applications. Nevertheless, a SPAD implementation using macro-pixels was chosen providing a fill factor of 70%. A cross-section of a macro-pixel is given in Figure 29, where two adjacent p+/deep n-well SPADs with p-well guard-rings are shown. The reason for the high fill factor is found in the design that SPADs share a common deep n-well substrate. The entire macro-pixel measures 150x50µm² with a SPAD pitch of 25µm.

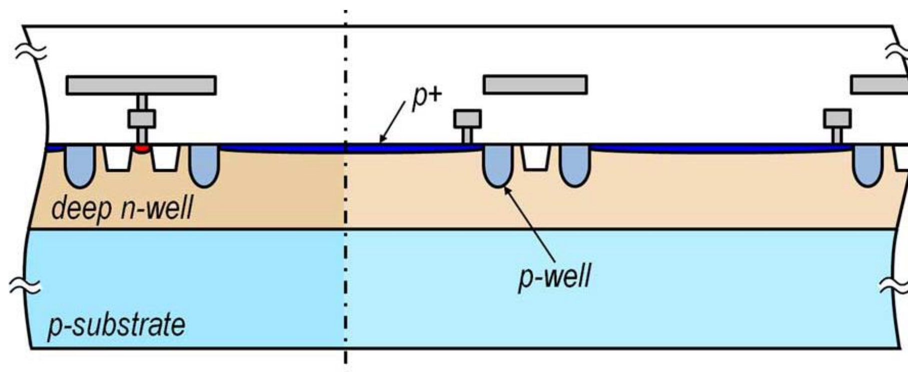

Figure 29: Cross section of a macro pixel [35]

In this device a temporal and spatial correlation of photons is used which increases the dynamic range and lowers the on-chip power consumption. The device achieved a repeatability error of smaller 10cm for a 100m

target under 80klux, leading to a relative precision of 0.1%. This is achieved by using a modified time-correlated-single-photon-counting (TCSPC) approach with the need of histogramming and further DSP processing [35]. An improved version is given in [36], using 16 macro-pixel for TOF ranging and 32 macro-pixel for background light intensity measurement in a 202x96-pixel 0.18µm CMOS on Chip (SoC) image sensor. The 16 TOF macro-pixels are next to an array of 64 time-to-digital converter (TDCs) and are driven by a PLL. An array of 32 SRAM blocks providing 768kb memory for on-chip DSP-processing is included (Figure 30).

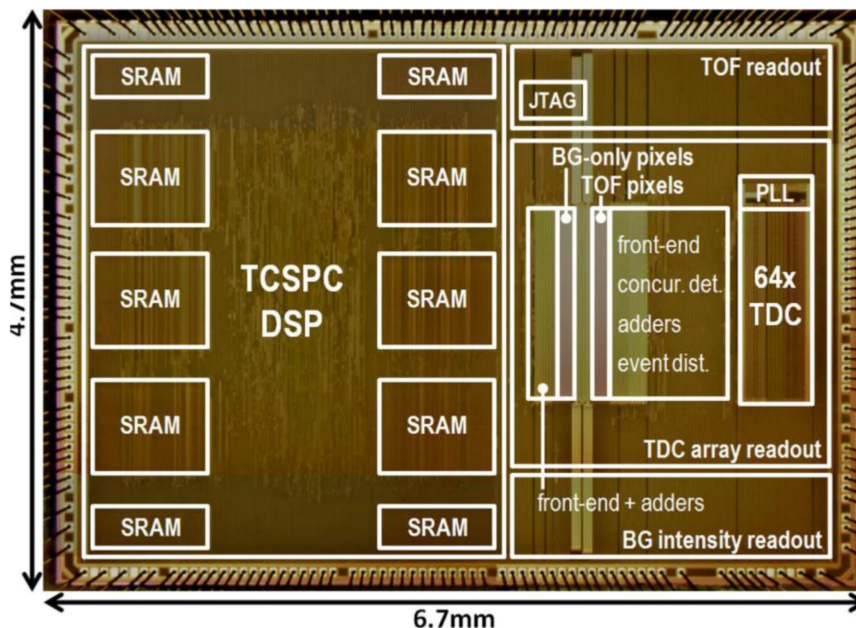

Figure 30: Chip die with system blocks [36]

Because of the costly implementation, multi-path scenarios, like capturing objects behind window glass, can be processed under high ambient light.

A 160×128-pixel sensor designed for FLIM and FRET applications, implemented in 0.13µm CMOS is introduced in [37]. The sensor is divided into 4 blocks of 80x64-pixel. Next to it, programmable region-of-interest (ROI) registers are implemented allowing selective readout of rows and columns. Each SPAD is connected to a TDC, which is composed of a ring oscillator. Thanks to this design, a TDC resolution of 55ps can be achieved. With further simultaneous two directional readout, a complete frame can be theoretically processed in 4µs.

Years before, a 32x32-pixel SPAD sensor with a simple on-chip, readout architecture was presented in [13]. Thereby each pixel consists of a SPAD a passive quenching circuit and a column access circuitry with a pixel fill factor of 1.1%. Because of a laser light source a very low power consumption for the illumination system of 750µW (mean power) could be achieved for this implementation. In addition, an accuracy of 1.8mm at 3m distance is stated for this device. The data processing is done by building up histograms using an array of depth measurements. The read out is performed sequentially with the drawback of losing some information (c.f. [3]). Nevertheless, good performance in 3D imaging is achieved with this approach. An accurate depth map profile of a human face obtained by the imager is given below.

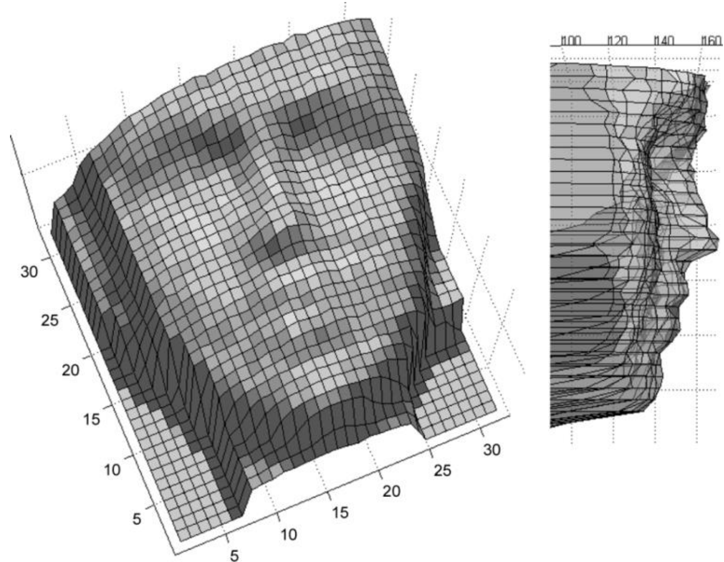

Figure 31: Depth map and profile (in millimeters) of a human face [13]

A further approach with a per-column readout is given in [38]. Whereby a latch less pipeline read-out (LASP) is implemented in a 128x128-pixel SPAD array. The benefit of LASP is that in addition to the time-of-arrival information also the row position where the pulse was generated is taken. Such an on-column readout design with 7.68Gbps through output is a powerful step towards parallelism [3]. In Figure 32 a block diagram of the proposed sensor is given, showing 32 TDCs whereby a group of four pixel is sharing one TDC. The TDCs are grouped in blocks of eight and are read out in parallel using a 4:1 event driven time-multiplexer. A row decoder is used to select each of the 128-pixel. For this sensor a TDC resolution of 97ps (1.4cm) is achieved but the overall 3D imaging quality compared to the previous 32x32-pixel did not improve well. Additionally, a costly large surface of 8x5mm² cannot be neglected.

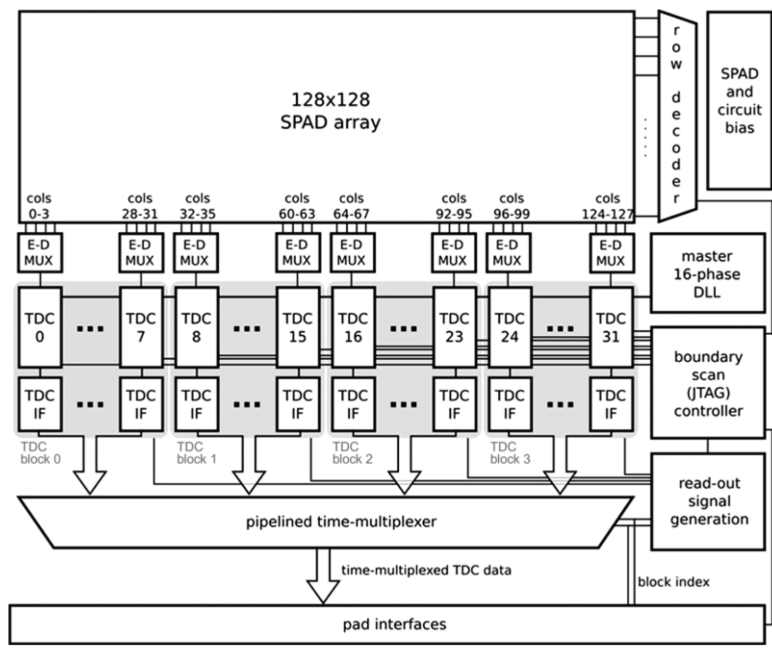

Figure 32: Imager architecture of a 128x128-pixel SPAD based sensor [38]

The next sensor, introduced by F. Villa et al. in 2013 [7] is a 32x4-pixel test structure designed in 0.35µm standard CMOS technology. The pixels are composed by a SPAD and one TDC each. The readout circuitry is based on a global Delay-Locked Loop (DLL) running at 160MHz providing 16 multiphase clocks of 400ps each. Compared to the previous discussed imager [37] , [38] this sensor shows better linearity and better SPAD performances with a lower timing resolution. An unneglectable drawback is the high power consumption of 6mW per channel for the designed TDC, putting a constraint on the field of application.

A novel paper published in 2015 reports from a TCSPC Sensor with full parallel histogramming TDC converter in 0.13µm 1P4M imaging CMOS process [9]. The sensor performance reads well, it can process 1.7Gphoton/s and generate 21k histograms/s with a readout time of only 4.6µs. Further a resolution of 71.4ps (1cm) is achieved. A benefit for this architecture is that the region of interest (ROI) can be programmed allowing high dark-noise pixels to be disconnected from the TDC input. The approximated total power consumption of the detector is 31.8mW. The following photomicrograph of the 2.4×1.7mm² device shows no DSP for on-chip histogram processing which depresses the mood because of the increase in costs arising for the overall system.

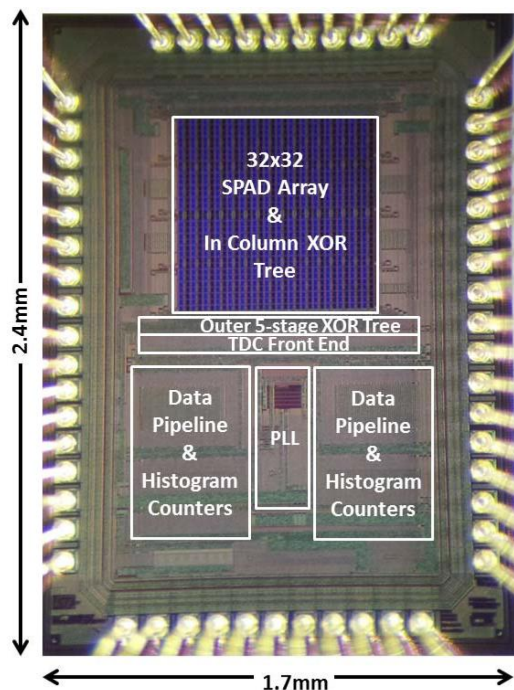

Figure 33: Photomicrograph of the device die, showing 32x32-pixel SPAD array and parallel histogram conversion [9]

On the next page an overall performance comparison table for the described SPAD based TOF sensors is given followed by an review on in-pixel photo mixing sensors.

Parameter		Unit	[32]	[34]	[35]	[37]	[36]	[13]	[38]	[39]	[7]
			R. J. Walker Robert K. Henderson et al. (Edinburgh UK, ST) ISSCC 2011	C. Niclass E. Charbon et al. IEEE 2009	C. Niclass Manabu Kagami et al. IEEE 2013	E. Veerappan Charbon et al. ISSCC 2011	C. Niclass et Manabu Kagami et al. IEEE 2014	C. Niclass Edoardo Charbon et al. IEEE 2005	C. Niclass E. Charbon et al. IEEE 2008	A. Neale W. Dutton, R.K. Henderson et al. ISSCC 2015	F. Villa, F. Zappa et al. (Milano) IEEE 2013
TOF Technology		-	Indirect TOF	SPSD	Modified TCSPC	TUPC/ TCSPC	TCSPC	TCSPC	TCSPC	TCSPC	TCSPC
Chip area		mm²	7.2 x 7.5	6.5x5.5	-	11x12.3	6.7x4.7	-	8x5	2.4x1.7	-
Technology Process node		-	0.13 µm imaging CMOS	0.35 µm HV2 CMOS	0.18 µm HV CMOS	0.13 µm	0.18 µm HV CMOS	0.8 µm HV CMOS	0.35 µm HV CMOS	0.13 µm STMicro. 1P4M imaging CMOS	0.35 µm Standard CMOS
Image sensor resolution		Pixels	128x96	60x48	340x96	160x128	202x96	32x32	128x128	32x32	32x4
Pixel Pitch		µm	44.65	85	-	50	-	-	25	21	-
Pixel fill factor		%	3.17	1	70	1	70	1.1	6	43	3.14
Median Dark Count Rate		Hz	<100	245	-	50	-	350	694	-	60
Frame Rate		fps	20	22	10	25k	10	-	-	-	10 (3D)
Target Reflectivity		-	white	white	white	-	9%	-	-	-	-
Unambiguous distance range		m	45	5	128	8	128	3	3.75	-	60
Illumination optical power		mW	50	800	40	2	21	100(peak) 0.750 (mean)	1	-	0.1
Illumination wavelength		nm	850	850	870	350-900	870	635	635	425nm	555
Narrowband optical filter width		nm	40	40	-	-	-	-	11	-	-
Illumination modulation frequency		MHz	3.33	30	0.2	-	0.133	50	40	-	80
PDP at illumination wavelength		%	5	31	-	3-27.5	-	12	35.4 at 460nm	-	-
Illumination field of view (HxV)		°	40x40	50x40	170x4.5	-	55x9	-	5	-	-
Integration Time		ms	50	45	-	-	44	-	50	-	800
Time Jitter at FWHM		ps	-	-	-	140	-	115	250	-	90(520nm)
Repeatability	1 σ distance resolution	cm	16	3.8	<10	14.2	-	-	1,4	approx. 1	-
	Max. distance	m	2.4	2.4	100	100	-	-	3.6	-	-
	Background light	klux	0.11	0.15	80	70	-	-	.15	-	-
Non-linearity	Max. error	cm	0.5	11	36.6	11.3	-	-	0.9	-	-
	Max. distance	m	2.4	2.4	100	100	-	-	3.75	-	-
	Background light	klux	0.11	0.15	80	70	-	-	0.15	-	-
Chip power dissipation		mW	40	35	-	550	530	<6	-	14,1mW TDC	-
Application			3D imaging	3D imaging	3D imaging	FLIM, FRET	3D imaging	3D imaging	3D imaging	3D imaging Automotive	3D imaging

Table 3: SPAD based sensor solutions

2.1.2 In Pixel based Sensor solutions

Compared to sensors based on SPAD, which require a pico-second laser source to be effective, in-pixel based sensors have not that stringent requirements on the illumination source. Additionally in SPAD, TDC structures may occupy as much area as the pixels itself, making it necessary to go to smaller processes nodes in order to be scalable to larger arrays. A constraint in 3D imaging for SPAD based sensors is their light sensitivity. Hence, they need optimized pixel structures or costly DSP processing (c.f. [36]) to prevent pile-up effect.

To start with, an 80×60-pixel lock-in detector in 0.18µm CMOS is presented in [29]. Based on a pinned-photodiode structure a pixel pitch of 10µm and a fill factor of 24% is stated. A functional description including a cross-section of this photo-demodulator with 4T APS configuration was already described in chapter (1.7.2.8). As reported, this imager works up to a modulation frequency of 50MHz. The 3D imaging sensor performance was tested by using an 850nm, 20MHz LED light source, delivering 80mW optical power to the scene. A 3D depth map obtained by the imager showing its capability is given in Figure 34 below.

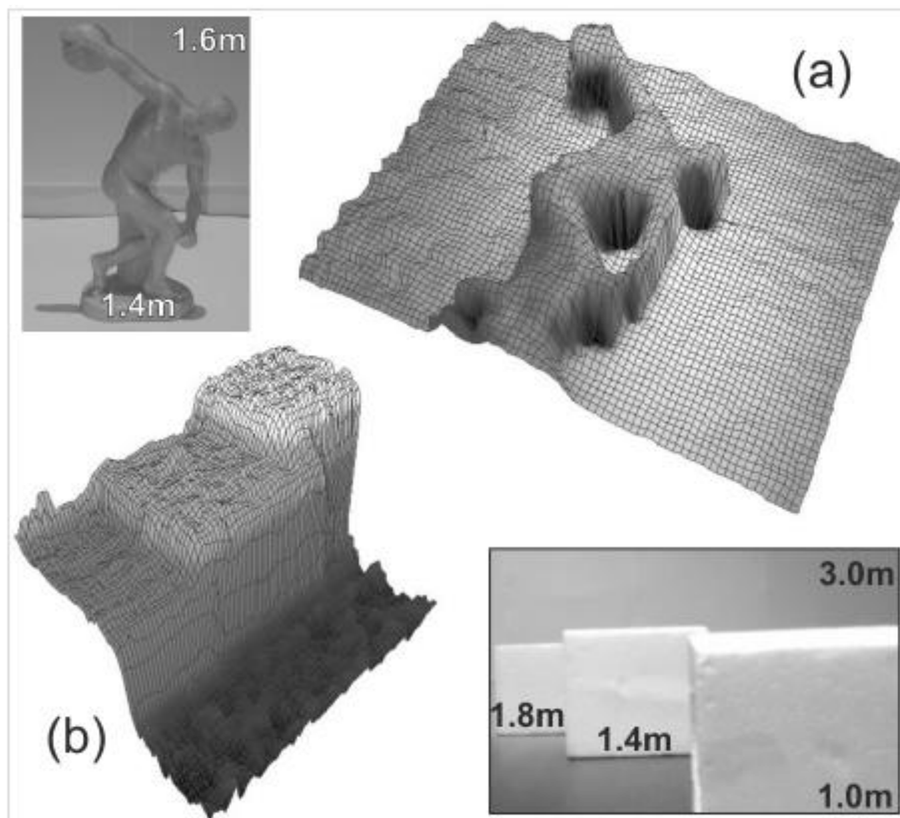

Figure 34: TOF depth map and original picture of two scenes
a) 100frames with 100ms integration time at 100lx
b) Single shot with 200ms integration time under dark conditions [29]

The next two sensors introduced here, serves consumer applications that require a monolithic integration for a single-lens camera system, capturing color and TOF range images simultaneously, for use in small-form-factor cameras with lowest-possible costs. This generation of TOF sensors based on pinned-photodiodes presented in [40] have been introduced by S.J. Kim et al., at Samsung Institute of Technology in [41]. One year later from the same development center W. Kim et al. introduced in [42] a camera prototype generating a real-time 3D

model of an arbitrary scene. It consist of a 1.5Mpixel RGBZ imaging module where color (RGB) and range (Z) pixels are tiled across the image plane as can be seen below:

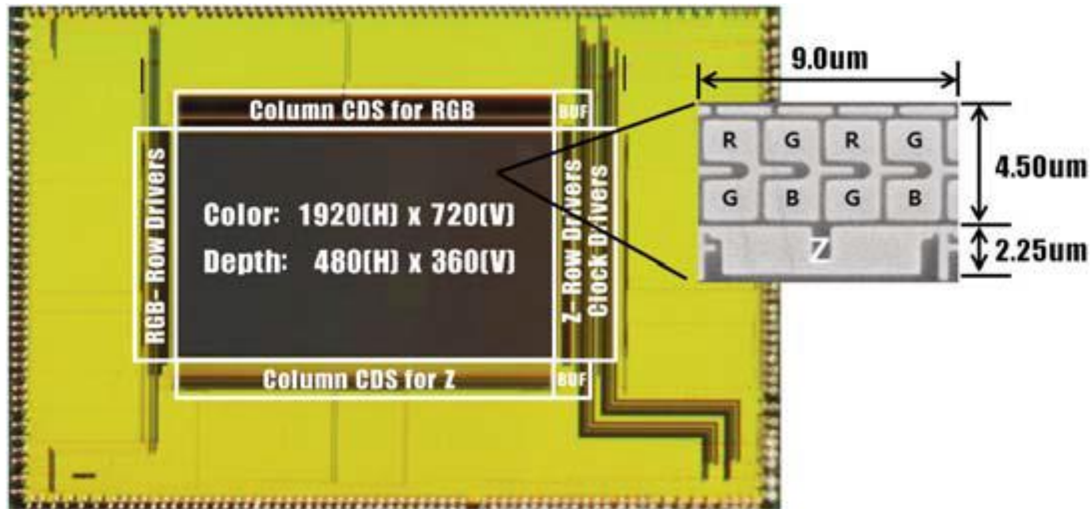

Figure 35: Microphotograph of the 1.55Mpixel sensor with approx. 70mm² total die size [42]

Overall there are, two interlaced arrays: a 1920×720-pixel physical array of color pixels consuming approx. 7mm² of surface and an embedded 480×360-pixel array of range pixels consuming approx. 10.5 mm² die space for a total of 1.55Mpixels on chip. The ADC and TOF signal processing is performed off-chip. The principle of operation for this color sensor is given as follows. Both the modulated infrared light and ambient light can penetrate RGB color filters placed on top of each color pixel, whereas a filter on top of the Z pixel is aligned on the modulation frequency and let only these spectral parts pass. An additional potential barrier below the color pixels prevents the photo-electrons generated by modulated infrared light to move towards the RGB photodiodes. The imaging performance of this approach is given in Figure 36.

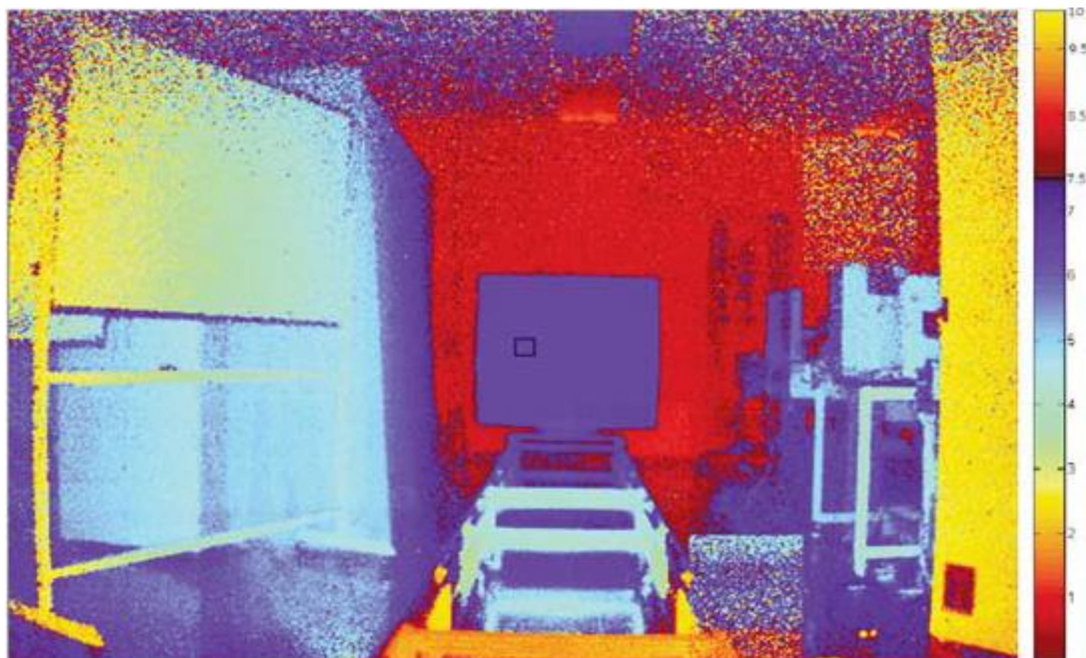

Figure 36: Colored distance representation of the scene, obtained with Z-pixels (480×360). Because of 20MHz modulation frequency, the distance and hence the color range repeats every 7.5m [42]

As can be seen in Figure 36, the image quality leaves much to be desired. An image signal processor (ISP) was already used to prevent pixel noise. Additionally efforts are announced mainly on the optimization of the potential barrier to reduce crosstalk and a backside illuminated RGBZ sensor [42].
The following in-pixel photodetector for distance measurement provides a TOF-pixel circuit managing very high ambient light up to 120klx. The 2×32-pixel sensor chip fabricated in a 0.6µm Bi-CMOS process was presented by the group of Horst Zimmermann et al. in [43]. This sensor uses TOF correlation method, extensively described in [3]. The total chip area is about 6.5mm², which includes 100×100µm² photodiode area, logic unit, output buffers and a ring oscillator plus PLL. The pixel fill factor is about 58% and the power consumption is ~0.1mA/pixel from a 5V supply and have been decreased to the factor of six compared to [44]. The same group reports an optimized pixel circuit without an operational amplifier as it was still required by the previous design, whereby the current consumption per pixel could be reduced by a factor of 50, in [45]. The following picture shows the 3D imaging capability for this device capturing four different gestures.

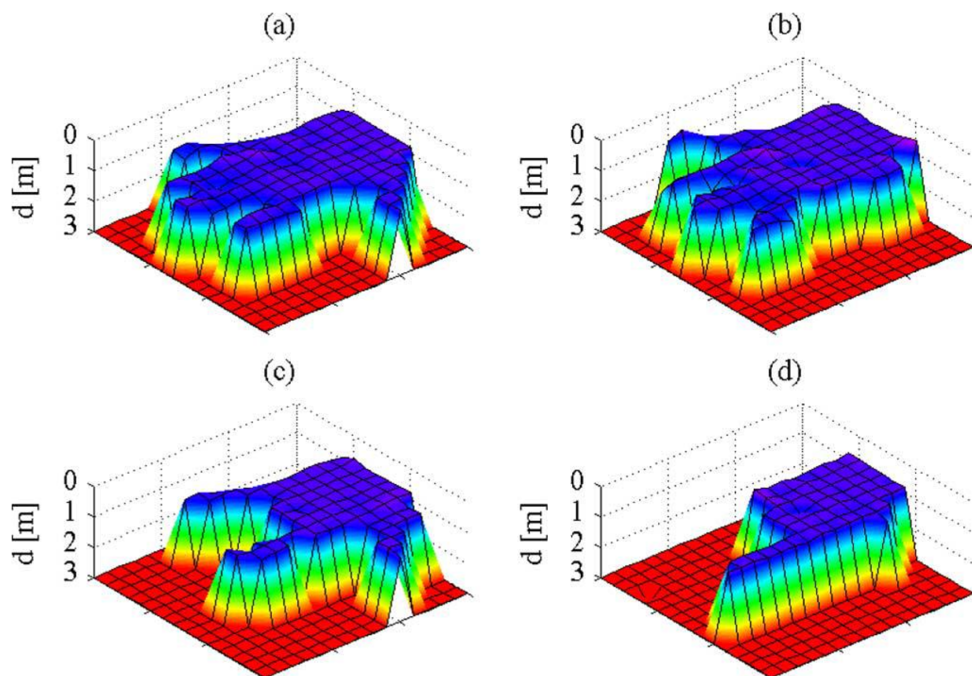

Figure 37: Depth map of a scene using 16 fps with external ADC [45]

It shows that a 16x16pixel structure is sufficient for gesture recognition. A drawback is definitely the overall system power consumption of correlation-based sensors of 10W in this case, mainly dominated by the active illumination source. This makes such a system suitable for industrial applications but not for battery-powered applications. By the same design group an improvement in terms of power consumption and pixel size have been reported in [46], for a single pixel range finding sensor in 2.5 V CMOS 90nm 1P9M process. This sensor provides higher background light suppression (120klux) compared to the commercial available MESA SR4000. M. Davidovic et al. presented a further optimization of this pinned-photodiode based sensor one year later providing 180klux background light suppression [47].
However, years before in 2001 a photodiode based CMOS range imager integrated in a standard 0.5µm CMOS process (3MIP) was presented by Ralf Jeremias et al. member of Fraunhofer Institute of Microelectronic Circuits and Systems, Duisburg, Germany. The two-lined 32x2-pixel array was characterized with a laser light source providing 10ns pulses and an optical diffuser to widespread the laser beam. The sensor shows good range

resolution lower 1cm within burst operation (100pulses). The advantage of this sensor is the immunity against high background illumination, even direct sunlight. On the one hand, this is achieved because of extremely short pulses and shutter times (below 30ns) on the other hand the light falling on the chip circuitry is blocked by a metal3 shielding in layout [48].
The sensor described in [49] and [50] counts to a fully differential pixel concept for I-TOF 3D measurement. The architecture is in detailed described in [3] and out of this, some advantages can be stated as follows:

- The background illumination can be cancelled effectively
- The circuit is simple to analyze
- Low offsets and reliability

Drawbacks are the "wasted" area of the dummy diode and due to high noise, mainly effected by kTC[1] noise.
The performance table of the 16x16-pixel image sensor, fabricated in a 0.35µm 3.3V CMOS technology is promising. The overall power consumption of the chip is 47mW (pixel power consumption 100µW) in real time 30fps operation, this is much better compared to the earlier discussed 16x16-pixel array in [45]. The sensor provides an accurate range map from 2m to 9m with a background light rejection up to 60klux. In terms of scalability, the main drawbacks of this device are the reduced fill-factor 20% and large pixel pitch of 80µm.
The next sensor being reviewed is a 160x120-pixel range sensor implemented in a standard 0.18µm CMOS presented by M. Perenzoni et al., University of Trento in [51] and [52]. The target application field is ambient-assisted living field [53], which focuses mainly on user interfaces. Therefore, requirements are low-cost sensors with moderate depth resolution, but a high field-of-view. Additionally, background light immunity is desired due to the high variety of illumination conditions (windows, artificial light). Compared to the previous sensor specifications, this approach shows better fill factor of 34% and smaller pixel pitch 29.1µm. Because of the increased pixel size, a power consumption of approximately 315mW is calculated for the chip, effectively preventing it from battery-operated devices.
On the next pages an overall performance comparison table for the described in-pixel based TOF sensors based on pinned-photodiodes is given.

---

[1] The kTC noise is a fundamental noise associated with the conversion of charge signal to voltage signal or vice versa [54].

Parameter		Unit	[29]	[42]	[41]	[43]	[45]
			David Stoppa Lorenzo Gonzo et al. (Trento) ISSCC 2010	Wonjoo Kim Eric Fossum et al. (Samsung) ISSCC 2012	Seong-Jin Kim Chang-Yeong Kim et al. (Samsung) VLSIC 2011	Gerald Zach Horst Zimmermann (University of Vienna) ISSCC 2009	Gerald Zach Horst Zimmermann et al. (University of Vienna) IEEE 2010
TOF Technology		-	CW-TOF	CW-TOF	CW-TOF	Indirect TOF	Indirect TOF
Chip area		mm²	-	-	6x6	6.5	3.3x3
Technology Process node		-	0.18µm Imaging CMOS	0.13µm FSI CMOS	CMOS 1P4M 0.11µm	0.6µm Bi-CMOS process	0.6µm Bi-CMOS process
Image sensor resolution		Pixels	80x60	480x360	640x480	2x32	16x16
Pixel Size		µm²	10µm (pitch)	2.25x9	6µm for color image 12µm for depth image 6x6	109x158	125x125
Pixel fill factor		%	24	48	34.5	58	66
Frame Rate		fps	-	-	-	50ms	16
Target Reflectivity		-	-	-	-	-	-
Unambiguous distance range		m	0.2-6	7.5	1-3	0.1-3.2	0.1-3.2
Illumination optical power		mW	80	450 (input)	-	900 (4LEDs)	900 (4LEDs)
Illumination wavelength		nm	850	850	850	850	850
Narrowband optical filter width		nm	-	RGB Color filter (Z-pixel)	-	-	-
Illumination modulation frequency		MHz	20	20	10	10	10
Integration Time		ms	-	-	50	-	-
Repeatability	Accuracy	cm	(<4cm best) 16cm	0.5	1-6	<2 (7)	<1
	Max. distance	m	6	1	1-3	1.2 (3)	1
	Background light	klux	-	-	-	Up to 120	Up to 150
Non-linearity	Max. error	cm	0.7%	2.5%	0.8	2cm	-1/+2cm
	Max. distance	m	6	7	1-3	3.2	0-3.2
	Background light	klux	-	0.3	-	120	Up to 150
Chip power dissipation		mW	-	-	-	~0.1mA/pixel @5V	10W
Year		-	2010	2012	2011	2009	2010
Note				RGBZ image sensor (color and range)		Fully electrical in-pixel Without optical filter ring oscillator	Fully electrical in-pixel
Application			3D imaging	3D imaging	2D/3D imaging	3D imaging High ambient light	3D imaging High ambient light

Table 4: Pinned-Photodiode based sensor solutions (1)

Parameter		Unit	[48]	[49]	[50]	[52]	[51]	[40]	[46]	[47]
			Ralf Jeremias Peter Mengel et al. (Fraunhofer Institute, Siemens) ISSCC 2001	David Stoppa Luigi Viarani et al. (Trento) IMTC 2003	David Stoppa Gianmaria Pedretti et al. (Trento) 2004	Matteo Perenzoni Lorenzo Gonzo et al. (Trento) 2010	Matteo Perenzoni Lorenzo Gonzo et al. IEEE 2011	Seong-Jin Kim Chang-Yeong Kim et al. IEEE 2010	Milos Davidovic Horst Zimmermann et al. (Vienna University) 2010	Milos Davidovic Horst Zimmermann et al. (Vienna University) 2011
TOF Technology		-	Indirect TOF with electronic shutter	Multiple pulse Indirect TOF	Multiple pulse Indirect TOF	Indirect TOF	Indirect TOF	Indirect TOF	Indirect CW TOF	Indirect CW TOF
Chip area		mm²	42	-	3.04x3.3	4.65×3.49	4.65×3.49	-	-	-
Technology Process node		-	0.5μm CMOS process (3MIP)	0.35μm, 3.3V CMOS	0.35μm, 3.3V CMOS (2P-3M)	0.18μm 1P4M 1.8V CMOS	0.18 μm 1P4M 1.8 V CMOS	0.18-μm 2P3M CMOS	90nm 2.5 V CMOS 1P9M	180 nm 1P6M CMOS
Image sensor resolution		Pixels	32x2	16x16	16x16	160x120	160x120	64x16	1	1
Pixel size		μm²	260	80x80	80x80	29.1 (pitch)	29.1 (pitch)	12x12	50x57	40x40
Pixel fill factor		%	-	20	20	34	34	60	90	67
Frame Rate		fps	Up to 20k	-	30	Max. 80	458(2D) 80(3D)	-	20	100
Target Reflectivity		-	-	-		White 40%	40%	-	-	White 90%
Unambiguous distance range		m	>5m	-	2-9m	4.5	4.5	4	30	3.2
Illumination optical power		mW	Class 1 laser	-	50	2.89	2.89	-	1.2	1
Illumination wavelength		nm	-	-	658	905	905	850	650	650
Narrowband optical filter width		nm	-	-	-	-	-	-	-	-
Illumination modulation frequency		MHz	-	-	-	-	-	5	5	12.5
Repeatability	Accuracy	cm	+-1	-	1	10cm		2%(4%)	<10cm	4
	Max. distance	m	10	-	2-9	1		1 (4)	3.2	3.2
	Background light	klux	10	-	<60	-		-	120	180
Linearity	Max. error		<5%	1.4%	<1.4%	-		-	+-10cm	+-5
	Max. distance	m	10	-	2-9	-		-	3.2	3.2
	Background light	klux	10	-	<60	-		-	120	180
Chip power dissipation		mW	330	0.1	47	-	-	-		-
Application			3D imaging	3D imaging	3D imaging	3D imaging	3D imaging	3D imaging	Range finding	Range finding

Table 5 Pinned-Photodiode based sensor solutions (2)

Beside of pinned-photodiode based imagers further CMOS range sensor have been presented in the last years. One of it is a 32×32-pixel array based on Current-Assisted Photonic Demodulator (CAPD), presented in [54] and [55]. The pixels measure 30µm × 30µm with a Fill-Factor of 66%. Furthermore, a modulation contrast of 51% at 20MHz is stated for this device. The characterization have been performed using a camera system with 100mW optical power, a 3mm 1:1.7 miniature lens and a VIS-cut optical filter with 90% transparency at 870nm. It shows that a good distance linearity was observed from 1m to 6m as well as a distance accuracy of 3cm at 2m is measured at 250fps. The capability of the presented imager for 3D imaging is shown below:

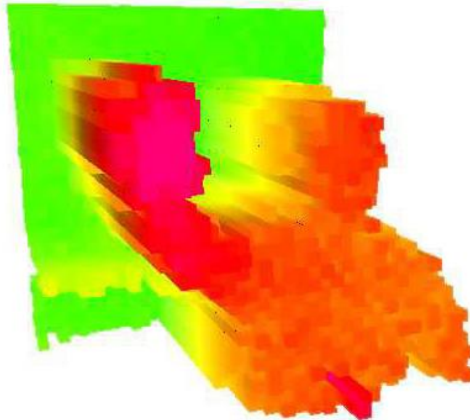

Figure 38: Colored 3D depth map obtained by a 32x32-pixel CAPD TOF 3D-imager [55]

The next 120x160-pixel CAPD imager was presented in [56] by the University of Trento, Italy in 2011. The total chip power dissipated is about 200mW (10µW per pixel) mainly determined by the high-power LED light source delivering 140mW optical power on the target. For testing, a camera objective (f=2.9mm, F/1) was mounted in front of the sensor chip, while a collimating diffuser was used to match the illumination field with the camera field of view (23°×30°). Distance measurements of a white diffusing target were acquired in the presence of ambient light at 30ms integration time per frame (corresponding to seven 3D fps) and in the range from 1.2m to 3.7m, showing a maximum linearity error between the real and measured distance of 3.3%, and a distance non-uniformity among the pixels lower than 2cm. The 3D ranging capability of the sensor have also been demonstrated by acquiring 3D videos at 7fps.

The final sensor reviewed here, have been introduced in [57]. This imager is based on a CCD/CMOS 1-tap demodulation pixel. Because of its only 1-tap, the usually four sampling points have to be acquired sequentially. The LED illumination provides an optical output of about 900mW. Distance measurements have been performed with an integration time of 100µs to 100ms. With a maximum modulation frequency of 20MHz, the maximum distance range is 7.5 m. With the use of two separate illumination units, a ranging accuracy of better than 5 cm over the full distance range have been achieved.

The overall specifications of the reviewed CAPD and CCD imagers are summarized in Table 6.

Parameter		Unit	[54], [55]	[56]	[57]
			Ward van der Tempel Maarten Kuijk (University of Brussel) et al. 2008	Gian-Franco Dalla Betta Giovanni Verzellesi (Universities of Trento, Pavia, Modena) et al. CLEO 2011	Robert Lange and Peter Seitz IEEE 2001
TOF Technology		-	CW-TOF	CW-TOF	CW-TOF
Chip area		mm²	-	2.5×2.5	-
Technology Process node		-	0.35m standard CMOS technology	0.18µm CMOS	2.0µm CMOS/CCD process
Image sensor resolution		Pixels	32x32	120x160	64x25
Pixel Size		µm²	30x30	10×10	65 x 21
Pixel fill factor		%	60	24	>20%
Frame Rate		fps	25	7	-
Target Reflectivity		-	Near 100%	White diffusing	-
Field of view		°	-	23×30	-
Unambiguous distance range		m	0-6	1.2-3.7	7.5
Illumination optical power		mW	100	140	Few hundreds
Illumination wavelength		nm	870	850	630
Narrowband optical filter width		nm	-	-	-
Illumination modulation frequency		MHz	20	20	20
Integration Time		ms	-	30	100µs to 100ms
Repeatability	Accuracy	%	Sub cm 3(15)	3.3%	5cm
	Max. distance	m	Up to 2m 2(5)	1.2-3.7	7.5
	Background light	klux	-	-	-
Non-linearity	Max. error	%	-	3.3	260ps
	Max. distance	m	1-6	1.2-3.7	-
	Background light	klux	-	-	-
Chip power dissipation		mW	1.5	200	-
Application			Range measurement	3D imaging	Range camera

Table 6: CAPD and CCD based sensor solutions

2.2 ST Microelectronics VL6180

A commercial available TOF product based on SPAD is ST's proximity and ambient light sensing (ALS) chip ST VL6180. This TOF sensor was designed for use in smartphones and portable touchscreen devices as well as tablets, laptop and gaming devices and finally domestic appliances like industrial devices. The main specifications have been abstracted from the data sheet, as given below:

Parameter	Unit	ST VL6180
Feature	-	Ambient Light Sensor Proximity Sensor VCSEL Light Source
Package	-	Optical LGA12
Dimensions	mm	4.8x2.8x1
Measurement range	mm	0-100
Framerate	fps	45 (3D imaging)
Sampling rate	Hz	10
Total power consumption	-	<2.8µW Standby @2.8V 840µW ALS @2.8V 4.76mW Ranging @2.8V ~300mW optical power (average)
Illumination wavelength	nm	850
Viewing angle (HxV)	°	42 (half angle)

Table 7: Specifications of ST-VL6180 device [58]

For the illumination system the ST-VL6180 uses a VCSEL light source modulated at 100MHz with a pulse with of 3.3ns which can be reduced to 1.5ns and a period of 10ns. For the measurement of TOF 6.6ns are used of this period and the rest 3.3ns for ambient light measurement. A total power consumption for the illumination system of approximately 300mW on average is calculated. The sensor was designed in a hybrid CMOS 90-130nm process. On top of the approximately (6x6) SPAD array a glass filter is added which consists of two filter layers. The specified measurement range reduces with background light to 4cm. For the readout an analog DLL circuit is used which was patented in [59]. The die size is about 5mm² whereby 3mm² are used by the digital core, microprocessor and interface. A complex package with two chambers separated by an optical barrier is used to have a reference start pulse for the TDC. A cross section of the sensor interiority is given in Figure 39.

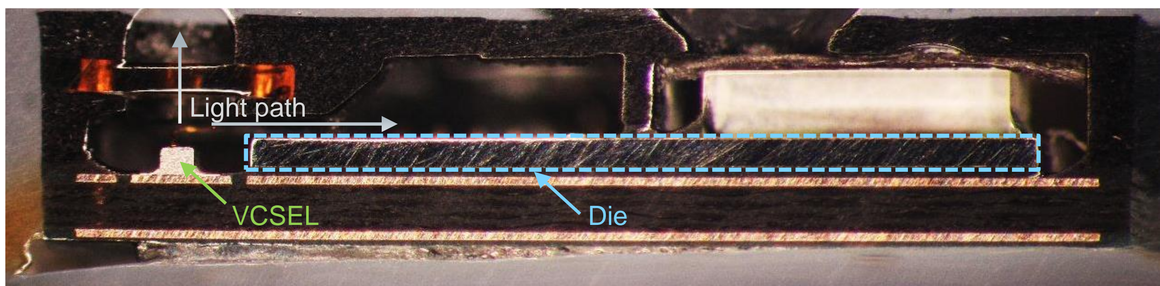

Figure 39 Cross section of the ST VL-6180 sensor

The photomicrograph shows the costly packaging. On the left hand side the VCSEL with its two corresponding light emitting paths is shown. One (above) towards the scene and to (the right) a reference diode can be found. As can be seen the VCSEL is placed beside of the sensor die separately. The rectangular shaped white form is the optical filter, which is placed on top of the SPAD array.

2.2.1 Performance of LG G3 using VL6180 Autofocus with TOF

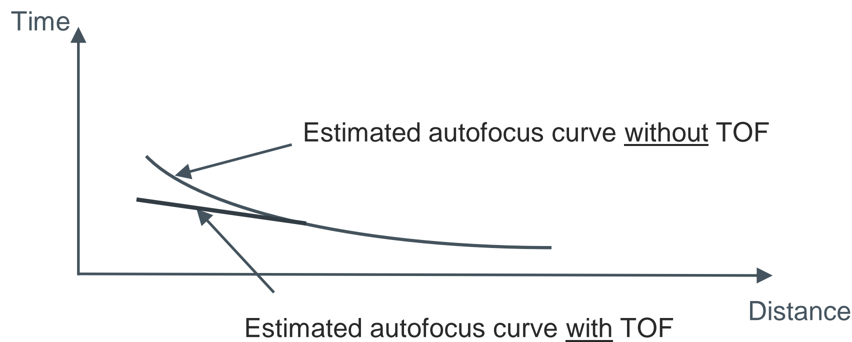

Figure 40: Estimated time over distance curves with and without TOF assistance

As shown in Figure 40, it is estimated that the autofocus time for short distances will increase without TOF assistance, mainly caused by the algorithm. Autofocus times for the HTC One (M8) and Samsung Galaxy S5 promise 300ms. This is the approach where a TOF assisted autofocus is an advantage. LG stated for their LG G3 using the VL6180 for autofocus assistance a timing of 276ms [60]. In the following practical sections, the timing benefit will be reviewed as well as the results evaluated.

2.2.1.1 Measurement Setup

The autofocus time of the LG G3 phone is measured for distances from 5cm to 150cm. Two measurement setups have been implemented. One with and one without TOF sensor. Therefore, the LG's Time-of-Flight sensor (ST- VL6180) is covered with an untransparent sticker, so that no IR-light can hit the scene. In both setups a white indoor wall is used as a target. The LG G3 is placed on a chair and the distance steps are measured with a tapeline. The elapsed autofocus time is then measured with a stopwatch app on a second smartphone. In order to not allow the camera to autofocus, on each beginning of every measurement an untransparent sheet is placed directly in front of the camera. An example of a measurement procedure is given as follows:

1. The camera is placed on a specific distance e.g. 150cm in front of the wall.
2. The shutter is held on the camera front.
3. Then the shutter is removed quickly and the start impulse for the stopwatch is given as fast as possible.
4. The clock is stopped by hand when the autofocus symbols appear on the display.

The main measurement inaccuracies occur because of the time delays during interaction by hand. Below an illustration and pictures of the measurement setup are given in Figure 41 and Figure 42.

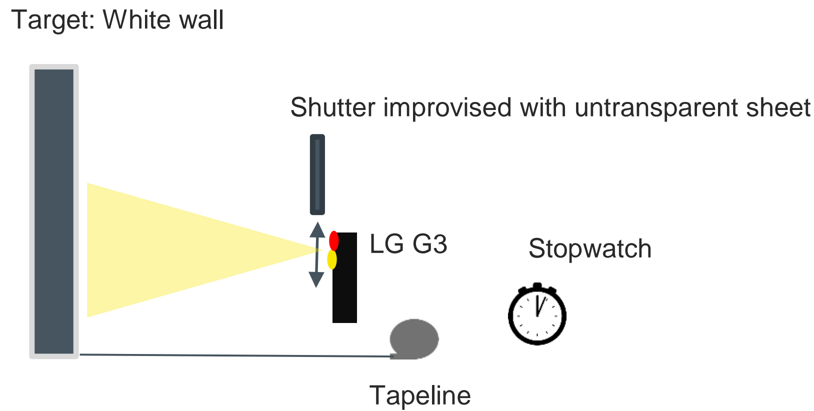

Figure 41: Schematic illustration of the measurement setup including their components

Figure 42: Non-laboratory testing environment

2.2.1.2 Measurement Results

For the autofocus time measurement, a couple of results are counted to state a range. It must be noticed that the time results have an inaccuracy of assumed 400-600ms, caused by the operation by hand and the distance might have an error of +-1cm. The “good results” are meant to be the usable autofocus results out of a series of 10 repeated measurements. In addition, the ambient light is also measured with a smart phone app. The lux values vary because of the ambient light situation in the measuring room.

The acquired time data’s are plotted as a function of the distance for both cases (Figure 43). The results correspond with the estimated waveform whereby the trend is clear. The best timings have been around one second with this measurement setup. If subtracting the measurement error the stated timings of 276 milliseconds seems to be realistic. More interesting in this overall measurement series is the fact that the probability for usable, autofocused pictures dramatically increase for short distances with TOF assistance. As can be seen in Figure 44, at 20cm distance the probability of capturing sharp pictures is still 100% with TOF

assistance compared to 70% without TOF. Another aspect should be mentioned, even with the use of TOF, correct autofocus results cannot be obtained at distances of 5cm and below. At these short distances, the autofocus algorithm is still offbeat. In appendix, the underlying measurement results of the following diagrams are listed.

2.2.1.3 Diagrams

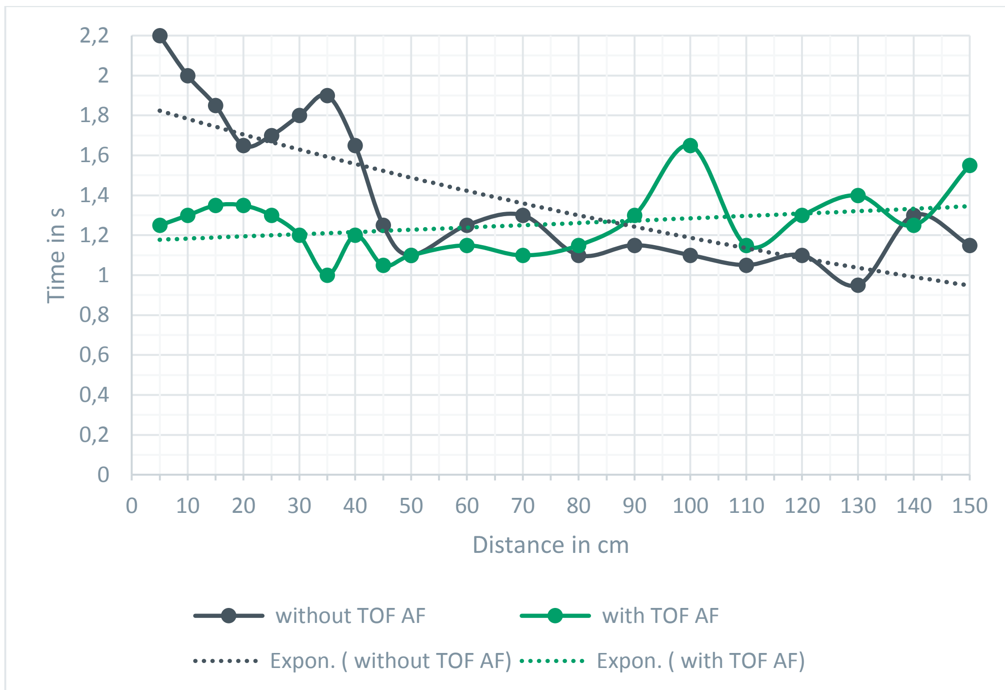

Figure 43: Measured timings for the LG G3 as a function of the distance

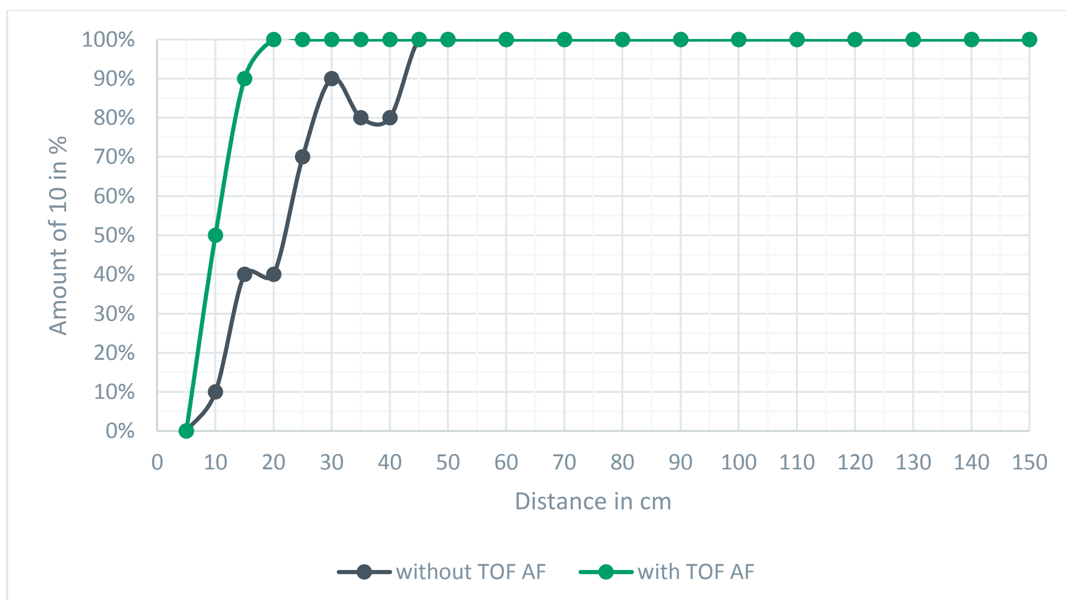

Figure 44: Probability of capturing focused pictures as a function of the distance

2.3 PMD CamBoard pico

To start with, some general information on the device will be given. The PMD CamBoard pico is a 3D TOF imaging camera with a small form factor based on the PMD (photonic mixer devices) principle (c.f. chapter 1.7.2.6). It provides high framerate (45fps in 3D) and is intended for capturing fast movements of fingers and hands for implementing smooth touchless gesture recognition in all-in-one PCs and laptops. The heart of this device is the Infineon 3D TOF image sensor IRS1010C based on the in-pixel PMD principle. The specifications for this camera system are given below followed by an image of the device interiority:

Parameter	Unit	PMD CamBoard pico
Dimensions	mm	89x17x6 incl. housing
ToF- Sensor		IRS1010C Infineon 3D Sensor IC
Measurement range	cm	20-100
Framerate	fps	45 (3D imaging)
Acquisition time per frame	ms	4.9
Power consumption	W	1-2
Illumination wavelength	nm	850 (LED)
Resolution	pixel	160x120
Viewing angle (HxV)	°	82x66
Depth resolution	mm	<3 @ 50cm <6 @ 100cm

Table 8: Specifications CamBoard pico [61]

Figure 45: PMD CamBoard pico [62]

A block diagram for the device is given in Figure 46, showing the main building blocks, which are the 160x120- pixel PMD in-pixel sensor matrix, which receives the incoming IR-light from the scene and is controlled by a modulated signal from a modulation driver. This modulation signal is used for shutter operation respectively charge separation as described in chapter 1.7.2. The readout is performed by an A/D-converter driven by a sequence controller, providing the digital 3D imaging data's for an external host controller. The illumination system consist of a multiple LED light source, which is driven by an Illumination driver.

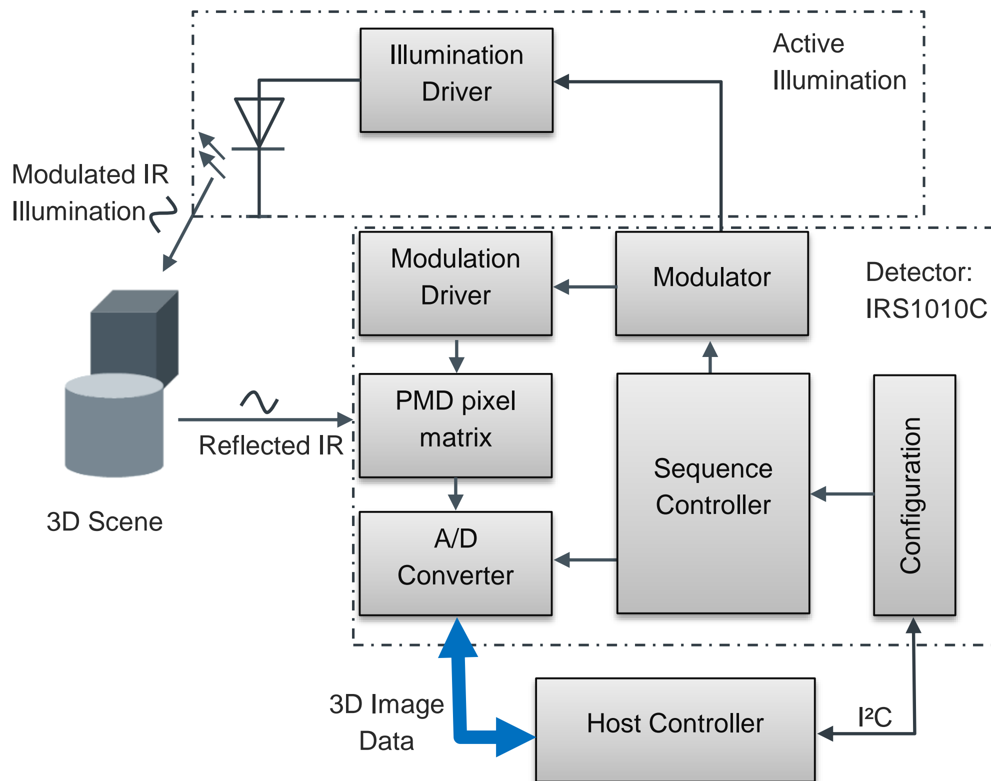

Figure 46: Block diagram of the PMD Cam board pico device [62], modified

2.3.1 Review on PMD CamBoard pico

On the next pages a review on the PMD Cam Board Pico will be given. The capability of the 3D imager will be demonstrated as well as borderlines for this in-pixel based TOF camera are shown. To start with a "greeting-picture" from the author is given, captured by the PMD device.

Figure 47: Imaging capability of the PMD device

For the PMD device a dedicated software tool for developers based on C++ is available and several software development kits. Additionally, a large online community is grown up concerning this product [63].

The picture above was captured with the user-friendly LightVis software tool, which will be in further consequence used for the following investigations. This software tool provides main controllers for the frame rate, integration time and modulation frequency. Additionally, post processing controls are integrated which mainly consist of averaging and filtering options.

The first test was done to see the influence of the integration time on the signal quality without post processing respectively any software improvements. The following pictures were captured under office light conditions (320-500lux) [64]. Furthermore, a modulation frequency of 30MHz was adjusted. The distance information for every pixel will be given in RGB graded colors, which is a software adjustment. A red pixel for instance corresponds to a near distance whereas a green colored pixel indicates a far distance.

As can be seen in the following picture (Figure 48), the quality of the raw image leaves much to be desired. Without post processing and using 100µs integration time the scene is completely noisy, hence, distance information is captured incorrect for many pixels. The cause is mainly found in the PMD system noise, which impacts more at short integration intervals.

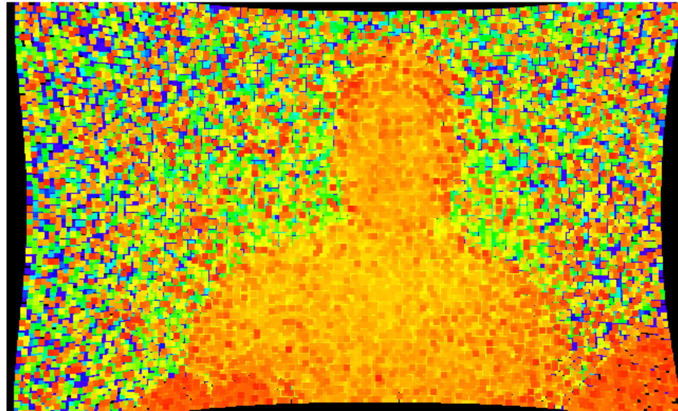

Figure 48: Picture quality with no software improvements using 100µs integration time

For the next picture, the integration time has been increased by a factor of 10 compared to the previous setting. Figure 49, shows the improved picture quality mainly caused by the averaging effect of the longer integration time.

Figure 49: Improved picture quality with 1ms integration time

The next study, shows the measurement range of the PMD device for an assumed black target (black wall) with an integration time of 1ms and a modulation frequency of 30MHz. The images where captured at several distances using colored distance representation as given below.

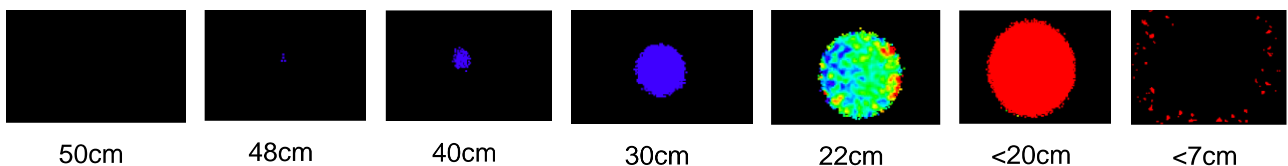

Figure 50: Reflected signal captured from a black target (black wall)

In Figure 50, the reflected light beam of the illumination source is shown at distances from 50cm to below 7cm. It can be seen, that the maximum measurement range with this device, assuming a black target and office light conditions is approximately 48cm. This is mainly restricted by the optical output power of the LEDs. Additionally, even with a wide viewing angle of 82°x66° the reflected light beam begins to miss the detector at close

distances. Hence to less photons are coming back and can be detected. It can be derived, that the distance between the light source and the emitter in the package plays an important role at short distances.

Next, an investigation on the maximum range was done showing the results below:

Maximum range	Target reflectivity	Ambient light conditions
~90cm	White reflective cardboard	60lux
~80cm	Black soft cover	

Table 9: Maximum range achieved by the PMD CamBoard pico, integration time was 1ms and the modulation frequency 30MHz.

The next analysis was made under high ambient light conditions. In Figure 51 below, the representation of the scene captured with the PMD device in 30cm distance is shown. As can be seen, thanks to high immunity against ambient light, the in-pixel based sensor can be still gather distance information above 1klux. However, a higher noise floor occurred at the scene borders and an additional circular noise (marked in the Figure) moved depending on the irradiation angle over the scene.

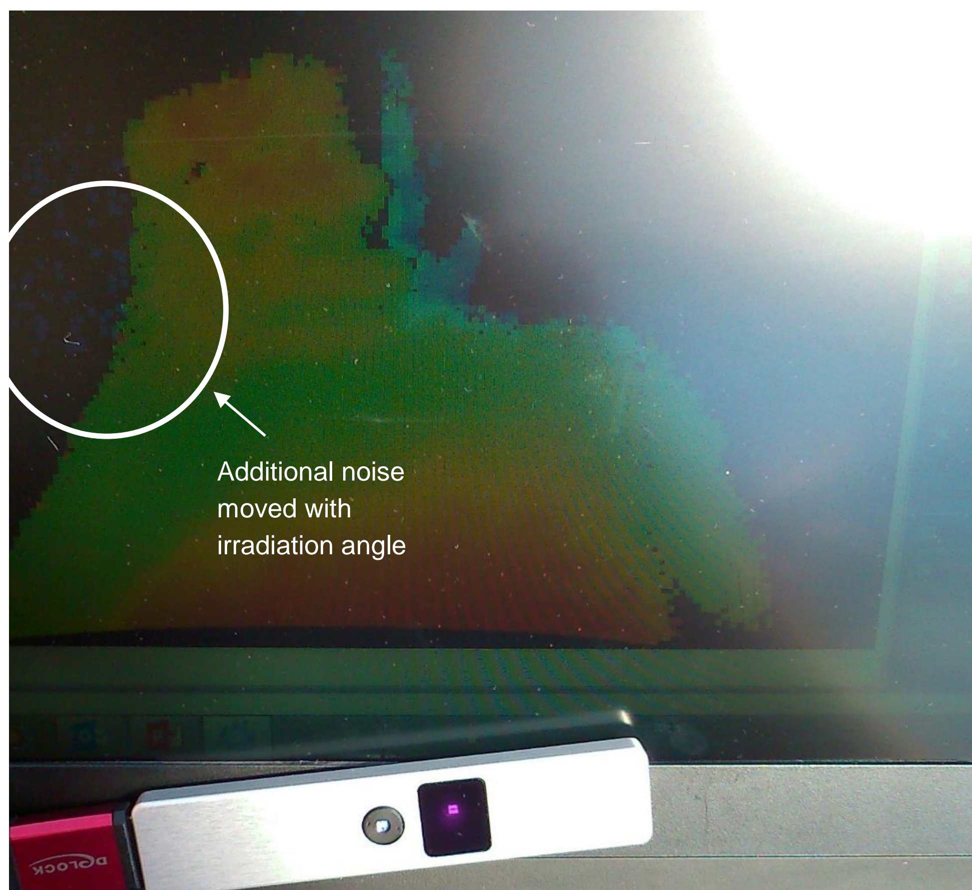

Figure 51: Captured image under high ambient light >1klux, 1ms integration time, at a modulation frequency of 30MHz and distance to the scene of 30cm

Finally, a very serious survey for all TOF devices will be presented. A multiple object, multiple reflection scene respectively a person behind window glass was tried to be captured by the PMD device. The measurement settings were left the same to the previous investigations. The distance to the object behind the window was approximately 40cm. The captured image for this test is given in Figure 52. It was taken with a digital camera through the window glass. The picture shows the LightVis screen on the laptop and the PMD CamBoard pico mounted below. As can be seen there is no colored distance information of the object (person) present, except some saturated pixels, which have been marked in the Figure below.

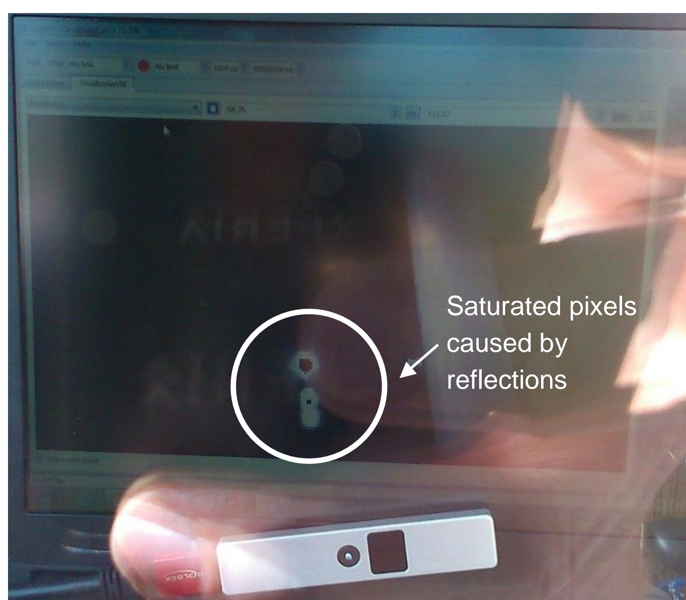

Figure 52: Test behind window glass, distance to the object 40cm

To summarize, the PMD CamBoard pico shows good performance in 3D imaging, even under high ambient light. The resolution is high enough to detect even complex gestures. The operation range varies depending on the object reflectivity and the lightning conditions from 20cm to 70cm. A drawback is the power consumption of the device with up to 2W with not negligible heating. As a proposal, a future device should use a VCSEL light source with a diffusor on top instead of several power consuming LEDs. It is really pity for such an overall good device to limit the fields of application and make it definitely not usable for battery-powered devices.

2.4 Others

In this chapter, a brief review on the Creative SENZ 3D by SoftKinetic, tested by the marketing group of ams will be given. Following this, a performance comparison table of today's commercial available TOF cameras will be presented.

The Creative SENZ 3D have been designed for consumer electronics mainly PC and Smart TVs, for gesture recognition and gaming applications. The camera is based on the I-TOF phase shift measurement principle as described in chapter 1.6.2. The SENZ 3D has 320×240 depth map sensing pixels and additional 0.9Mpixel for RGB imaging. A distance measurement accuracy of the camera is not known, but preliminary tests performed by the group have shown a distance measurement accuracy comparable to the PMD CamBoard pico. Furthermore, the camera provides a very wide FOV of 74°, which is a requirement in gaming applications.

A teardown of the SENZ 3D can be seen in Figure 53, it shows two printed circuit boards (PCB) containing the illumination source on the upper board and on the PCB below the camera as well as the detector module.

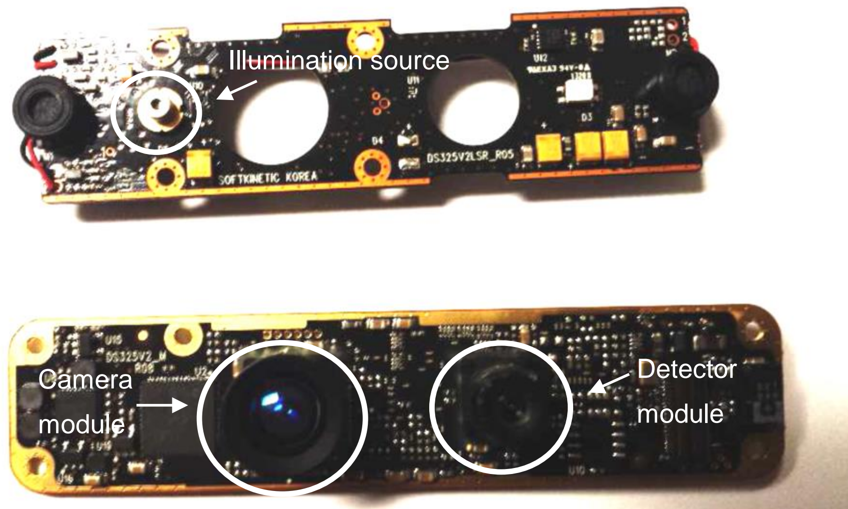

Figure 53: Teardown pictures of the Creative Senz 3D camera

A closer picture has been captured showing the illumination system. It shows in Figure 54 that the illumination source consists of an Edge-emitting LED c.f. [65].

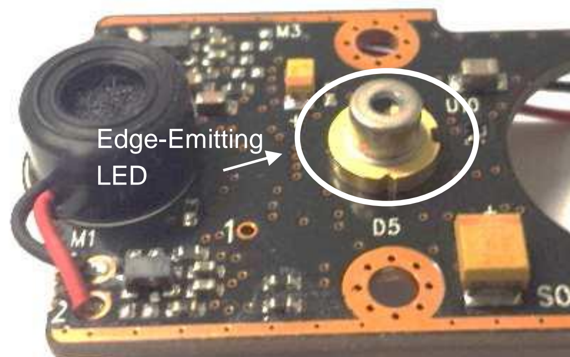

Figure 54: Illumination source of the Senz 3D consists of an edge-emitting LED

The results of some performance measurements performed by the test group will be given as follows. A maximum distance measurement test using an OPTEKA gray card as a target has shown better distance performance compared to the specifications in the datasheet. As can be seen in Figure 55, the gray card can be sensed at distance up to 142cm.

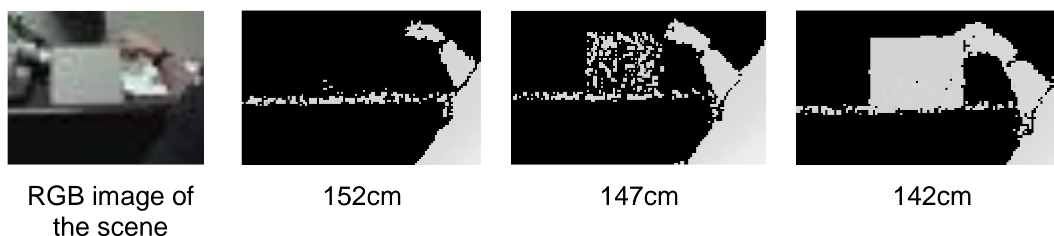

Figure 55: Maximum distance sensing a grey card

Additional measurements using a Macbeth Color Checker have shown that the camera suffers from sensing black colored targets. As can be seen in Figure 56, at 40cm distance to the table all colors have been senses on the map except the black one. In practical cases, problems might emerge when capturing e.g. black hairs with this device.

Figure 56: Using a Macbeth Color Checker for evaluation at 40cm

Additionally, application specific evaluations have been performed showing some unsolved problems. The group reported from false gesture detection using the shipped software. As can be seen in Figure 57, a gesture using forefinger and thumb was miss interpreted and led to a false gesture recognition.

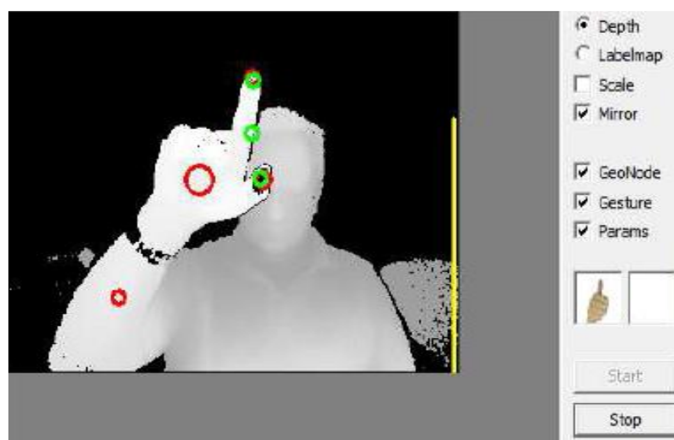

Figure 57: Wrong gesture detection using Creative Senz 3D

On the next page, key features about commercial available TOF cameras are summarized in order to show their performances among themselves. It is suggested that the column “measurement accuracy/repeatability” in Table 10 contains heterogeneous information since the camera manufacturers adopt different terms and conditions for this information [66].

Manufacturer	ToF Camera Model	Working Principle	Max Sensor Resolution [Pixel × Pixel]	Max Range [m]	Focal Distance [m]	Max Frame rate [fps]	Signal wavelength [nm]	Default Modulation Frequency [MHz]	Measurement Accuracy /Repeatability (σ)
Canesta Inc.	XZ422	I-TOF	160 × 120	n.a.	n.a.	n.a.	n.a.	44	n.a.
Canesta Inc.	Cobra	n.a.	320 × 200	n.a.	n.a.	n.a.	n.a.	n.a.	millimetric
Fotonic	Fotonic B70	I-TOF	160 × 120	7.0	n.a.	75	808	44	±0.015 m at 3–7 m (accuracy) and ±0.030 m at 3–7 m (uncertainty)
Mesa Imaging AG	SR-3000	I-TOF	176 × 144	7.5	0.008	25	850	20	n.a.
Mesa Imaging AG	SR-4000	I-TOF	176 × 144	5 or 10	0.010	54	850	30 or 15	±0.010 m or ±0.015 m
Optrima NV	OPTRICAM DS10K-A	I-TOF	120 × 90	10.0	0.0037	50	870	n.a.	noise level <0.03 m at 3.5 m
Panasonic	D-Imager (EKL3104)	I-TOF	160 × 120	9.0	n. a.	30	870	n.a.	±0.04 m and σ = 0.03 m (no ambient ill.) or σ = 0.14 m (ambient illum.)
PMDTechnologies GmbH	PMD19k	I-TOF	160 × 120	7.5	0.012	15	870	20	centimetric
PMDTechnologies GmbH	CamCube3.0	I-TOF	200 × 200	7.5	0.013	15	870	21	centimetric
PMDTechnologies GmbH	A2	I-TOF	64 × 16	9.4–150	n. a.	15	870	16–1	±0.10 m (distance < 40 m)
Stanley Electric Ltd.	P-300 TOFCam	I-TOF	128 × 128	15	n. a.	30	850	10	repeatability 1% of the distance (at 3 m)
Advanced Scientific Concepts Inc.	DRAGONEYE 3D FLASH LIDAR	D-TOF	128 × 128	1.500	0.017	10	1570	n. a.	±0.10 m and 3σ= ±0.15 m
Advanced Scientific Concepts Inc.	TIGEREYE 3D FLASH LIDAR	D-TOF	128 × 128	60–1.100	n. a.	n. a.	1570	n. a.	±0.04 m at 60 m
Advanced Scientific Concepts Inc.	PORTABLE 3D FLASH LIDAR	D-TOF	128 × 128	70–1.100	0.017–0.500	15	1570	n. a.	n. a.
SoftKinetic	DS311	D-TOF	160 × 120 + RGB 640 × 480	4.5	n. a.	60	infrared	n. a.	depth resolution <0.03 m at 3 m
3DV Systems	ZCamII	D-TOF (Shutter)	320 × 240 + RGB	10.0	n. a.	n. a.	n. a.	n. a.	n. a.
3DV Systems	Zcam	D-TOF (Shutter)	320 × 240 + RGB 1.3 Mpixel	2.5	n. a.	60	n. a.	n. a.	±0.02 m
SoftKinetic (Creative)	SENZ3D VF0780	I-TOF	320x240 + RGB +0.9Mpixel	0.15-1	n.a.	30	n.a.	n.a.	n.a.

Table 10: Performance comparison table for commercial available TOF cameras [66], modified

3 Concept Requirements

The targeted applications for a proposed 3D TOF camera for ams are gesture detection, proximity sensing and autofocus assistance in consumer electronics. Therefore, a camera must have an appropriate assessed array of approximately 50x50-pixels. The device must have low product-specific costs in order to be early competitive on the market. An important factor is the power consumption, it must not significantly impact the cell phones battery life. It should be of small form factor, hence a package should be a single, small package similar to the ams proximity sensor product. The thickness of the module has to be below 5mm. The light emitter and detector and all related electronics should be taken all together in a single modular package. Regarding the complexity of such a device, most signal processing should be performed on-chip and an I²C interface should be used for data acquisition and further processing. Such a final product must have low EMI. Operation in high ambient light is intended. However, the best technology should be chosen, showing the greatest potential for 3D imaging as well as low cost proximity and autofocus applications. Finally, such a device technology should be capable for further fields of applications like LIDAR, PET and Fluoroscopy.
Some application specific requirements have been predefined which should be taken into account for a proposed system. They are given as follows:

Proximity sensing:

- 30º Field of view (FOV)
- Single detector (1D ranging)

Autofocus assistance:

- Multi-zone sensor
- Multi-zone emitter
- Window detection (histogram interpretation)

3.1 Technology Decision

In the chapters before we have intensively reviewed in-pixel based as well as SPAD based TOF sensors. It was shown that each one of these technologies has his pros and cons and there is no clearly embodiment suitable for all the potential applications. To summarize the benefit of in-pixel based sensors is their high background light suppression capability. Furthermore, they are already integrated in commercial available cameras showing good 3D imaging quality at high frame rates. However, there are several aspects need to be improved. Primarily, the high power consumption. On the other hand, SPAD based sensors have shown low power consumption making them perfectly suitable for battery powered devices. Additionally, several research groups have demonstrated their performance independently. Thanks to their picoseconds resolution, they are best suitable for a wide range of fields of application from automotive over consumer electronics to health care.
In order to come to a decision and in consequence to a system proposal our TOF group has rated in teamwork both technologies, an in-pixel based system based on CAPD compared to a SPAD based system.
Therefore, an evaluation profile based on a scorecard was used. The summarized decision factors were organized by their importance. Ratings were carried out using numbers from one to 10 whereby a one indicated low success, poor, high cost and long time. On the other hand, a 10 implied high success, low cost, short time. The evaluation for each factor quoted in a separate column was obtained by multiplying the rating figure with

their importance factor. Finally, all these columns were added up to a final result. The decision profile including the final rating is given below.

		SPAD		CAPD	
Factor	**Importance**	**Rating From 0 (low) to 10 (high)**	**Rating x importance**	**Rating From 0 (low) to 10 (high)**	**Rating x importance**
Process Node	10	4	40	8	80
Performance Risk	10	10	100	7	70
Price in 2018 < 0.50	10	2	20	2	20
Optical Filter	10	2	20	10	100
Cross license support	10	10	100	2	20
Eliminate Optical Reference Path	10	5	50	2	20
Time to Market (Best Case)	8	8	64	10	80
Architecture Risk (Time to Market Worst Case)	8	5	40	6	48
Autofocus - 9 zones	8	10	80	10	80
Ambient Light Handling	8	4	32	6	48
Power Consumption	8	8	64	5	40
Multiobject	5	10	50	0	0
Zero Distance Detection	5	10	50	3	15
Low Signal	5	10	50	6	30
Patent	5	5	25	9	45
Experience	5	5	25	2	10
Digital Complexity	5	1	5	7	35
Customer Software Complexity	5	5	25	7	35
		Total SPAD	**840**	**Total CAPD**	**776**

Table 11: Decision profile with total ratings for SPAD and CAPD

Because of this ranking, it is assumed that a SPAD technology will be the best choice for ams AG to build a TOF chip that perfectly serves our targeted applications. In the following chapter, a proposal for a deep submicron TSMC CMOS implementation of a SPAD based TOF sensor is carried out. This advances process node reduces the required space especially when thinking of a histogramming approach. Further small process nodes lead to less power consumption and allow better TDC resolution hence a higher depth resolution. Thanks to the high integration we assume that the fill factor will also increase. However, we have to deal with a performance risk since every design in deep submicron technology presents challenges in terms of analog and digital circuit design and performance loss due to process variations and other related issues.

4 SPAD based TOF Camera System

In this chapter, a Time-of-Flight system based on SPAD will be worked out. To begin with, a rudimentary block diagram will be given brushing up the knowledge on TOF followed by a partitioning of the system. At this point, each block will be described in detail as well as feasible architectures. Then, a subchapter will be given showing the power consumption of the blocks followed by a physical dimension estimation of the system. Then a SPAD array concept will be introduced. Finally, we will estimate the performance of the system.

4.1 Block Diagram of a SPAD TOF System

A block diagram of the SPAD based 3D imaging system is given in Figure 58. It consists of a VCSEL laser light source, emitting short optical pulses (~200ps), a matrix of pixels being capable to detect single photons along with their TOF at picoseconds accuracy, a micro lens aperture to increase fill factor, high attenuate optical filter stacked onto the photodetector to cancel ambient light, D-TOF measurement method and a full digital 3D image reconstruction based on histogramming.

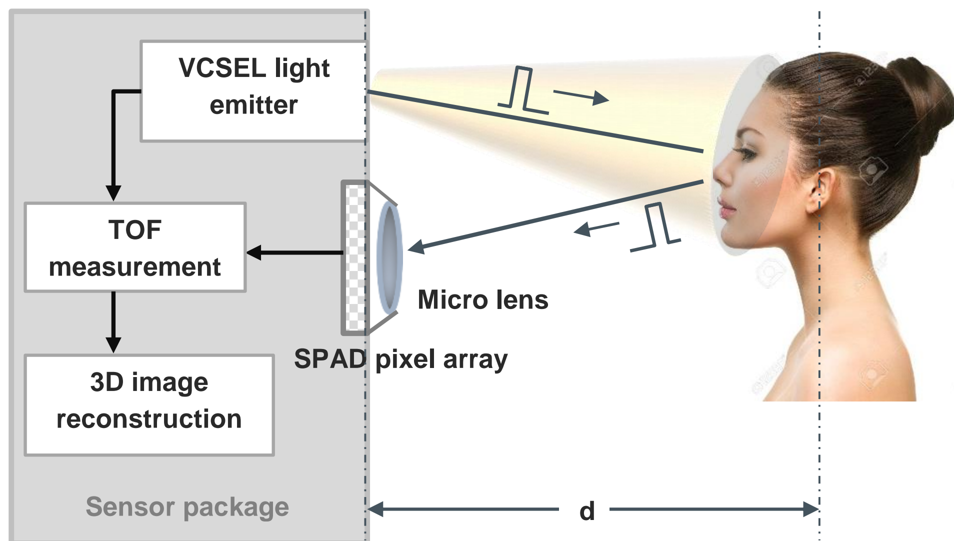

Figure 58: SPAD based TOF sensor

4.2 Partitioning for a SPAD based System

To understand the working principle for a SPAD based TOF system for mobile phone applications it is necessary to perform partitioning. In Figure 59, the TOF system is divided into the detection, readout and processing system. The detection system, or alternatively called pixel, consists of the SPAD with their front-end quenching circuit and the TDC converter. An exception is a macro pixel, which consist of several SPADs including their quenching circuits sharing one TDC. This option has the effect of increasing the fill factor and it will be described in a later chapter. In addition, the illumination system will be given in the next subchapter. However, it can be regarded as a separate building block, whereby the incident light on the SPADs results therefrom and indirectly the start pulse of the TDC. The Time to Digital converter measures the time between the start-pulse and stop-pulse accurately. The TDC is driven by an external or internal clock and is addressed by a global controller. The output of the TDC is readout either event driven or sequentially. The readout circuit passes the series of time

stamps to a digital processing circuit, which stores the data in a memory and performs with the use of a core histogramming or directly provides the data to an output.

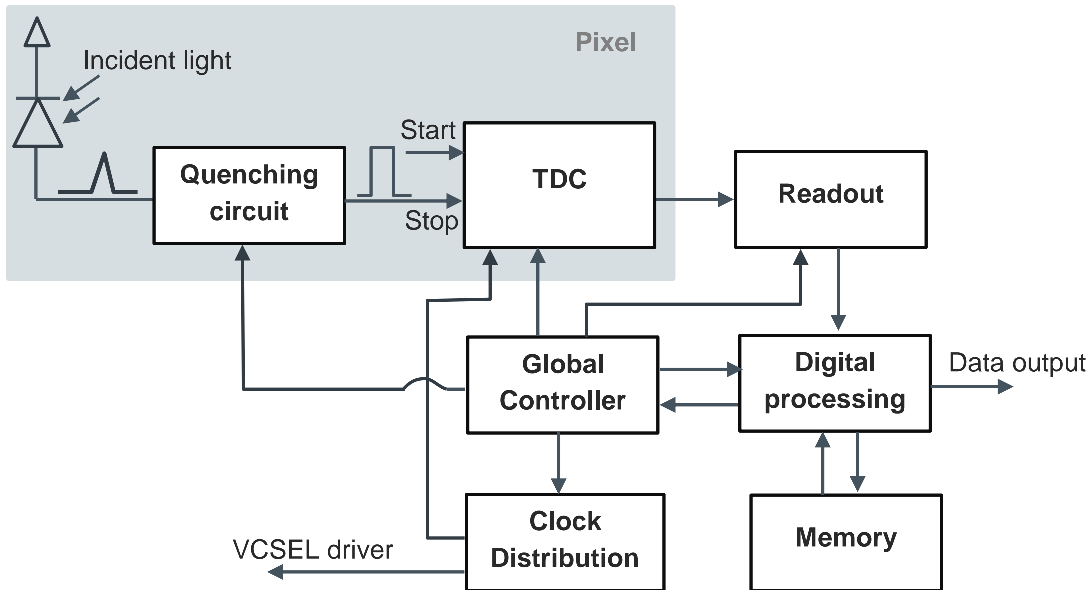

Figure 59: Partitioning of the TOF system showing detection, readout and processing blocks

4.2.1 Illumination System

The illumination system consists of a VCSEL light source driven by a driver, which is in turn clocked by an oscillator or a phased locked loop (PLL). At the optical side of the VCSEL, one path leads towards the scene of interest and a second path crotch some light and leads it straight towards a reference SPAD or fast photodiode (c.f. Figure 39). This is necessary in order to have an optical reference start pulse to trigger on. Due to temperature variations in the silicon an electrical start pulse is too inaccurate for the TDC. In order to achieve high accuracy the driver provides a modulation frequency above 100MHz. In the design of such a PLL or oscillator, the emission causing electromagnetic interferences become very important. Because of that, a separate chapter will address this issue.

There are two ways positioning the driver, embedded in a module with the VCSEL light source or standalone. Further, the VCSEL can be placed on the sensor die or beside.

In Figure 60 below, the illumination system is sketched.

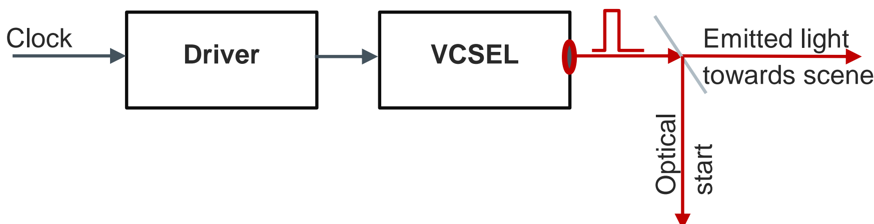

Figure 60: VCSEL based illumination system

The system goals for a VCSEL based illumination system are:

- maximize the optical output
- minimize the optical pulse with
- stay in laser safety class and reduce power consumption

Hence, a VCSEL driver has to provide short pulses, high current and low duty cycle. Several VCSEL driver concepts have been presented in literature mainly for optical communications in glass-fiber cable. Because both transmitter and receiver architectures are characterized in the papers the interesting performances for our VCSEL driver system have to be acquired carefully. However, a figure of merit (FOM) is presented herein based on a proposal in [67]. A high FOM indicates a desirable architecture in terms of performance and costs. A performance comparison table is given in Table 12.

Generally, a VCSEL driver can be distinguished by their wiring of the VCSEL light source. A common-cathode type controls the current flow from the positive power supply into the anode of the VCSEL. In the following Figure 61 a common-cathode structure is given:

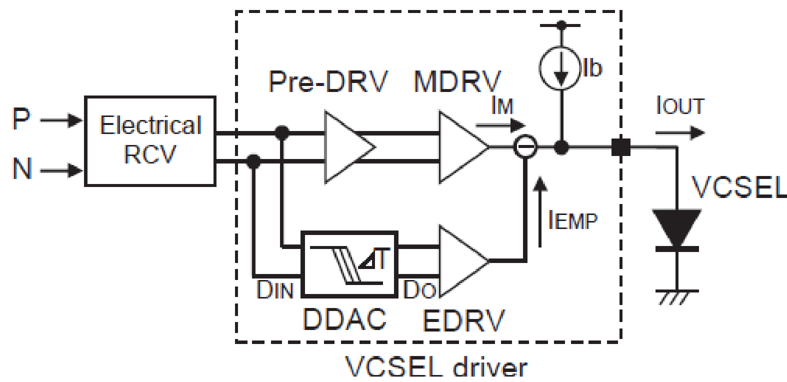

Figure 61: Common-cathode VCSEL driver in 65nm CMOS [68]

The VCSEL driver was introduced in [68] implemented in a 65nm CMOS process providing 25Gbps for each of the four channels. Each channel consumes a large area of 0.32mm². The power consumption is 74.4mW/channel at 25Gbps, which is relatively high, and leads to the lowest FOM of 1.05 presented here.

Another common-cathode based laser diode (LD) driver providing 25Gbps with less space consumption is presented in [69]. The driver was thought for optical interconnects, and was fabricated in 65nm CMOS technology. A schematic of this driver is given in Figure 62, it shows that the main driver stage is based on a mutually coupled inductor circuit to adjust the inductive peaking and improve eye patterns under various packaging conditions. Additionally a pre driver is used to provide a gain of 20dB, whereas it uses a CMOS active feedback circuit to achieve a wide bandwidth and high gain in relation to the small size and power consumption. The laser diode driver provides 26mA average current to the diode while consuming 6.2mW/Gbps. In case of a VCSEL light source, less power consumption of 2.6mW/Gbps at an average current of 10mA is proposed for this system, which leads to an improved FOM of 34.9.

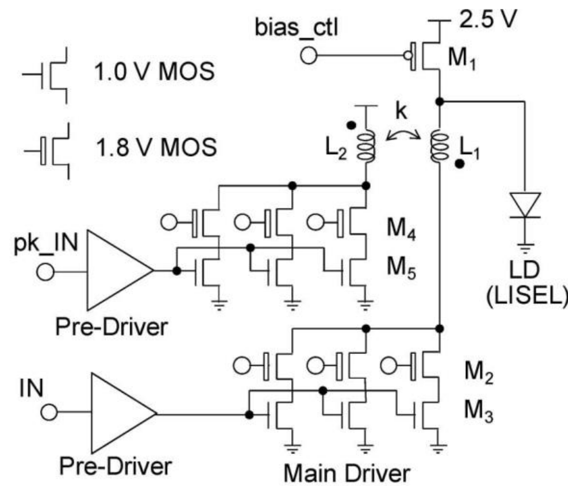

Figure 62: Structure of the laser diode driver [69]

Next, a common-anode VCSEL driver in 90nm CMOS is presented in [70]. The sketch of the driver architecture is given in Figure 63. The VCSEL driver is driven by a multiphase 3.2GHz PLL and has a power consumption of 48mW at an optical data rate of 16Gbps. The average current across the 850nm VCSEL was 6.2mA. Approximately 2mW (3.1dBm) optical transmit power is stated for this concept. The VCSEL driver area is 0.017mm². Because of the relatively large power consumption, the FOM is worse to the previous system.

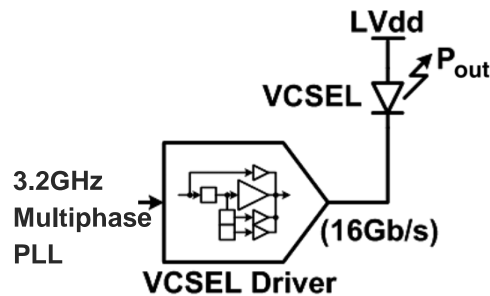

Figure 63: Common anode VCSEL driver [70]

The system with the highest FOM is presented in [71]. It is based on a common-anode structure and has been integrated in an 80nm CMOS process. The active area of this implementation was 0.005mm². A schematic of the transmitter is given in Figure 64, showing a combination of a pre-driver and main driver stage. The main driver is a combination of a common source (CS) and a source follower (SF) amplifier topology, has advantages in terms of voltage gain, power consumption, and reduced VCSEL timing jitter. The power consumption was only 16.8mW including the VCSEL, providing 1.78mW optical launch power.

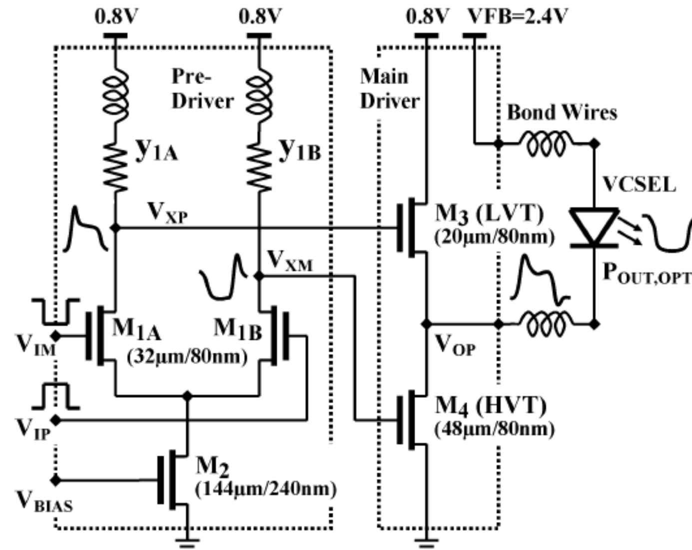

Figure 64: Schematic of the VCSEL driver stage [71]

Finally, a very compact VCSEL driver is reported in [67], with only 0.003mm² active area in 80nm CMOS technology. The triple-well common-cathode architecture is much more reliable compared to the common-cathode solutions in [68] and [69], based on stacked transistors. The driver provides a data rate of 17Gbps at a maximum average optical power of 1.7mW (2.5dBm). The total power consumption reported for this system was 60mW.

An overall performance comparison table of the different VCSEL driver architectures is given below:

Parameter	Unit	[68]	[69]	[70]	[71]	[72]	[67]
Year		2014	2011	2008	2005	2012	2015
Type	-	Common-cathode, stacked transistors	Common-cathode, stacked transistors	Common-anode	Common-anode	Common-anode	Common-cathode, triple-well
Technology	nm	65 CMOS	65 CMOS	90 CMOS	80 CMOS	90 CMOS	80 CMOS
Data rate optical	Gbps	25	25	16	10	25	17
Power consumption transmitter incl. VCSEL	mW	74.4@3.3V	65@2.5	48@2.8V	16.8 @2.4V	36.2 @1.2V	60@2.7V
Energy efficiency	mW/Gbps	2.9	2.6	3	1,68	1.4	3.5
Active area per channel	mm²	0.32	0.011	0.017	0.005	0.014	0.003
Optical power	mW	-	0.17	2	1.78	0.73	1.78
FOM	$\frac{Gbps}{mW \cdot mm^2}$	1.05	34.9	19.6	119	49.3	94.4

Table 12: Performance comparison table of published VCSEL driver

A VCSEL light source used in TOF has several benefits, which will be briefly described. A good power conversion efficiency (PCE) of >40% at 808nm and >50% at 976nm is reported for VCSEL in [73]. Where PCE is given as the ratio of the optical power divided by the electrical power at which the VCSEL is driven. Although the narrow spectral width is an advantage compared to LEDs as shown in Figure 65 below:

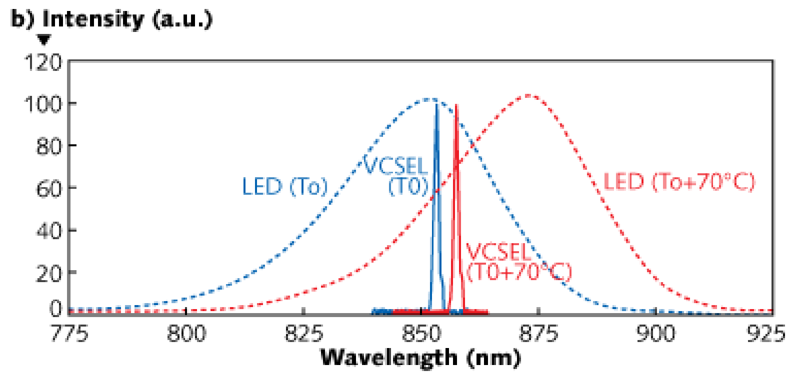

Figure 65: Spectral width of a VCSEL compared to a LED, showing the temperature variation [74]

Thanks to its narrow spectral width of approximately 1nm at FWHM, filters can be adapted on the photodetector in order to reduce the noise associated with background radiation. Additionally a VCSEL combines best spectral properties with high reliability, an almost speckle free illumination source, narrow beam divergence, and significant packaging flexibility. An additional performance comparison table is given below:

Parameter	High-power IR LED	High-power IR VCSEL array	Edge-emitting laser
Low cost and manufacturability	++	+	-
Ease of packaging	+	+	-
Output power	-	+	++
Reliability	+	+	neutral
Modulation speed	-	+	+
Emission beam and optics integration	-	+	-
Spectral properties	-	++	+
Speckle-free	+	+	-

Table 13: Performance comparison of VCSEL compared to LEDs and Edge-emitting laser [74]

Practically, it is possible to connect 2D arrays of VCSEL parallel to achieve a larger emission area and higher power. For example, a 0.25mm² VCSEL array can emit more than 1W of power in pulsed mode. About 3W is achievable in pulsed mode from a 0.45mm² array [75]. For gesture recognition application in consumer electronics 10mW to 3W are necessary whereby for 3D imaging up to 10W optical power are required [74].

4.2.1.1 Average and Peak Power

In this subchapter a short excursion to average and peak power of a pulsed VCSEL light source will be given. The relationship between average and peak power is described in [76], whereby the average power of a pulsed VCSEL is given by the equation:

$$P_{avg} = \frac{Pulse\ energy}{cycle\ period} = \text{Energy} \cdot \text{frequency} \tag{3.5}$$

It shows, that shorter pulse periods or higher pulse frequencies increase the average power. Another considerable figure of pulsed signals is how much power is delivered with each pulse. This is defined as peak power which is given by:

$$P_{peak} = \frac{Pulse\ energy}{Pulse\ width\ (FWHM)} \tag{3.6}$$

As can be seen for a given pulse energy, the peak power increases with a shorter pulse width. However, a shorter pulse width is desired in TOF with ranges from nanoseconds to picoseconds. The corresponding amount of energy released in such small time frames is ranging from few nanojoules to picojoules.
Usually the peak power of a train of pules signals is set to a fixed value, hence another factor have to be considered namely the signal duty cycle. It is defined as the ratio between the pulse width and the signal period. Furthermore, it applies that the duty cycle affects the average power proportional, as given below:

$$P_{avg} = P_{peak} \cdot \frac{pulse\ width}{period} = P_{peak} \cdot \text{duty cycle} \tag{3.7}$$

Therefore a decrease on duty cycle decreases the average power and vice versa.

4.2.2 Time to Digital Converter

Building a TDC in deep submicron CMOS, requires comprehensive knowledge of several architectures available including their performance parameters. Especially, because the TDC determines the achievable resolution of the TOF system. A buffer or gate delay limits the minimum time resolution achievable with a TDC.
In literature, it is differentiated between two TDC architectures, they are:

- Delay Line(DL) based
- Coarse-fine

An improved DL based structure is the Vernier Delay Line (VDL) given in the schematic below:

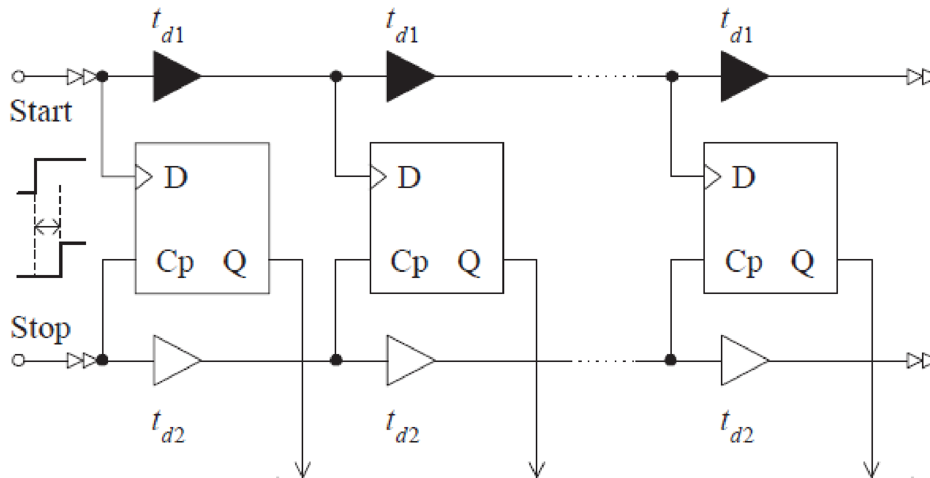

Figure 66: Basic Vernier delay line [77]

A Vernier TDC consists of two delay lines, one for the Start and one for the Stop, composed of buffers and a flip-flop at each corresponding pair of connections. It is assumed that the delay t_{d1} is slightly larger than the delay t_{d2} of the second delay line. A time interval measurement is triggered on the propagation of the Start signal in the first delay line. The Stop signal from the SPAD arrives later in time but it experiences smaller delays in the delay line and chases the Start signal until it is in phase. This method enables resolution below the gate delay time. For more details, see [78].
An optimized VDL structure was presented in 2010 and built in 65nm TSMC CMOS process in [79]. A 7-bit TDC was designed achieving a time resolution of 4.8ps and a power consumption of 1.65mW for a conversion rate of 50Msps requiring 0.02mm². However, the VDL structure suffers from long delay lines making them susceptible for process variation leading to resolution loss. Furthermore, they are undesirable for low-cost applications, because of their too long delay lines. Additionally, it can be concluded that linear delay line structures are suitable only for short dynamic range [78].
Another TDC architecture commonly used in SPAD based TOF sensors is called Coarse-fine TDC. The benefit of this is a higher dynamic range and resolution. Its principle is based on two TDC blocks, a coarse TDC measures the time interval in coarse time steps, achieved through the use of counters, whereas a fine TDC is built of a ring oscillator or VDL. The fine converter quantizes the time residue between a reference clock and the start signal in smaller time steps [80]. An elementary block diagram for this architecture is given in Figure 67.

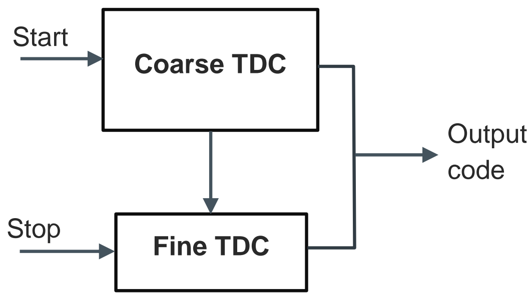

Figure 67: Coarse-fine TDC block diagram

Next, two scalable coarse-fine architectures will be presented and their strength and weaknesses will be described. The first structure is called TDC-EC, because of its external clock distribution [3]. It was introduced in [81], and consist of a 32x32-pixel TDC array fabricated in 130nm CMOS process. The proposed system works in reverse start-stop mode, which means that the converters are activated when the SPADs are fired and stopped by an external PLL synchronous to the reference pulse of the illumination source. The benefit of this reverse mode is that the TDC does not consume power if no photon was detected. A constraint is, that this configuration works only with a very stable pulsed laser source, because the STOP signal is taken from the laser's synchronization signal for the subsequent laser pulse [81]. A block diagram of this architecture is given in Figure 68, below.

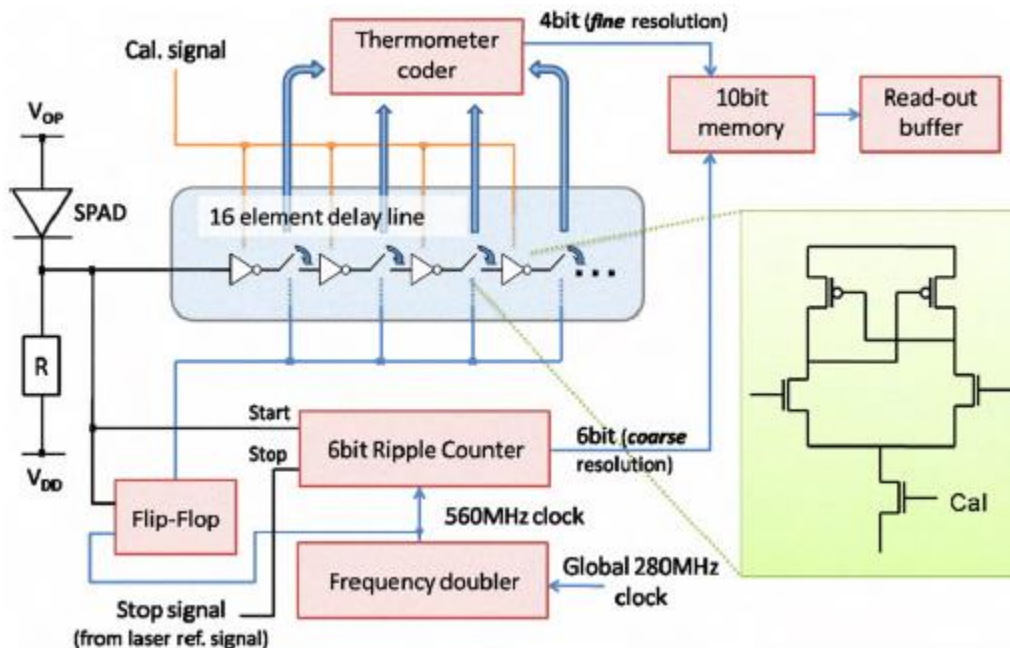

Figure 68: external clock TDC with coarse-fine converters [81]

The operation principle is shown Figure 69 and will be described as follows. Upon a photon is detected the front end circuit of the detector SPAD array generates a digital start pulse for the TDC which is send through the 16 element delay line of the fine TDC. On the first clock edge after the start pulse the propagation through the fine converter is stopped and the time-counts are converted through a thermometer coder into a 4-bit binary number.

At this point, the coarse TDC counts until the stop signal arrives. The stop pulse is the subsequent pulse from the reference signal synchronous to the PLL clock. The proposed course TDC has a resolution of only 1.78ns, but with the additional fine TDC, an increased measured time resolution of 119ps for this system is stated.

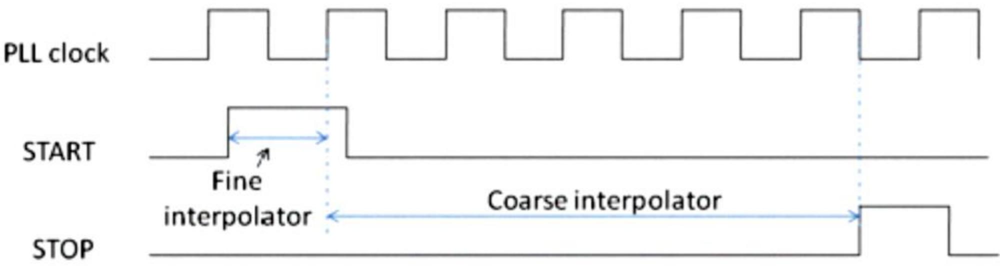

Figure 69: coarse-fine principle with reverse start-stop configuration [81]

After the acquisition time, the 10-bit code, which is equal to one frame, is stored in a memory placed inside the pixel. A rolling-shutter type readout is used to read then 500kframes/sec per pixel out of the chip. Even if no photon was detected, a specific code is read out.

Because the TDC is event driven, the power consumption will be lower for low illumination levels and increases under high ambient light. However, as can be seen in Figure 70, the power consumption is dominated by the PLL and clock distribution if only some pixel are enabled. Above 100pixel, the power consumption increases exponentially with the pixel activity.

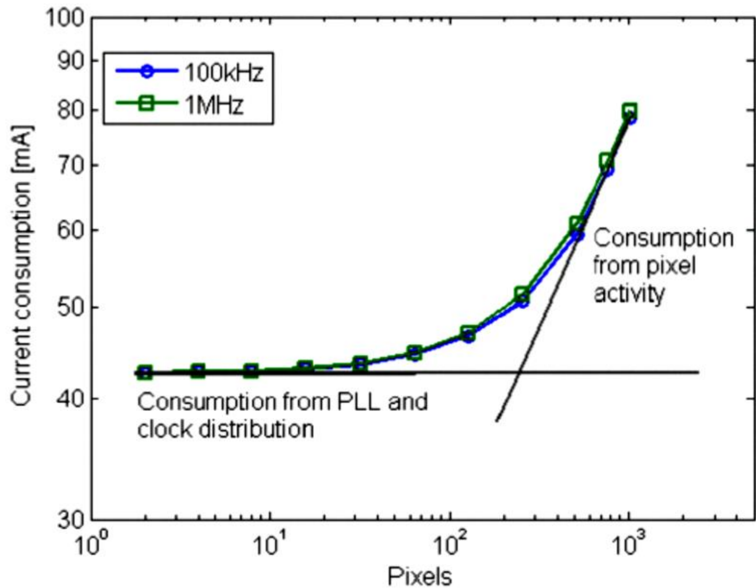

Figure 70: Power consumption as a function of the enabled pixel [81]

An internal clock TDC with coarse-fine architecture was introduces in [82], fabricated in a ST Microelectronics 130nm, 4 metal CMOS Imaging process. Thereby a coarse converter consist of a gigahertz gated ring oscillator within each pixel, incrementing a ripple counter on every ring period. The fine interpolation is obtained by decoding the 'frozen' dynamic states of the internal inverter chain of the ring. A logic block is used to generate ring oscillator differential control signals. A block diagram of the TDC is given in Figure 71.

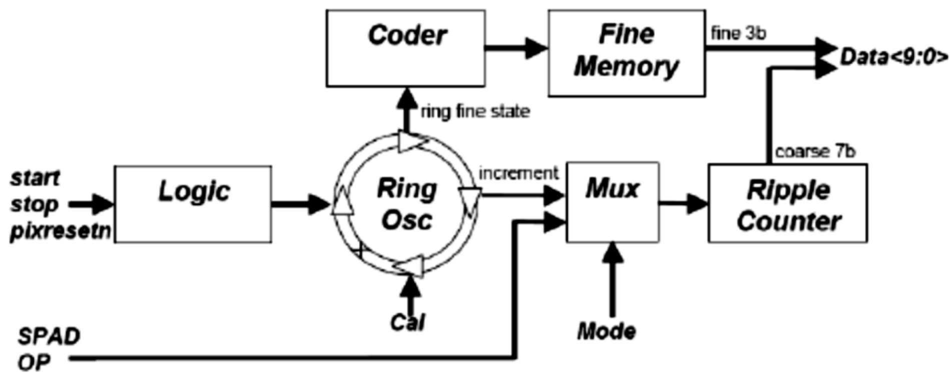

Figure 71: Block diagram of the proposed ring oscillator TDC [82]

As can be seen in Figure 72, the TDC operates in reversed start-stop mode whereby for data acquisition a minimum time resolution of 50ps is achieved. Because of the event driven mechanism the ring oscillator is only started when a photon was detected. During this on time the TDC consumes approximately 275µA peak current.

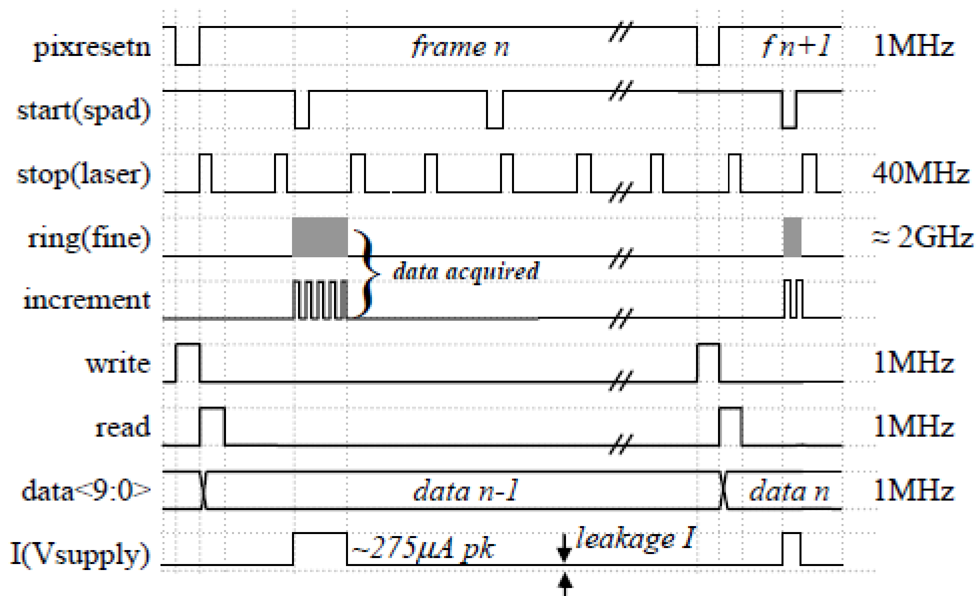

Figure 72: Operation principle in TCSPC mode [82]

The power consumption of this architecture is highly photon-flux dependent and limits the applications as well as the scaling of the array to larger resolution formats (c.f. [83]). As can be seen in Figure 73 the power consumption increases linear with the number of pixels that have been activated by the photon arrival. The offset of approximately 22mW for the TDC array is given due to contribution of clock trees, readout, calibration block and I²C ancillary cells [82].

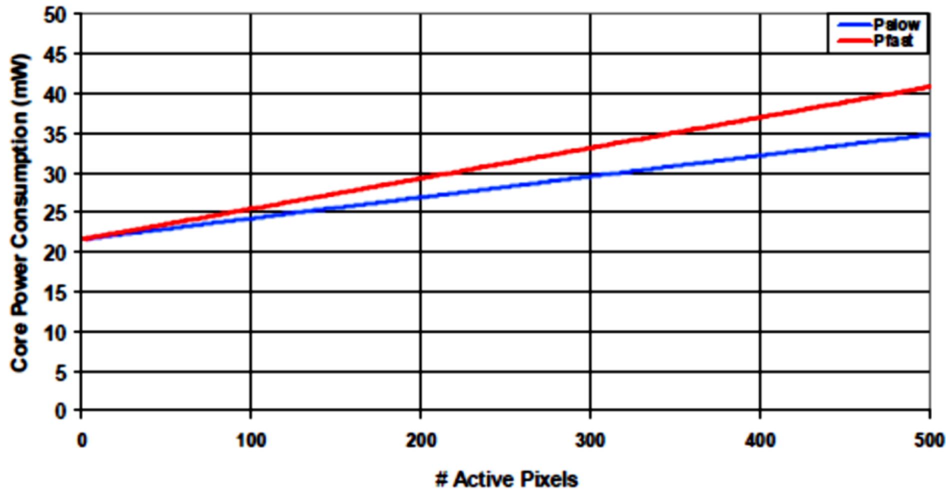

Figure 73: Power consumption of the 32x32-pixel TDC array as a function of the active pixels [82]

A TDC-IC structure with ring oscillator in a 64x64-pixel 3D imaging sensor in 0.18µm CMOS introduced in [84]. The targeted applications fluorescence lifetime imaging (FLIM) but also 3-D imaging for object reconstruction. A block diagram of the differential controlled coarse-fine ring oscillator is given in Figure 74. The single TDC area is 1740µm², which is smaller than the previous introduces TDCs. A block diagram of the TDC is given below:

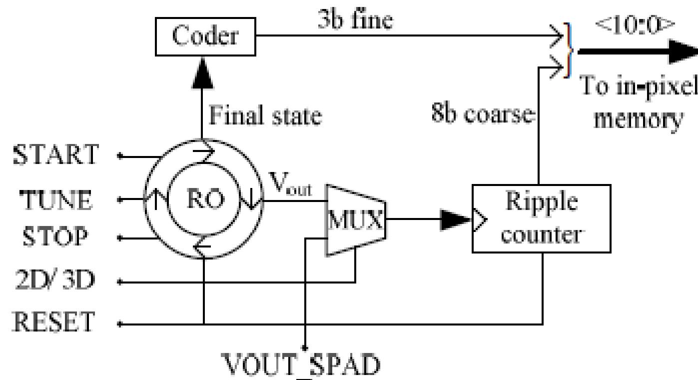

Figure 74: Block diagram of the 11-bit ring oscillator based TDC [84]

The main contribution to power consumption at the pixel level is the operation of the voltage controlled ring oscillator when running at maximum frequency. The average power consumption at full range and 5kfps is 2.7µW per TDC, which is an improvement of factor three compared to the earlier approach in [82]. The TDC achieves a best time resolution of 145ps, which is at the limits of human face reconstruction (c.f. [13]). Finally, the performance parameters for the described TDC approaches are summarized in Table 14.

Parameter	Unit	[81]	[82]	[84]
Year		2009	2009	2014
Type	-	TDC-EC	TDC-IC	TDC-IC
Technology	nm	130	130	180
Format	-	32x32	32x32	64x64
Pixel pitch	µm	50	50	64
Bit resolution	bits	10	10	11
Time-resolution (LSB)	ps	119	178/52	145
Uniformity	LSB	+/- 2	8	-
INL	LSB	+/- 1.2	+/- 0.4/1.4	1.7
DNL	LSB	+/- 0.4	+/- 0.5/2.4	+/- 1
Time jitter	ps @ FWHM	185	107/32	133
Power consumption	µW @ 500kframe/sec	94	28/38	9
Single TDC area	mm²	0.002	0.0022	0.0017
Chip TDC area	mm²	2.05	2.25	7.13

Table 14: Overall performance parameter of the introduced TDCs

4.2.3 Readout

A critical block in SPAD based TOF detectors is the readout system. The main issue is the dynamical photon counting process, generating immense data's which have to be processed. Compared to in-pixel based detectors where the photocurrent is integrated in the parasitic capacitance and the resulting voltage is available at the end of the integration process, SPAD based sensors need external controllers, counters thus larger active area. However, this increase in pixel area is not necessarily preferred because it exhibit larger jitter and noise and has an impact on costs [85] .

However, three basic readout mechanism for SPAD based detectors can be quoted:

- Parallel readout
- Event driven readout
- Sequential readout

In a fully parallel readout, every pixel on the array has a dedicated routing resource as shown in Figure 75 below.

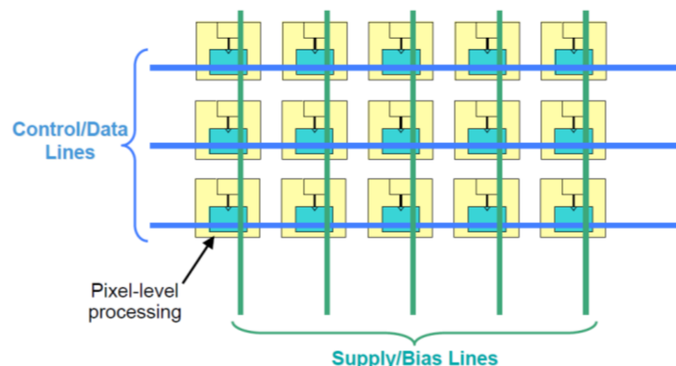

Figure 75: Fully parallel readout structure [86]

The benefits of full parallelism are that no photons are lost within the detection cycle and the frame acquisition and readout time is minimized. Drawbacks are the larger routing area and the readout bandwidth. Additionally noise issues from the substrate or supply must be considered in this architecture [86].

In an event driven readout [2], [87] a pixel is read only when a photon impinged on the SPAD. Through a signaling mechanism the pixel communicates the occurrence of the event to a controller (Figure 76). The benefit of this system is that it consumes low power as any pixel is read only when it has a new data from a photon event. A drawback of this readout mechanism is that it works well only with low photon count rates. Which perfectly fits for FLIM applications but not for 3D imaging under high ambient light. Furthermore, during a readout cycle the bus is blocked which leads to a large column dead time.

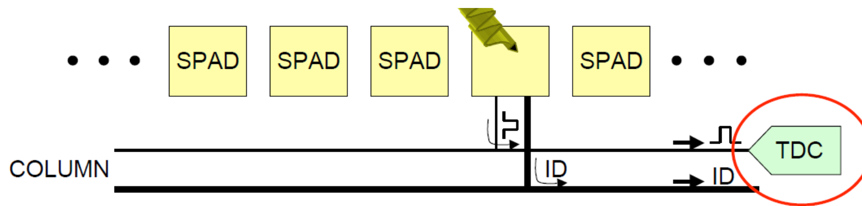

Figure 76: Schematic of an event-driven readout [87]

A commonly used readout mechanism in 3D-imaging applications is the sequential readout. The simplest sequential readout is the pixel-based readout where an M-to-1 digital multiplexer routes the output of a selected pixel directly to the global output for all M pixels in the array. This random access architecture provides high measuring accuracies per pixel, but it prevents simultaneous detection in all pixels [87]. Such an architecture was implemented in [13] and [88]. Another benefit of this architecture is that it allows selection and readout of a single pixel addressed by its coordinates and because of the simple readout scheme, it uses few silicon area and hence low costs. Drawbacks are the large readout time leading to a low frame rate a high loss of photon events thus making it highly inefficient [85]. A schematic of this approach is given as follows:

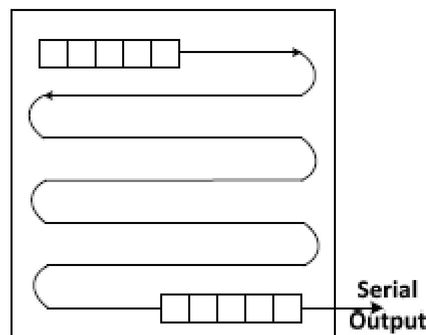

Figure 77: Pixel based random access readout [78]

While the pixel based readout has several drawbacks for 3D-imaging applications, a higher parallelism is needed which increases the readout speed. Such a column based rolling shutter readout is presented for a 32x32-pixel array in 65nm CMOS in [78]. In this approach a 5-bit row decoder and 32 serializers are used to select the pixel and convert its parallel data into a serial bit line. A block diagram of this even low cost architecture is given below.

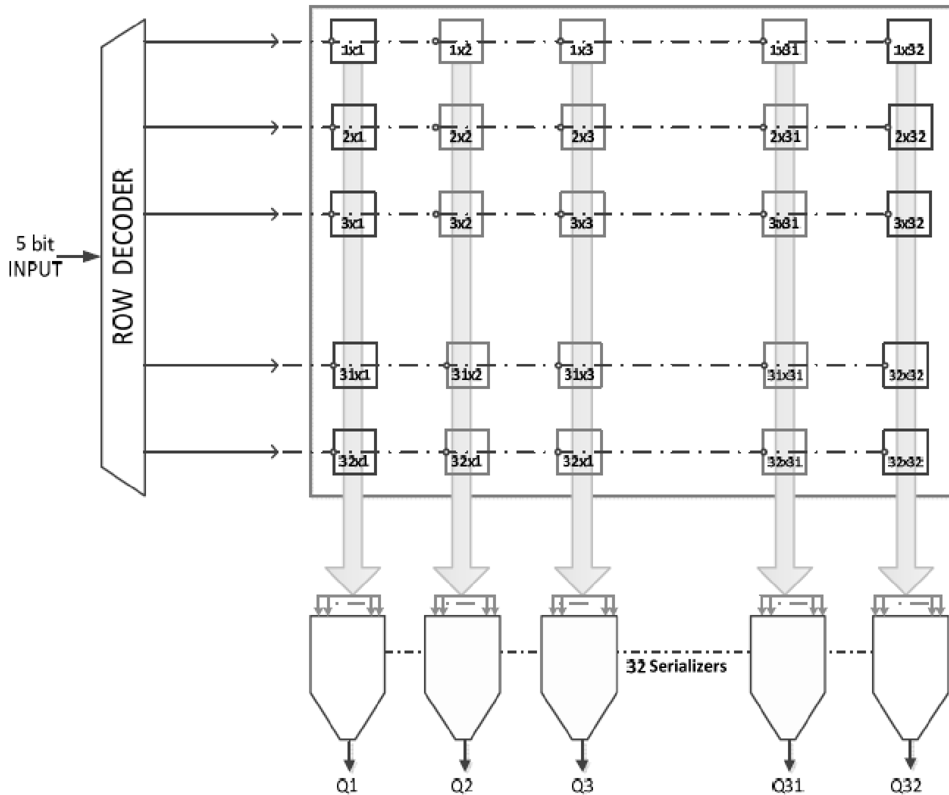

Figure 78: Block diagram of a column based rolling shutter system readout [78]

An approach, which can be suited to all readout schemes, is the ROI readout. In this particular readout case, a subset of lines and columns can be selected thus reducing the amount of data to be transferred and increasing the frame rate [85].

In Figure 79, the readout mechanism available for SPAD based detectors are stated, showing the trade-off between area consumption and readout time.

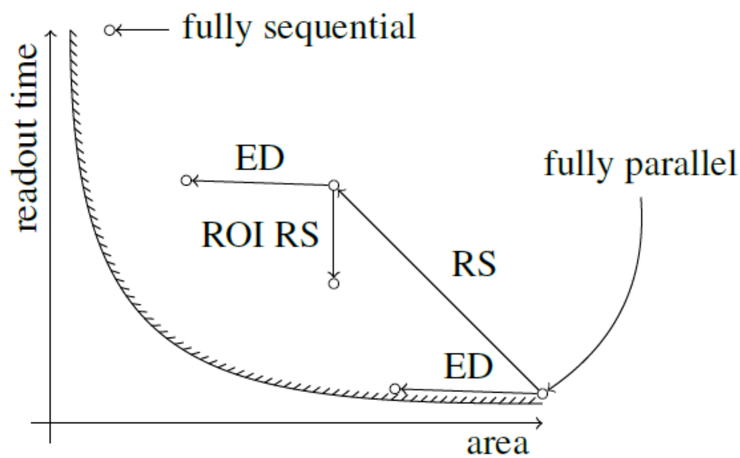

Figure 79: Readout schemes for SPAD based TOF sensors, whereby (ED) means event-driven and (RS) stands for rolling shutter mechanism [85]

4.3 Pixel Architecture Concept

Based on the collected knowledge in the previous chapters a pixel architecture concept has been worked out and a size and power estimation will be given for that.

As it was shown, a high parallelism has several advantages in TOF but suffers from a large layout area. This drawback can be overcome when some sharing is implemented. Therefore, a concept will be given using one TDC for several SPADs without information loss.

In Figure 80, a highly parallelized macro-pixel is introduced which contains 4 SPADs including quenching circuit whereby each SPAD is connected via a control/data line to the further processing circuit as well as to a supply respectively bias line. The latter can also be used to disable uncooperative SPADs, which commonly occurs due to defects in silicon. A 4-to 1 event driven multiplexer is used to serialize the data stream of the SPADs and hand it over to a TDC. This works as follows, a photon impinging on one of the SPAD surfaces leads to a digital pulse, which an event driven multiplexer senses and passes it to the TDC. In consequence, this first SPAD is blind as long as the dead-time, hence no pulse is expected. During this time, the multiplexer switches to the next SPAD passing the second pulse to the TDC and so on. Because of this sequential passing process, after pulsing effects can be decreased. A further idea would be an event ID, which is send to the TDC by every occurred avalanche. Such an ID can be used as an indicator for after pulsing (e.g. SPAD one has produced 10 events in a defined time slot compared to others with only one event) or ideally as an indicator for background light intensity.

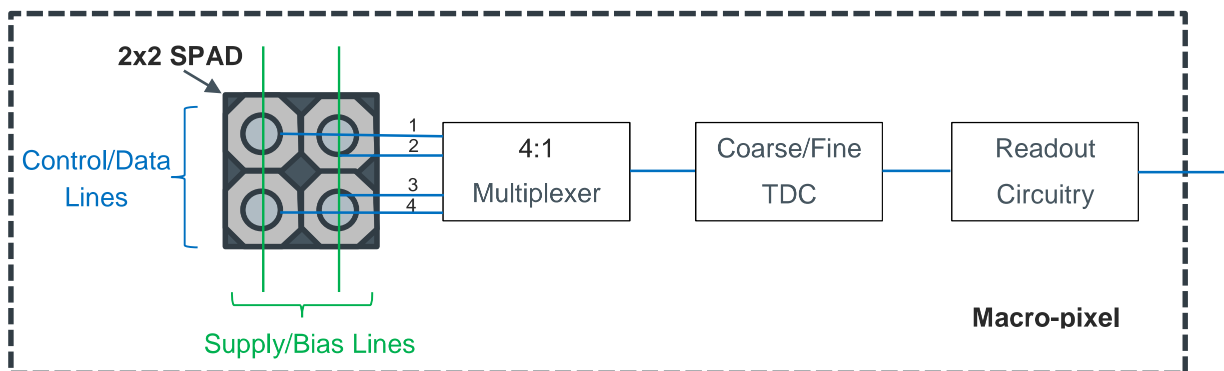

Figure 80: Concept for a macro pixel array with four SPADs using one TDC

The coarse-fine TDC proposed for this system is based on a ring oscillator architecture introduced in [84]. This converter seems to be the best choice in terms of low power and small area. Such a TDC structure consumes only 9µW at 500kframes/s at a space of 0.0017mm² in 0.18µm CMOS which might be reduced to 425µm² (factor 4) when using deep submicron TSMC CMOS process. The total macro-pixel active area measures about 576µm², using a 65nm approach presented in [78]. Additional digital circuitry like multiplexer and pixel readout may consume additional 50µm².

Summarizing, for a macro-pixel approach a total pixel area of 1051µm² is predicted in deep submicron TSMC CMOS process. The total power consumption for this macro-pixel is theoretically difficult to estimate, but can be predicted by simulations. However, it will be mainly determined by the TDC performance.

A fully-parallel concept with no TDC sharing is shown in Figure 81, whereby each pixel consists of a SPAD including quenching circuit, a dedicated coarse-fine TDC off the earlier model and a pixel readout. In this case, the detection of photons is only limited by their SPAD dead-time. A drawback for this pixel concept is that a SPAD defect leads to a complete pixel lost.
For this single pixel concept an active area of 144µm² using the same 65nm SPAD, a TDC space of 425µm² equally to the earlier model and additional digital circuitry of 30 µm² is predicted. Together, a total single pixel space consumption of approximately 600µm² is achieved. The power consumption is again determined by the TDC performance.

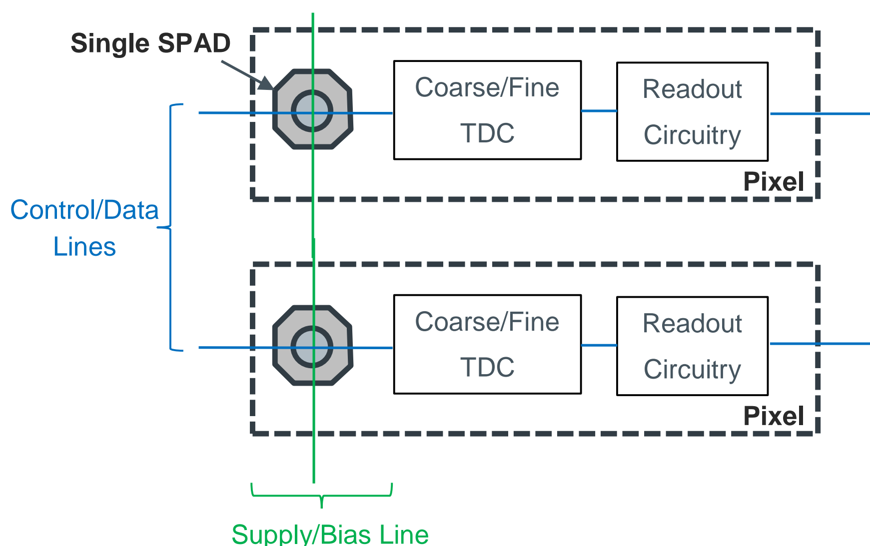

Figure 81: Fully parallel single-pixel concept

In consequence, a macro-pixel has several advantages, which have to be considered during system design. First the proposed macro-pixel can acquire four times more photons compared to the single-pixel thus increasing the pixel PDP at almost the same power consumption. The pixel area is less than two times a single pixel but has the strength of redundancy. Further, the sharing TDC concept should not lead to information lost because of the SPAD non-idealities, mainly dead-time is anyway a limiting factor. Furthermore, some ideas on SPAD readout concepts towards the TDC have been introduced which might decrease the after pulsing effects and could lead to a better handling with high photon events. Below a comparison table of the two introduced pixel concepts is given:

Parameter	Unit	Macro-pixel	Single-pixel
Technology	nm	Deep submicron TSMC CMOS	
SPADs	-	4	1
Pixel area	µm²	1051	600
Power consumption	µW @ 500kframe/sec	<9	

Table 15: Comparison of macro and single-pixel concept

In Figure 82, a structure proposal for a detection and readout system, based on the previous introduced macro-pixel concept will be given. Therefore, a modular kit is used to increase the numbers of pixels for the sensor. For the 2x2 macro-pixel array, a rolling shutter readout system shown in Figure 78 is used. The operation voltages for the SPAD are provided to the array by a 2bit input signal. The timestamps generated by the TDCs are readout by a data serializer and send to a processing circuit, which performs histogramming. Such an architecture is highly scalable, as we will see in the following calculations. Assuming a deep submicron TSMC CMOS process, for a 2x2 macro-pixel array approximately 4200µm² of silicon will be used. For a 16x16-macro pixel array, which obtains effectively 1024 SPADs a detector area of 0.27 mm² is calculated. Thus, the macro-pixel detector proposal herein is an improvement in size of factor 2 compared to the 32x32 single pixel device in 65nm CMOS presented in [78] with a detector area of 0.64mm².

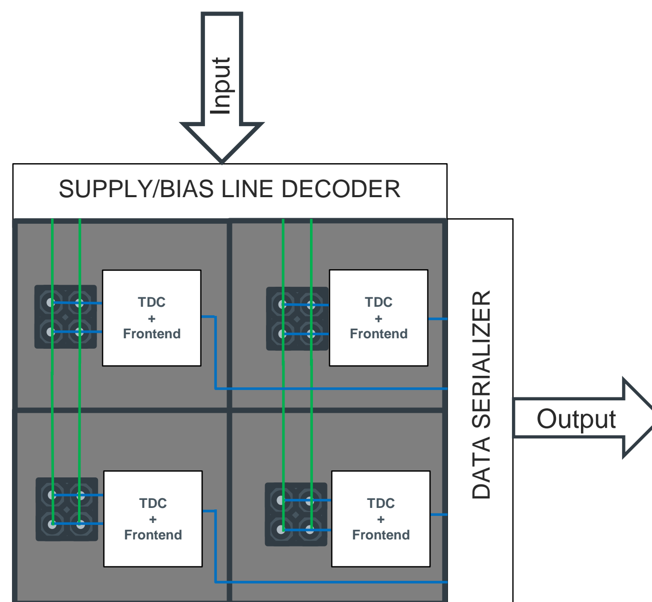

Figure 82: Structure of a 2x2-macro pixel array

A structure for a highly parallelized 3x3 single pixel concept is shown in a simplified way in Figure 83. Because each of the nine SPADs need, a separate supply and output line, a 4-bit input decoder and output data serializer would be needed. A column wise selection could be implemented reducing the effort to a 2bit input decoder, with the drawback of enabling and disabling column wise. However, the output overhead scales with the number of SPADs used. This applies, the scalability is reduced in full parallel single pixels. For a conceptual 4x4 single pixel array which has the same number of SPADs as a 2x2-macro pixel array, 9600µm² space is used, that is more than twice the size of the macro-pixel array. Nevertheless, compared to the 32x32-single pixel array in [78] approximately 5% improvement can be assumed. This is mainly achieved due to the small TDC area used.

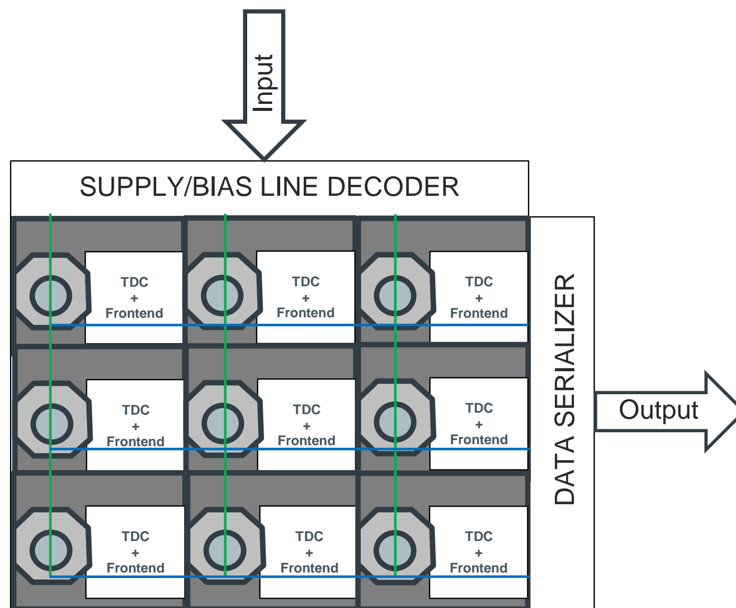

Figure 83: Structure of a 3x3-single pixel concept

Finally, to be able to compare these concepts in terms of power consumption and area size with the 65nm approach in [78], the pixel concepts have been scaled to an equally amount of SPADs. Therefore in Figure 84, a comparison table is given. It shows impressively that a macro-pixel has high advantages compared to a single-pixel in terms of power consumption and detector area.

Parameter	Unit	Macro-pixel concept	Single-pixel concept	[78]
Technology	nm	deep submicron TSMC CMOS		65nm
Number of pixels		16x16	32x32	32x32
SPADs	-	1024		
Pixel area	µm²	1051	600	625
Detector area	mm²	0.27	0.61	0.64
Power consumption per pixel	µW @ 30frames/sec	0.54*		1.05
Power consumption of detector	mW @ 30frames/sec	0.14*	0.55*	1.1
*Estimated TDC power consumption at 30frames/sec from [84]				

Figure 84: Comparison table of the pixel concepts to another approach assuming a detector array of 1024 SPADs

Nevertheless, to confirm these theoretical results and to come to a more precise estimation, simulations of the pixel concept have to be performed.

5 Electromagnetic Interference (EMI)

The aim of this chapter is to show the relevance of EMI in a TOF-chip in order to prevent too high emissions in a final product. In the following paragraph, effects of the VCSEL signal shape in terms of its frequency spectrum will be described and main design rules preventing EMI stated.

The ideal signal shape for a pulsed modulated light source provided by the VCSEL driver is a periodical squared wave (Figure 48) with its corresponding duty cycle, equation (3.8).

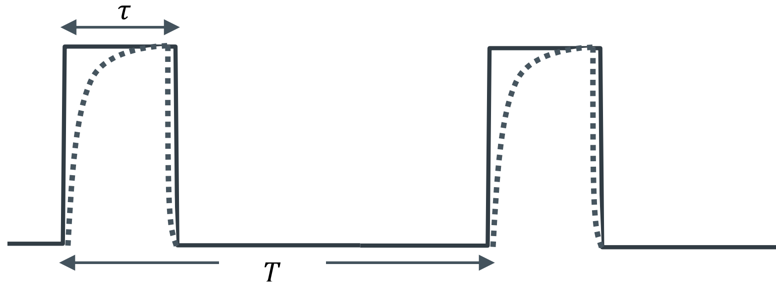

Figure 85: Ideal square waved pulses compared to real pulse shape of a VCSEL (dotted lines)

In case of the VCSEL driver used in the ST-VL6180x the duty cycle can be calculated as follows:

$$D = \frac{\tau}{T} = \frac{3{,}3ns}{10ns} \cdot 100\% = 33\% \tag{3.8}$$

As it can be seen above, square waved pulses are not realistic in a VCSEL and cannot be used for further EMI considerations. A commonly used approximation for on-chip clock signals rely on trapezoidal-shaped pulses as given below [89].

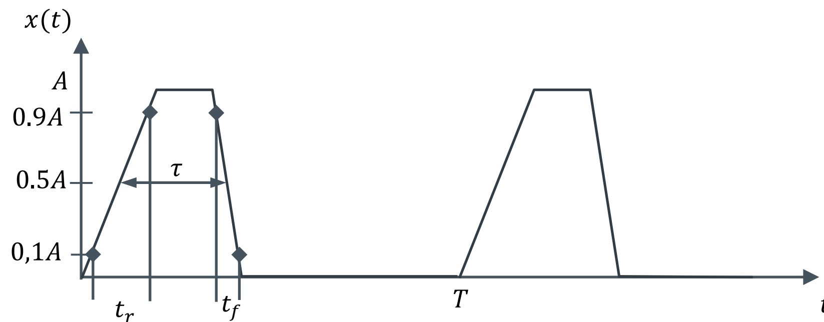

Figure 86: Characteristics of trapezoidal-shaped pulses for approximation

For a signal that consists of a periodic representation of trapezoidal-shaped pulses, each pulse can be described by its amplitude (A), pulse rise time (t_r), pulse fall time (t_f), pulse width (τ) and time period (T).

Once the interest is on the frequency spectrum of the trapezoidal signal, Fourier transformation is used. Before that it is assumed that the pulse rise and fall times are equal. In succession it is only refered to the pulse rise time (t_r). Under this conditions the analytically expression of the Fourier coefficients of the one-sided spectrum magnitude can be computed. The spectrum magnitude, which only exists at harmonics of the fundamental frequency, lies on the following envelope:

$$envelope_{dB} = 20\log\left(2A\frac{\tau}{T}\right) + 20\log|sinc(\pi t_r f)| + 20\log|sinc(\pi\tau f)| \tag{3.9}$$

In further consequence the three different logarithm parts can be plotted together in a bode diagram [90].

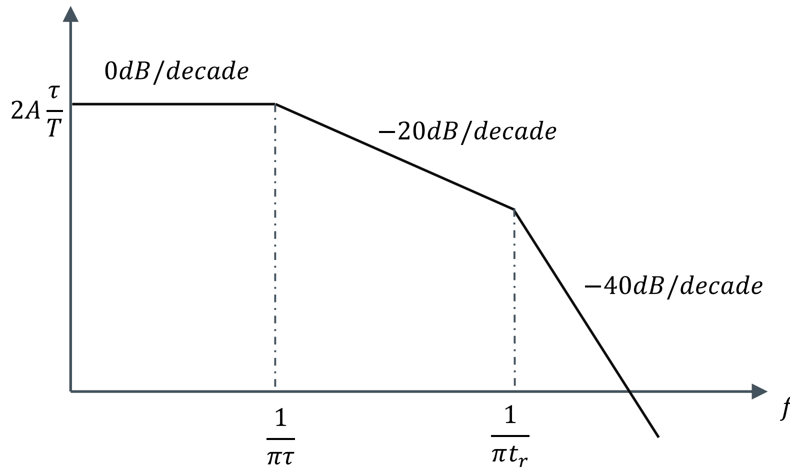

Figure 87 Bode plot of the trapezoidal digital pulse [90]

There are two breakpoints in the bode diagram, the first is related to the pulse width of the signal and the second to the rise time of the signal. Reducing the rise time will shift the second breakpoint to the right, hence increasing the amplitudes of the higher frequency harmonics and vice versa [90].
This particular case will be investigated in a comparison plot of two trapezoidal signals with different rise times ($t_{r1} = 500ps$ and $t_{r2} = 100ps$) suitable for VCSEL based TOF applications.

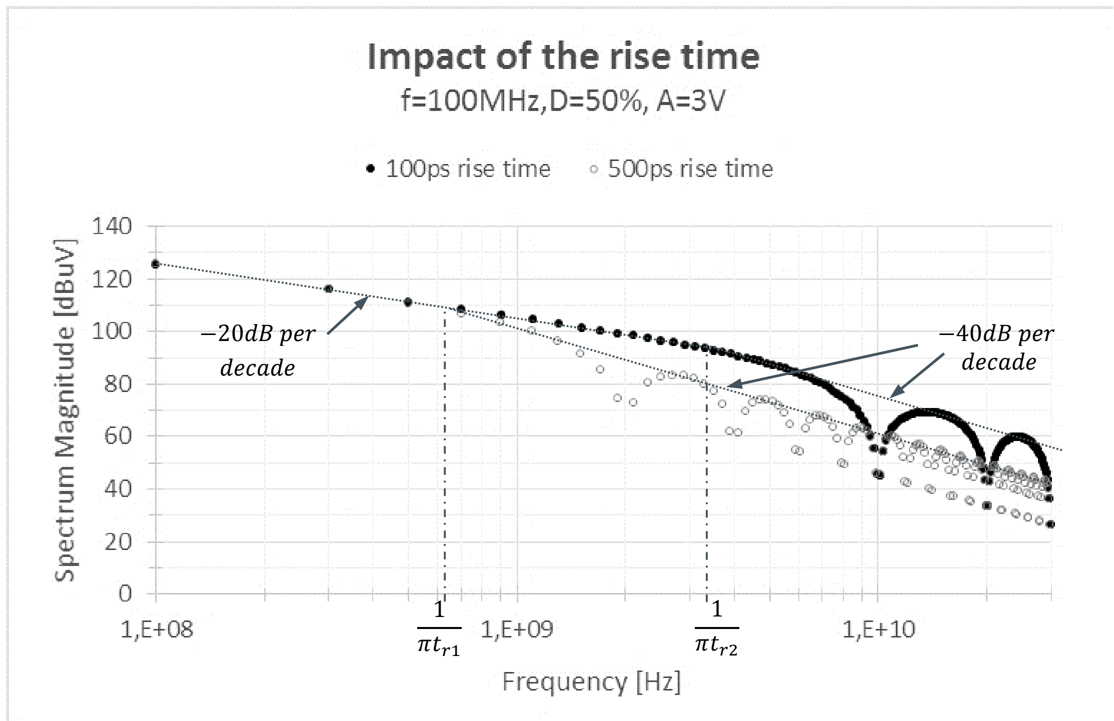

Figure 88: Magnitude spectra of trapezoidal waveforms with different rise times, the fundamental frequencies are in both cases 100 MHz and the duty cycle is 50%

As can be seen in Figure 40, the rise time has a dramatically effect on the magnitude of the high frequency content and in further consequence on the emissions of the product. Another variable impacting the magnitude of the harmonics is the signal frequency. Increasing the frequency, shifts the first breakpoint to higher frequencies hence the -20dB/decade begins later. This circumstance is plotted below:

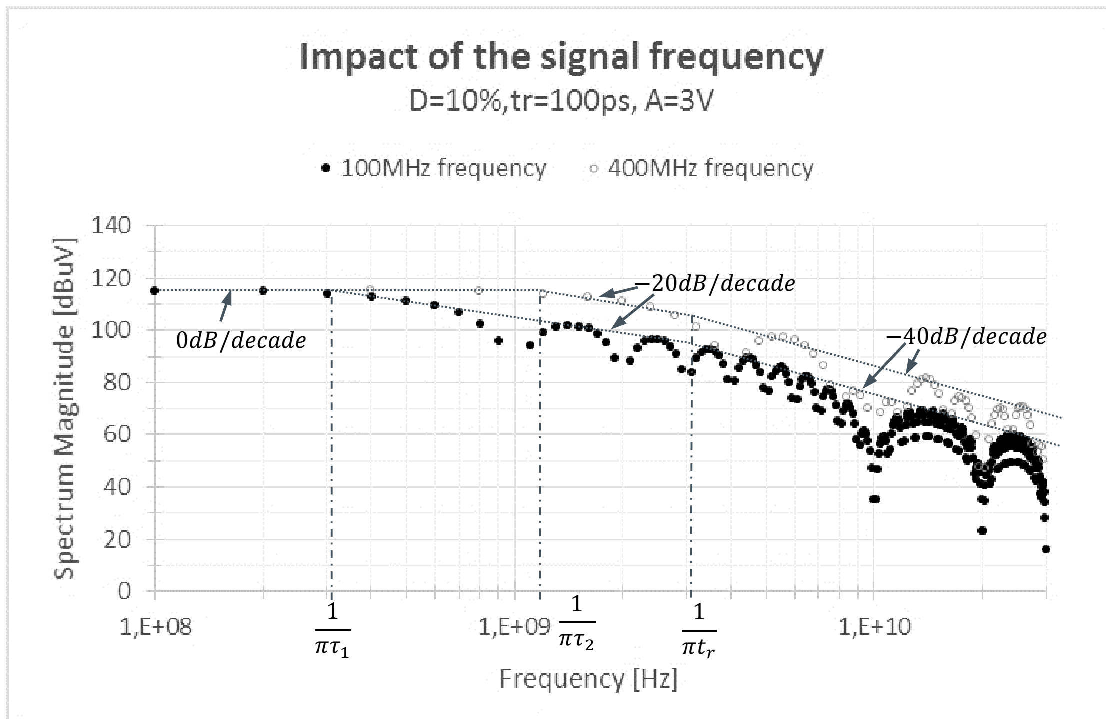

Figure 89: Comparison of the harmonic spectrum of two trapezoidal signals with different frequencies, the amplitude is 3V, the duty cycle is changed to 10% and the rise time is 100ps.

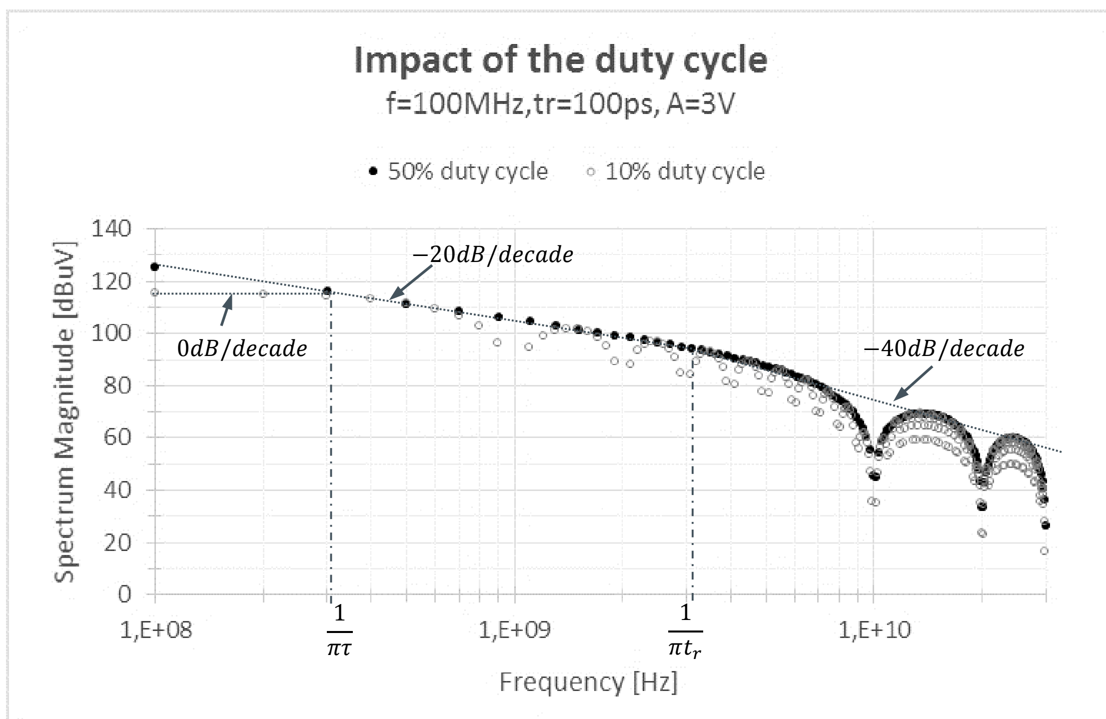

Figure 90: Impact of the duty cycle for a trapezoidal wave with constant Amplitude: 3V, rise time: 100ps, frequency: 100MHz and two different duty cycles 10% and 50%.

As can be seen in Figure 42, a decrease on duty cycle decreases the magnitude of the fundamental frequency. The first breakpoint is shifted to higher frequencies, hence the lower harmonics are reduced in amplitude. Analytically, the envelope of the magnitude spectrum with 50% duty cycle has a slope of 0dB per decade until it reaches the first breakpoint given by:

$$1.\,\mathrm{breakpoint}_{50\%\ duty\ cycle} \rightarrow \frac{1}{\pi\tau} = \frac{1}{\pi \cdot D \cdot T} = \frac{1}{\pi \cdot D \cdot \frac{1}{f}} = \frac{1}{\pi \cdot 0{,}5 \cdot \frac{1}{100MHz}} = 63{,}66\mathrm{MHz} \tag{4}$$

This frequency is lower than the fundamental frequency itself. Therefore, the envelope is plotted beginning with a slope of -20dB per decade at the fundamental frequency of 100MHz. When decreasing the duty cycle to 10% the first breakpoint shifts to higher frequencies as given by:

$$1.\,\mathrm{breakpoint}_{10\%\ duty\ cycle} \rightarrow \frac{1}{\pi\tau} = \frac{1}{\pi \cdot D \cdot T} = \frac{1}{\pi \cdot D \cdot \frac{1}{f}} = \frac{1}{\pi \cdot 0{,}1 \cdot \frac{1}{100MHz}} = 318{,}31\mathrm{MHz} \tag{4.1}$$

Both envelopes decrease at a rate of -20 dB per decade until they reach the second breakpoint, which can be expressed as:

$$\frac{1}{\pi t_r} = \frac{1}{\pi \cdot 100ps} = 3{,}18\mathrm{GHz} \tag{4.2}$$

After this, both envelope decreases at a rate of -40dB per decade.

As it was discussed, the controls for the envelope of the magnitude spectrum of a trapezoidal wave are given by the three variables rise time, duty cycle and signal frequency. Once, in VCSEL TOF applications the focus lies on fast rise times to prevent noise on the detection side, a low pulse width to save power and a high frequency to obtain high resolution, hence the controls are specified instinctively. In further consequence, unwanted emissions may be generated and might cause EMI. However, the following table gives a breakdown on the trade-offs for a pulsed TOF signal.

	Emissions (EMI)	**Distance accuracy**	**Power**
Decrease Rise and Fall time	−	+	neutral
Reduce Pulse width	+	+	*increases Peak optical power*
Increase Signal frequency	−	+	−

Table 16: Trade-off in TOF using pulsed signals whereby a “-“indicates a negative and “+” a positive effect on a TOF system.

In Table 16, on the one hand, a decrease in rise and fall time is desired in TOF but it leads to negative effects in terms of higher emissions. On the other hand, it has a positive effect on the distance accuracy. An increase in signal frequency increases the achievable distance accuracy with the drawback of higher emissions and power consumption.

In further consequence, it is necessary to investigate in the frequency bands, which are used in mobile phones. Additionally, these frequency bands have to be matched with the trapezoidal signal spectrum in order to evaluate their impact. In Figure 91 the frequency bands used in mobile phones are plotted together with the harmonics caused by a trapezoidal signal with 10% duty cycle, 100ps rise time, 3V Amplitude at a modulation frequency of 100MHz.

It shows dramatically, that several frequency bands are influenced. Even the 5GHz WLAN band is effected by a magnitude of 90dBµV of the higher harmonics.

At this point the impact on the mobile phones frequency bands is shown sufficiently. In further consequence it's absolutely necessary to do simulations on a VCSEL driver design to see if the theoretically ascertained emissions can be confirmed. Additionally, EMI measurements in an early product should be conducted as well.

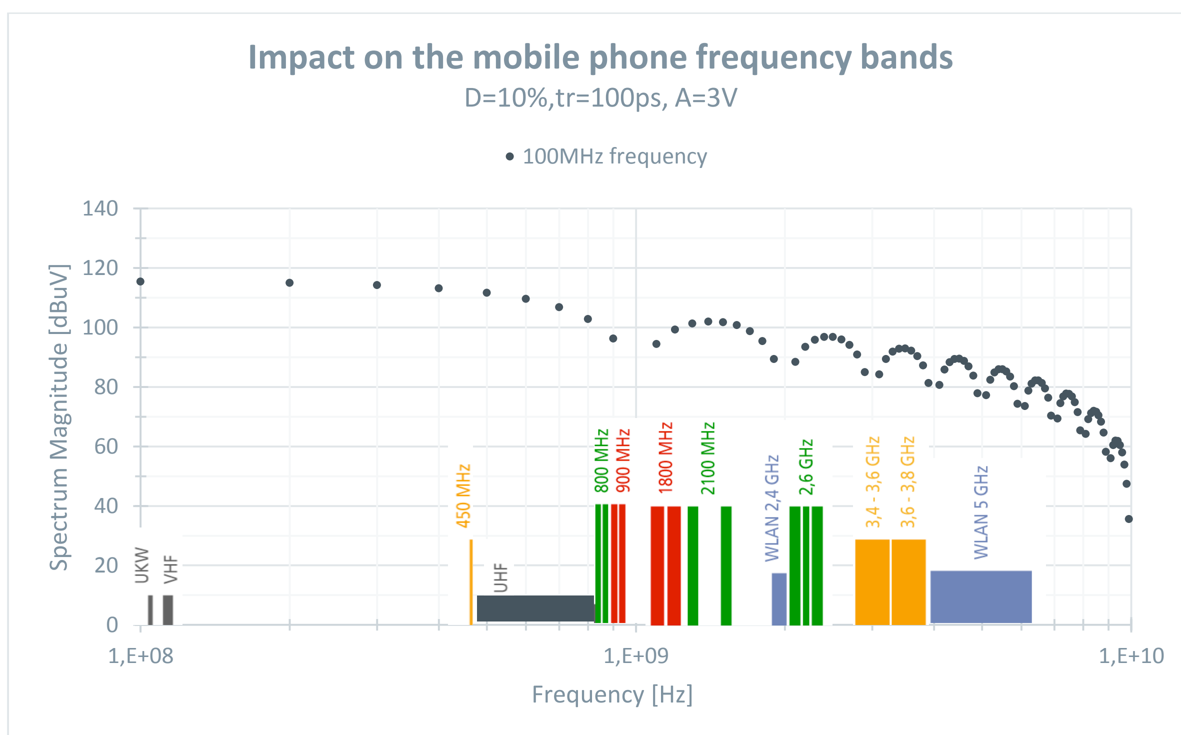

Figure 91: Overlap of the harmonics caused by a trapezoidal pulse (duty cycle: 10%, rise time: 100ps, Amplitude: 3V, frequency: 100MHz) and the frequency bands used in mobile phones

To conclude, trapezoidal-waves are rich in harmonics and the EMI effects on the system have to be considered through the system design. Another factor can reduce EMI essentially namely design rules in digital and analogue circuit design. An analogue design, which includes a high frequency (HF) oscillator or other high di/dt circuits, must follow HF design principles. Especially in this case are the ground rules, which have to be considered, they are:

- Identify the circuits of high di/dt (for emissions) e.g. clocks, bus buffers/driver, high-power oscillator
- Identify sensitive circuits (for susceptibility) e.g. low-level analogue, fast digital data
- Minimize their ground inductance e.g. minimizing the length and enclosed area
- Apply partitioning wherever possible
- Ensure that internal and external ground noise cannot couple of or into the system
- Create, maintain and enforce a ground map

Furthermore, every processor-based circuit such as the processing circuit in TOF is prone to corruption by fast transients which can cause the execution of false states. Great care is therefore necessary to prevent any clocked circuit from being susceptible to incoming interferences [91].

6 Economy

In every company, a good synergy between customer and product is the secret of success. A product will be profitably sold if the customer is willing to buy it and the costs are lower than the price. However, the ways of generating a valuable and profitable product can be distinguished by their starting point of consideration.

In Figure 92, a value based perception is given whereby the customer is primarily considered. This supposes, from the customers point of view that every product has its value compared to the price paid for it. Therefore the customer values the product and is willing to pay a certain price. The component manufacturer has to estimate this value for the customer.

Figure 92: Value based perception [92], modified

With a value based approach the firm requires a very clear view on the customer segments to be served, as well as the knowledge of the specific value it creates for each segment. The product price is based on the generated value and the costs are considered at the end [92].

The opposite way is chosen with a cost based perception, given in Figure 93. Thereby the process begins with the product related costs. Based on a cost calculation a profitable price is set before taking the value created for customers into consideration [92].

Figure 93: Cost based perception [92], modified

However, both perceptions do not exclude each other. Instead, the customer-product synergy should be considered in both ways. To maximize the profitability an increase on generated value and decrease in costs is desirable. Finally, both strategies will lead to a win-win situation for the customer and the manufacturer of the product as given in Figure 94 below.

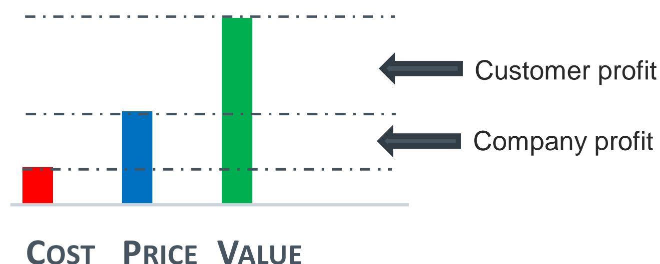

Figure 94: From cost to value, a win-win situation

6.1 TOF Product Cost and Price

In every product development, the main economic parameters are the costs and the price. To be competitive a price must be targeted which covers the expenses and hits the willing margin to have profit. Cost drivers must be elicited, thus detailed knowledge of the costs is essential to place a successful product on a global market. Additionally the question, what is a customer willing to pay, is an essential input for the choice of pricing strategy. This chapter will give a view on the costs, which are arising in IC production, which can be separated, into two major components fixed costs, and variable costs. Both will be explained in the following subchapters and example calculations will be given as well as price building strategies will be discussed.

6.1.1 Fixed Costs

Among non-recurring engineering costs (NRE) there are costs that are spent once during the development of a product. They are also called fixed costs. Generally, NREs are independent of the sales volume or the number of products sold. They mainly depend on the internal engineering effort (Personnel costs) as well as the manufacturing tooling costs. A decision towards a new technology requested by a customer can increase research and development expenses (R&D) dramatically. Further cost driver can be a high design complexity, a low productivity of the design team, high equipment and tooling costs or even many purchased services. Excessive expenses on NRE should be considered with care because they can lead to a non-attractive investment. A calculation schema for NRE costs is given in Figure 95 where the figures are suppositious.

FIXED COSTS (NRE)			
ENGINEERING COST			
Item	**Quantity**		**Amount**
Personnel cost	Hours	Rate	
Design engineering work	800	100	$80.000,00
Layout engineering work	200	100	$20.000,00
Test engineering work	600	100	$60.000,00
RESEARCH AND DEVELOPMENT COST			
Item	**Quantity**		**Amount**
Mask cost			
Mask+Wafer			$42.000,00
Packaging cost			
Assembly			$5.000,00
Testing cost			
Test Hardware			$20.000,00
Support cost			
Evaluation PCB			$8.000,00
Total			**$235.000,00**

Figure 95: Fixed costs (NRE) calculation schema

6.1.2 Variable Costs

The variable costs are defined as the recurring expenses that occur with every produced unit. They contain die costs, test costs and assembly costs. In the following section an estimation of the variable costs for the TOF sensor ST-VL6180 will be given. To start with, out of the sensors microphotograph it can be determined that the ST chip has a die size of 5mm² in 0.13µm process. If the size of each technology block is given separately, the die size could be estimated with the scheme below:

Chip Silicon Area		
Item	**Amount**	**Unit**
Technology	**0.13**	**µm**
PLL	1	mm^2
I2S	1	mm^2
I2C	1	mm^2
DAC-digital	1	mm^2
DAC-analog	1	mm^2
Total	**5**	**mm^2**

Figure 96: Estimated die size of the ST VL-6180 with suppositious figures

However, 5mm²-silicon area are assumed for the further calculation without knowing each block size. The next step is to get reliable prices for a silicon wafer in the desired process geometry. Therefore, published prices for 200mm and 300mm wafers are used, which are continuously reported by the Global Semiconductor Alliance. The 4Q14 price for a 200mm wafer in 130nm process is marked in Figure 97 below:

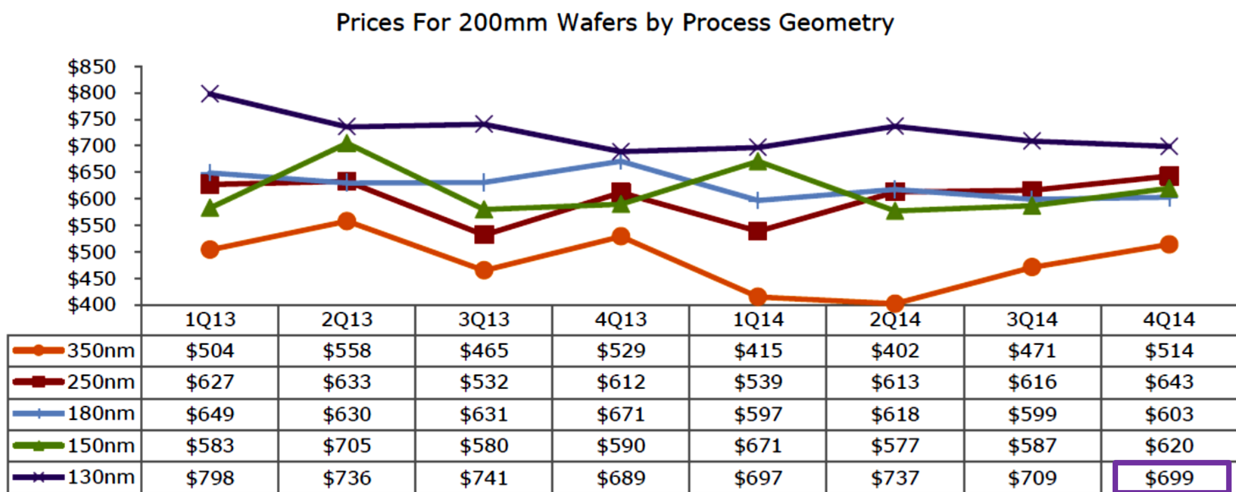

	1Q13	2Q13	3Q13	4Q13	1Q14	2Q14	3Q14	4Q14
350nm	$504	$558	$465	$529	$415	$402	$471	$514
250nm	$627	$633	$532	$612	$539	$613	$616	$643
180nm	$649	$630	$631	$671	$597	$618	$599	$603
150nm	$583	$705	$580	$590	$671	$577	$587	$620
130nm	$798	$736	$741	$689	$697	$737	$709	$699

Figure 97: Wafer pricing report [93]

First, the gross amount of dies per wafer (GDW) respectively dies per wafer (DPW) for a given wafer size have to be calculated. Thus, a mathematical approximation is needed to calculate the exact GDW count. In [94] an investigation of GDW formulas is given, whereby equation 4.3 is recommended to deliver exact results.

$$\mathrm{GDW} = \frac{\pi \cdot {R_{eff}}^2}{A} - \frac{\pi \cdot 1.16 \cdot R_{eff}}{\sqrt{A}} \tag{4.3}$$

With A is the die area including the scribe lane and R_{eff} is the physical radius minus a fixed edge exclusion, typically in the range of 1 to 5 mm [94]. A GDW of 5875 pieces is calculated assuming an edge exclusion of 2mm. The result has been proven using an online calculation tool in [95] with minimal divergence as can be seen in Figure 98.

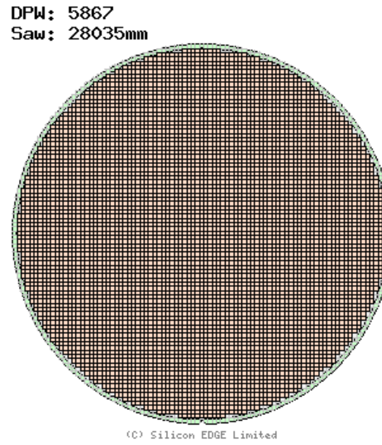

Figure 98: Silicon EDGE dies per wafer estimator [95]

The DPW count is listed in Table 17 and will be in the next step reduced by another important factor namely die yield. It can be defined as the percentage of good dies in a production batch. The die yield corresponds to the following equation:

$$\text{Die yield} = \text{Wafer yield} \cdot \left(1 + \frac{\textit{Defects per unit area} \cdot \textit{die area}}{\alpha}\right)^{-\alpha} \tag{4.4}$$

Whereby the parameter α stands for process complexity, which is directly linked to the number of steps and is typically around three [96]. A die yield exceeding 95% is reported for TSMC 200mm wafer in [97]. In practice, the wafer fab provides die yield after screening out bad devices with probe or wafer sort. Furthermore, the count of good dies for one wafer is given by:

$$\text{Good dies} = \text{DPW} \cdot \text{Die yield} \tag{4.5}$$

With the wafer costs from Figure 97, the die costs per wafer can be calculated with the equation below:

$$\text{Die cost} = \frac{\textit{Wafer cost}}{\textit{good dies}} \tag{4.6}$$

Matching the costs to the IC fabrication process cycle it can be concluded that a count of 5580 good dies at a price of 0.13$ per unit is obtained which has to be assembled in the next process step. Therefore, additional costs namely assembly costs must be added. These costs are assumed to be 0.4$/unit for the ST-VL6180

because of the costly package. In the next step the assembled device has to be final tested which concludes additional test costs. Finally, the IC costs are given by:

$$\text{IC costs} = \frac{Die\ cost + Test\ cost + Assembly\ cost}{Final\ test\ yield} \tag{4.7}$$

Whereby the final test yield is defined as the units passing final test (output) divided by the units tested (input). This implies a final test yield of ideally 100% is intended. A high final test yield is a major task for every fab because a decrease in yield from 98% to 58% would increase the IC costs for e.g. the ST device to 1$.

To summarize, a variable cost break down is a very important tool, which leads to the IC costs. These particular cost figures represents all recurring expenses arising during the manufacturing process of a single IC. An important mechanism for lower IC costs is a yield improvement. As yield improves, volume increases, hence with approximately 10% cost decrease for doubling volume. Beside of manufacturing losses other cost drivers must be considered, as they are costs for the raw material and packaging.
In the following Table 17 the described cost breakdown is given for the ST device. It can be seen that the package costs are dominantly with a percentage of 67% of the IC costs.

VARIABLE COSTS (RE)		
DIE COST		
Item	**Amount**	**Unit**
Dies per wafer	5875	pcs.
Die yield	95	%
Good dies	5580,92	per wafer
Wafer cost	699	$
Total	**0,13**	**$**
ASSEMBLY COST		
Item	**Quantity**	**Unit**
Total	**0,4**	**$**
TEST COST		
Item	**Quantity**	**Unit**
Total	**0,05**	**$**
Final test yield	98	%
IC COST = $0,59		

Table 17: Calculation scheme for the variable costs

In the calculation, a 200mm wafer is assumed, because of the process node and the available price information's. In Figure 99 it can be seen that the assumed wafer size is still outdated. In this context an actually question should be answered. What is the benefit of increasing wafer size to 300mm or even 450mm wafers?

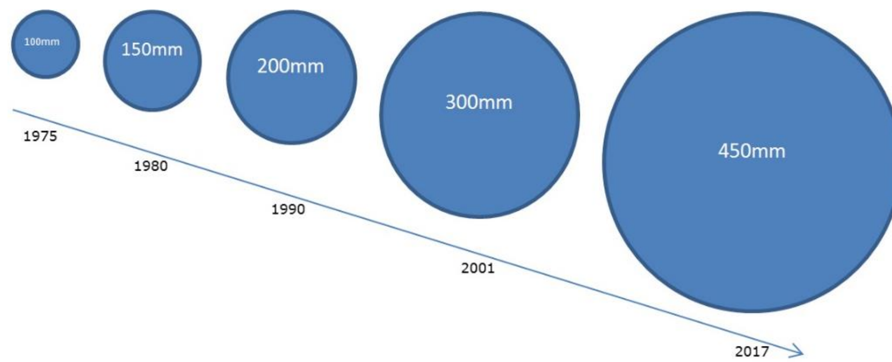

Figure 99: Increase on wafer diameters over the years [98]

To answer this question let us assume a given die size 5mm² and 2mm edge clearance using the earlier GDW equation. If it is the intention to process the chip in a 200mm fab A with a capacity of assumed 40-45k wafer starts per month another can produce the same amount of chips in a 300mm fab B with approximately 18k starts per month and a third one needs approximately 8k starts per month in a 450mm fab C. It follows that fab A has 5 times more workload and may has already reached its workload limits. However, this makes only sense if the percentage increase in NRE costs per wafer from the new technology is smaller than the increase in revenue thanks to the expected lower RE costs. Practically, a push in process node down to e.g. 14nm with 450mm wafers is necessary to be competitive while hitting the margins [98].

6.1.3 Pricing

In many conversions with engineers regarding the best technology, choice for our product the question raised what price might be achieved for our product. Moreover, sometimes it was mentioned that marketing is very easy to understand. It might be assumed, that you have to sell the product for more than it costs and that's enough for sufficient profit.

As it can be seen in the previous section, cost breakdown can give a rough hint on the costs. However, the price cannot be systematically generated because in addition to costs and profit it has an uncontrollable psychological component, which even the best companies are not able to control. One way to simplify the problems is to do a good branding for the product. As this is often very difficult to implement, there is still another option, which is referred to as pricing strategy.

In the next subchapters a small selection of possible pricing strategies will be given. For additional information, please refer to [99].

6.1.3.1 Price Skimming

From the viewpoint of a company, the strategy with the most "skimming" profit is often referred to as price skimming. This pricing strategy is also known as what the market will bear (WTMWB) [100]. Price skimming implies that the company sets the price to the maximum price level the market will accept. Thus, the strategy focuses mainly on innovators and early adopters they are willing to pay for the uniqueness of a new product. This strategy is well applicable for startups to refinance high research and development (R&D), marketing and production costs.

Another factor, which simplifies price skimming for a company, is a high patent protected product. This advantage holds as long as patent protection maintains, but usually the desirability expires earlier.

6.1.3.2 Price Penetration

This strategy is used to maximize sales, by setting a relatively low initial price, which gains market acceptance quickly, and in consequence, a large market share can be achieved. Penetration pricing focuses on price sensitive customers in contrast to price skimming. Such a strategy can be employed when the R&D and marketing expenses are relatively low. Another factor making price penetration interesting is, when new competitors enter the market. In this case, a quick management decision is necessary to lower the price thus making the competing startup uninterested and maximize the sales for your own company. Nevertheless, a company how wants to employ price penetration must have cost structures and scale economies that allow narrow profit margins [99].

6.1.3.3 Gross Profit Margin Target

Another pricing strategy used is called Gross Profit Margin Target (GPMT). This strategy is based on the Gross Profit Margin index, indicating what remains from sale when the expenses are paid to generate positive net income and cash flow. GPM is quoted in percentage and defined by the equation below:

$$\mathrm{GPM} = \frac{Revenue - COGS}{Revenue} \tag{4.8}$$

, whereby COGS are cost of goods sold [101]. For example if a company sells $50,000 worth of goods and its COGS were $25,000, the GPMT would be equal to 50%. The same idea can be used for product pricing, if we simply replace “Revenue” by “Price” and we rearrange the formula above it leads to:

$$\text{Average selling price} = \frac{COGS}{1 - GPM} \tag{4.9}$$

If we would have employed a GPMT strategy, we can use the above equation for calculating the price of a TOF product. From the previous variable costing we have calculated IC costs i.e. COGS which are for the ST device approximately 0.59$ and we assume our company aims for a GPM of 50%, thus the average selling price for the ST chip would be 1.18$.

GPMT strategy is that it does not exclude another pricing strategy instead, it can be employed together with other pricing strategies.

Usually companies know the GPMT they want, however some indexes were found in [100]:

- Manufacturers typically aim for a GPMT of 50%
- Distributors (Wholesalers) usually need a GPMT of 10 to 15%
- Dealers (Retailers) require a GPMT of 30%(without after-sale support) and up to 50% (with after-sale support)

Nevertheless, an advantage of GPMT strategy is that it does not exclude another pricing strategy, instead it can be employed together with other pricing strategies and can be perfectly used for analysis purpose.
In this context another interesting aspect is given in [102], saying that globally GPMT differentials exist. For example, companies in the U.S. target a GPM of 60 to 70% compared to China with only 5-10%. This exhibits impressively the press of global business.

7 Conclusion

In this diploma thesis, an extensive overview on TOF technology was given, the main measurement principles were described in detail and several detector technologies reviewed. A major effort was put into investigations on published state of the art TOF sensors as well as commercial available cameras. Reviews have been carried out for the SPAD based sensor ST-VL6180 in the LG G3 phone and for two additional in-pixel based cameras PMD CamBoard pico and SoftKinetic SENZ 3D. In this context practical observations were reported and measurement results presented. In a next step, requirements have been worked out for a low cost and low power 3D TOF camera which can be used for gesture recognition, proximity sensing and autofocus assistance. Furthermore, a technology decision between CAPD and SPAD was realized and the results are given. From this time on a SPAD based TOF concept, which is best suitable for low cost, low power TOF cameras for use in mobile phones and tablets, was considered. At this point a SPAD based TOF camera system was partitioned and the main building blocks were analyzed in terms of performance, power consumption and size. A subchapter was dedicated to the light source and it was shown that VCSEL has many benefits over LED in TOF concerning performance and power consumption. Additionally a concept was introduced for a highly parallelized single and macro pixel, showing that a coarse-fine ring oscillator TDC serves best for our desired product. This chapter was followed by an investigation on electromagnetic interferences in TOF sensors. Therefore, Fourier spectrum analysis was conducted for a trapezoidal signal. It was shown that the high modulation signals in TOF will cause unavoidable emissions which will have an impact on the mobile phones frequency bands. At this point additional knowledge was given to prevent EMI. Along with the technical achievements on the subject of TOF the economic perspective was another essence of this thesis. Therefore an investigation into costs was given, whereby the costs were divided into non-recurring expenses and recurring expenses. Both costs were described and cost drivers shown. Beyond a calculation model for RE was presented and the IC costs for the VL6180 exemplary calculated. Finally, a price was proposed for the latter TOF device and important pricing strategies were shown.

8 Prospect

A future work might pick up the theoretically considerations presented herein and makes use of the knowledge in order to perform system simulations. Following this, a SPAD based TOF prototype would be a corollary. However, during my investigation in TOF some difficulties were noticed which I would like to bring in. One issue was the insufficient comparability of TOF sensors in general, because no unified figures of merit existed, and often performance parameters were not given. Furthermore, many key performance parameter, like the maximum measurable distance and the distance measurement uncertainty were measured by non-uniform measurement systems without connection to an application. Therefore, a proposal for a future work is to provide ideas to unify TOF. This implies that, a TOF benchmarking system is required. An outline for possible benchmark parameters in TOF is given in Figure 100 below:

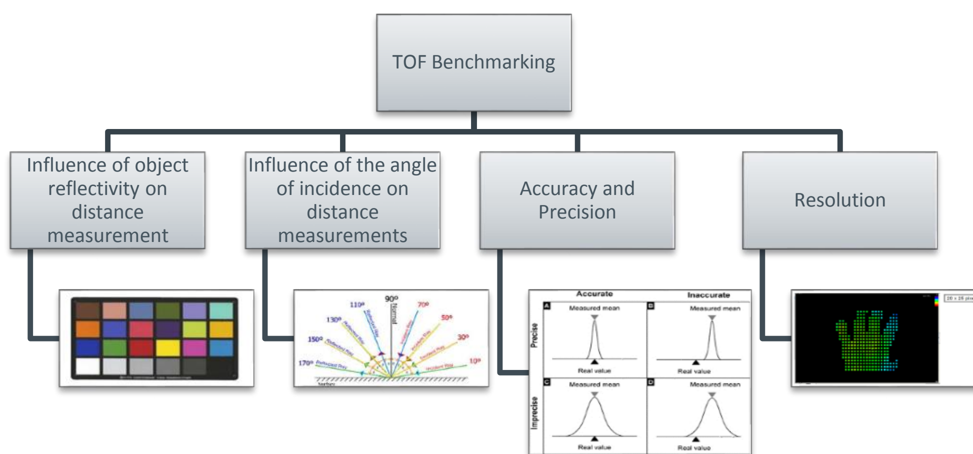

Figure 100: TOF benchmarking parameters

In consequence, for each TOF application, e.g. gesture recognition for a specific application field e.g. mobile devices, benchmark parameters should be developed and standards in measuring methods as well as definitions on measurement setups defined. A proposal for a benchmarking system regarding gesture recognition in mobile devices is given in Table 18.

TOF camera A	Benchmark: TOF device performance	TOF camera B
Good	Sensor resolution	Good
Poor	Working range	Quite good
Good	Distance precision and accuracy	Good
Very good	Sensitivity to sunlight	Poor
Good	Angle of incidence stability	Good
TOF camera A	**Benchmark: Application specific**	**TOF camera B**
Good	Hand gestures e.g. wipe, finger detection, gesture interpretation	Quite Good
Poor	Facial expressions e.g. laugh, cry	Good
Good	Object color sensitivity	Good
Poor	Fast, slow movements	Quite Good

Table 18: Benchmarking proposal gesture detection in mobile devices

9 Appendix

Distance (cm)	Time (s)	Good results of 10=100%	Ambient light (lux)
5	2,0-2,4	0	10
10	1,8-2,2	1	14
15	1,7-2	4	14
20	1,5-1,8	4	18
25	1,6-1,8	7	10
30	1,7-1,9	9	13
35	1,7-2,1	8	20
40	1,5-1,8	8	20
45	1,1-1,4	10	30
50	1,0-1,2	10	34
60	1,1-1,4	10	33
70	1,1-1,5	10	35
80	1,0-1,2	10	32
90	0,9-1,4	10	31
100	1,0-1,2	10	30
110	0,9-1,2	10	45
120	1,0-1,2	10	70
130	0,8-1,1	10	65
140	1-1,6	10	70
150	1,0-1,3	10	74

Measurements results for a reflective target without TOF autofocus

Distance (cm)	Time (s)	Good results of 10=100%	Ambient light (lux)
5	1,1-1,4	0	42
10	1,1-1,5	5	34
15	1,2-1,5	9	36
20	1,1-1,6	10	38
25	1,0-1,6	10	56
30	1,0-1,4	10	65
35	0,9-1,1	10	86
40	1,0-1,4	10	88
45	0,9-1,2	10	89
50	0,9-1,3	10	83
60	0,9-1,4	10	74
70	1,0-1,2	10	79
80	1,0-1,3	10	74
90	1,2-1,4	10	76
100	1,3-2,0	10	78
110	1,1-1,2	10	83
120	1,2-1,4	10	86
130	1,2-1,6	10	92
140	1,1-1,4	10	81
150	1,2-1,9	10	84

Measurements results for a reflective target with TOF autofocus

10 Bibliography

[1] P. J. Besl, "Active, Optical Range Imaging Sensors," in *Machine Vision and Applications*, Springer New York, 1988, pp. 127-152.

[2] C. Niclass, "Single-Photon Image Sensors in CMOS: Picosecond Resolution for Three-Dimensional Imaging," in *PHD Thesis*, University of Lausanne, 2008.

[3] F. Remondino and D. Stoppa, TOF Range-Imaging Cameras, Springer , 2013.

[4] S. Cova and M. Ghioni et al., "Avalanche Photodiodes and Quenching Circuits for Single-Photon Detection," *Applied Optics,* vol. 35, no. 12, pp. 1956-1976, 1996.

[5] M. Fishburn, "Fundamentals of CMOS Single-Photon Avalanche Diodes," in *PHD Thesis*, University of Delft, 2012.

[6] M. Karami, Y. Hyung-June and E. Charbon, "Single-Photon Avalanche Diodes in Sub-100nm Standard CMOS Technologies," in *Int. Image Sensor Workshop (IISW)*, Onuma, Hokkaido, 2011.

[7] F. Villa et al., "CMOS single photon sensor with in-pixel TDC for Time-of-Flight applications," in *Time-to-Digital Converters (NoMe TDC)*, IEEE Nordic-Mediterranean Workshop , 2013.

[8] M. Karami, "Deep-Submicron CMOS Single Photon Detectors and Quantum Effects," in *PHD Thesis*, University of Delft, 2011.

[9] M.-J. Lee et al., "A first Single-Photon Avalanche Diode fabricated in standard SOI CMOS technology with a full characterization of the device," *Optics Express,* vol. 23, no. 10, pp. 13200-13209, 2015.

[10] S. Cova et al., "Trapping Phenomena in Avalanche Photodiodes on Nanosecond Scale," *Electron Device Letters, IEEE,* vol. 12, no. 12, pp. 685-687, 1991.

[11] S. Cova et al., "20ps Timing Resolution with Single Photon Avalanche Diodes," Rev. Sci. Instrum. 60, 1104 (1989).

[12] PicoQuant, "Photon Counting Detectors PDM Series," PicoQuant, [Online]. Available: https://www.picoquant.com/products/category/photon-counting-detectors/pdm-series-single-photon-avalanche-diodes#images. [Accessed 4 8 2015].

[13] C. Niclass et al., "Design and characterization of a CMOS 3-D image sensor based on single photon avalanche diodes," *Solid-State Circuits, IEEE Journal,* vol. 40, no. 9, pp. 1847-1854, 2005.

[14] T. Instruments, "Introduction to the Time-of-Flight (ToF)," 2014. [Online]. Available: http://www.ti.com/lit/ml/sbau219d/sbau219d.pdf. [Accessed 20 8 2015].

[15] T. Spirig et al., "The lock-in CCD-two-dimensional synchronous detection of light," *Quantum Electronics, IEEE Journal ,* vol. 31, no. 9, pp. 1705-1708, 1995.

[16] M. Lehmann et al., "Smart Pixels for future 3D-TOF Sensors," in *IEEE Workshop on Charge-Coupled-Devices & Advanced Image Sensors*, Karuizawa, Japan, 2005.

[17] R. Lange, "3D Time-of-Flight Distance Measurement with Custom Solid-State Image Sensors in CMOS/CCD-Technology," in *PHD Thesis*, University of Siegen, 2000.

[18] R. Schwarte et al., "New electro-optical mixing and correlating sensor: facilities and applications of the photonic mixer device (PMD)," *Proc. SPIE 3100,* p. 9, 1997.

[19] X. Luan, "Experimental Investigation of Photonic Mixer Device and Development of TOF 3D Ranging Systems Based on PMD Technology," in *PHD Thesis*, University of Siegen, 2001.

[20] P. Gulden et al., *Application of the Photoelectronic Mixing Device to Optical Measurement of Presence, Distance and Velocity,* Paris: Microwave Conference, 30th European, 2000.

[21] D. Nieuwenhove et al., "Novel Standard CMOS Detector using Majority Current for guiding Photo-Generated Electrons towards Detecting Junctions," Proceedings Symposium IEEE/LEOS Benelux, Mons, 2005.

[22] W. Tempel, D. Nieuwenhove and M. Kuijk, "Photonic mixer and use thereof". United States Patent US 8294882 B2, 23 10 2012.

[23] G.-F. Dalla Betta et al., "Design and Characterization of Current-Assisted Photonic Demodulators in 0.18-µm CMOS Technology," *Electron Devices, IEEE Transactions,* vol. 58, no. 6, pp. 1702-1709, 2011.

[24] B. Burkey et al., "The Pinned Photodiode for an Interline-Transfer CCD Image Sensor," *Electron Devices Meeting, International (Volume:30),* vol. IEEE, pp. 28 - 31, 1984.

[25] P. L. Paul et al., "Active Pixel Sensor integrated with a Pinned Photodiode". US Patent 5904493, 18 5 1999.

[26] E. R. Fossum et al., "A Review of the Pinned Photodiode for CCD and CMOS Image Sensors," *IEEE Journal Of The Electron Devices Society,* vol. 3, no. 2, p. 11, 2014.

[27] N. Junichi, Image Sensors and Signal Processing for Digital Still Cameras, CRC-Press, 2006.

[28] J. Illade-Quinteiro et al., "Custom Design of Pinned Photodiodes in Standard CMOS technologies for Time-of-Flight Sensors," in *Cellular Nanoscale Networks and their Applications (CNNA)*, Notre Dame, IN, 2014.

[29] D. Stoppa et al., "An 80×60 Range Image Sensor Based on 10µm 50MHz Lock-In Pixels in 0.18µm CMOS," *Solid-State Circuits Conference Digest of Technical Papers (ISSCC),* pp. 406 - 407, 2010.

[30] J. P. Dakin and R. G. W. Brown, Handbook of Optoelectronics (Two-Volume Set), CRC Press, 2006.

[31] E. Charbon, "Techniques for CMOS Single Photon Imaging and Processing," in *ASICON 2005. 6th International Conference*, Shanghai, 2005.

[32] R. J. Walker et al., "A 128×96 Pixel Event-Driven Phase-Domain ΔΣ-Based Fully Digital 3D Camera in 0.13µm CMOS," in *ISSCC*, San Francisco, USA, 2011.

[33] J. A. Richardson et al., "Low Dark Count Single-Photon Avalanche Diode Structure Compatible With Standard Nanometer Scale CMOS Technology," *IEEE Photonics Technology Letters,* vol. 21, no. 14, p. 3, 2009.

[34] C. Niclass et al., "Single-Photon Synchronous Detection," *IEEE Journal Of Solid-State Circuits,* vol. 44, no. 7, p. 13, 2009.

[35] C. Niclass et al., "A 100-m Range 10-Frame/s 340x96-Pixel Time-of-Flight Depth Sensor in 0.18- m CMOS," *IEEE Journal Of Solid-State Circuits,* vol. 48, no. 2, p. 14, 2013.

[36] C. Niclass et al., "A 0.18- m CMOS SoC for a 100-m-Range 10-Frame/s 200 96-Pixel Time-of-Flight Depth Sensor," *IEEE Journal Of Solid-State Circuits,* vol. 49, no. 1, p. 16, 2014.

[37] C. Veerappan et al., "A 160×128 Single-Photon Image Sensor with On-Pixel 55ps 10b Time-to-Digital Converter," *ISSCC 2011 / Session 17 / Biomedical & Displays / 17.7,* p. 3, 2011.

[38] C. Niclass et al., "A 128x128 Single-Photon Image Sensor With Column-Level 10-Bit Time-to-Digital Converter Array," *IEEE Journal Of Solid-State Circuits,* vol. 43, no. 12, p. 13, 2008.

[39] N. Dutton et al., "A Time-Correlated Single-Photon-Counting Sensor with 14GS/s Histogramming Time-to-Digital Converter," *ISSCC 2015 / Session11 / Sensors and Imagers for Life Sciences / 11.5,* p. 3, 2015.

[40] S.-J. Kim et al., "A Three-Dimensional Time-of-Flight CMOS Image Sensor With Pinned-Photodiode Pixel Structure," *IEEE Electron Device Letters,* vol. 31, no. 11, p. 3, 2010.

[41] S.-J. Kim et al., "A 640×480 Image Sensor with unified Pixel Architecture for 2D/3D imaging in 0.11µm CMOS," *VLSI Circuits (VLSIC), Symposium,* pp. 92 - 93, 2011.

[42] W. Kim et al., "A 1.5Mpixel RGBZ CMOS Image Sensor for Simultaneous Color and Range Image Capture," *ISSCC 2012 / Session 22 / Image Sensors / 22.7,* p. 3, 2012.

[43] G. Zach and H. Zimmermann, "A 2×32 Range-Finding Sensor Array with Pixel-Inherent Suppression of Ambient Light up to 120klx," *ISSCC 2009 / Session 20 / Sensors and Mems / 20.7,* p. 3, 2009.

[44] G. Zach, A. Nemecek and H. Zimmermann, "Smart Distance Measurement Line Sensor with Background Light Suppression and On-Chip Phase Generation," in *Proc. SPIE Infrared Systems and Photoelectronic Technology III*, vol. 7055, 2008.

[45] G. Zach et al., "A 16x16 Pixel Distance Sensor With In-Pixel Circuitry That Tolerates 150 klx of Ambient Light," *IEEE Journal Of Solid-State Circuits,* vol. 45, no. 7, p. 9, 2010.

[46] M. Davidovic et al., "Range Finding Sensor in 90nm CMOS with Bridge Correlator Based Background Light Suppression," *IEEE,* 2010.

[47] M. Davidovic et al., "High Dynamic Range Background Light Suppression for a TOF Distance Measurement Sensor in 180nm," p. 4, 2011.

[48] R. Jeremias et al., "A CMOS Photosensor Array for 30 Imaging Using Pulsed Laser," *ISSCC 2001 Session 16 Integrated Mems and Display Drivers,* p. 4, 2001.

[49] D. Stoppa et al., "A Novel Fully Differential Pixel Concept for Indirect TOF 3D Measurement," in *IMTC*, Vail, Colorado, 2003.

[50] D. Stoppa et al., "A 16x16-Pixel Range-Finding CMOS Image Sensor," in *Proc. of the 30th IEEE ESSCIRC*, pp. 419-422, 2004.

[51] M. Perenzoni et al., "A 160x120-Pixels Range Camera With In-Pixel Correlated Double Sampling and Fixed-Pattern Noise Correction," *IEEE Journal Of Solid-State Circuits,* vol. 46, no. 7, p. 10, July 2011.

[52] M. Perenzoni et al., "A 160×120-Pixels Range Camera with On-Pixel Correlated Double Sampling and Nonuniformity Correction in 29.1µm pitch," in *ESSCIRC*, Seville, 2010.

[53] "AIT Austrian Institute of Technology GmbH," [Online]. Available: http://www.ait.ac.at/research-services/aal-ambient-assisted-living/?L=1. [Accessed 30 8 2015].

[54] W. Van der Tempel et al., "A 1k-Pixel 3D CMOS Sensor," *IEEE,* pp. 1000-1003, 2008.

[55] D. Nieuwenhove et al., "A CAPD based Time-of-Flight ranging pixel with wide dynamic range," *Proc. SPIE 7000, Optical and Digital Image Processing,* 2008.

[56] G.-F. Dalla Betta and Q. D. Hossain et al., "TOF-Range Image Sensor in 0.18µm CMOS technology based on Current Assisted Photonic Demodulators," *OSA/ CLEO 2011,* p. 2, 2011.

[57] R. Seitz and P. Lange, "Solid-State Time-of-Flight Range Camera," *IEEE Journal Of Quantum Electronics,* vol. 37, no. 3, p. 8, 2001.

[58] S. Microelectronics, "http://www.st.com/web/en/resource/technical/document/datasheet/DM00112632.pdf," 2014. [Online].

[59] M. Drader et.al., "Device having SPAD Photodiodes for Detecting an Object". Patent US20130153754 A1, 20 6 2013.

[60] Wikipedia, "LG G3," [Online]. Available: https://en.wikipedia.org/wiki/LG_G3. [Accessed 31 8 2015].

[61] Pmdtechnologies, "pmdtec.com," 2014. [Online]. Available: http://www.pmdtec.com/html/pdf/PMD_RD_Brief_CB_pico_71.19k_V0103.pdf.

[62] A. Infineon Technologies, "Infineon 3D Image Sensor IRS1010C," 5 2013. [Online]. Available: http://www.infineon.com/dgdl/3D+Image+Sensor+IRS10x0C_PB_final_v2.pdf?fileId=db3a30433e82b1cf013e847e27e703e9.

[63] "Cayim," [Online]. Available: https://www.cayim.com/. [Accessed 1 9 2015].

[64] Wikipedia, "Lux," [Online]. Available: https://en.wikipedia.org/wiki/Lux. [Accessed 1 9 2015].

[65] Wikipedia, "Laserdiode," [Online]. Available: https://de.wikipedia.org/wiki/Laserdiode. [Accessed 2 9 2015].

[66] D. Piatti and F. Rinaudo, "SR-4000 and CamCube3.0 Time of Flight (ToF) Cameras: Tests and Comparison," *Remote Sensing,* pp. 1069-1089, 2012.

[67] L. Szilágyi et al., "A High-voltage DC Bias Architecture Implementation in a 17 Gbps Low-power Common-cathode VCSEL Driver in 80 nm CMOS," Circuits and Systems (ISCAS), IEEE International Symposium, Lisbon, 2015.

[68] T. Yazaki et al., "25-Gbps×4 optical transmitter with adjustable asymmetric pre-emphasis in 65-nm CMOS," Circuits and Systems (ISCAS), IEEE International Symposium , Melbourne VIC , 2014.

[69] N. Chujo et al., "A 25 Gb/s 65-nm CMOS Low-Power Laser Diode Driver With Mutually Coupled Peaking Inductors for Optical Interconnects," *Circuits and Systems I: Regular Papers, IEEE Transactions,* vol. 58, no. 9, pp. 2061 - 2068 , 2011.

[70] S. Palermo et al., "A 90 nm CMOS 16 Gb/s Transceiver for Optical Interconnects," *Solid-State Circuits Conference, 2007. ISSCC 2007. Digest of Technical Papers. IEEE International ,* pp. 44 - 586, 2007.

[71] C. Kromer et al., "A 100-mW 4x10 Gb/s Transceiver in 80-nm CMOS," IEEE J. Solid-State Circuits, 2005.

[72] J. Proesel, C. Schow and A. Rylyakov, "25Gb/s 3.6pJ/b and 15Gb/s 1.37pJ/b VCSEL-Based Optical Links in 90nm CMOS," ISSCC 2012 / Session 24 / 10GBase-T & Optical Frontends / 24.5, 2012.

[73] D. Zhou et al., "Progress on vertical-cavity surface-emitting laser arrays for infrared illumination applications," SPIE Proceedings Vol. 9001, 2014.

[74] Vixar, "Vixar High Power Array Technology," [Online]. Available: http://vixarinc.com/wp-content/uploads/Vixar-High-Power-Array-Technology-rev-2.pdf. [Accessed 7 9 2015].

[75] G. Overton, "LaserFocusWorld," [Online]. Available: http://www.laserfocusworld.com/articles/print/volume-49/issue-08/world-news/vcsel-illumination-high-power-vcsels-rule-ir-illumination.html. [Accessed 4 9 2015].

[76] Markettech, "Overview of Modulated and Pulsed Diode Laser," [Online]. Available: http://www.markettechinc.net/pdf/Diode%20Laser%20Application%20Note.pdf. [Accessed 11 9 2015].

[77] G. Javanovic and M. Stojcev, "Verniers Delay Line TDC," University of Novi Pazar, 2009.

[78] P. Kumar, *Time-of-Flight 3D Imaging based on a SPAD-TDC Pixel Array in Standard 65 nm CMOS Technology,* Master Thesis: Delft University of Technology, 2011.

[79] L. Vercesi et al., "Two-Dimensions Vernier Time-to-Digital Converter," *Solid-State Circuits, IEEE Journal ,* vol. 45, no. 8, pp. 1504 - 1512 , 2010.

[80] A. Yousif and J. W. Haslett, "A Fine Resolution TDC Architecture for Next Generation PET Imaging," *Nuclear Science, IEEE Transactions,* vol. 54, no. 5, pp. 1574 - 1582 , 2007.

[81] M. Gersbach et al., "A Parallel 32x32 Time-to-Digital Converter Array Fabricated in a 130nm Imaging CMOS Technology," ESSCIRC, Athens, 2009.

[82] J. Richardson et al., "A 32x32 50ps Resolution 10 bit Time to Digital Converter Array in 130nm CMOS for Time Correlated Imaging.," IEEE 2009 Custom Intergrated Circuits Conference (CICC), San Jose, CA , 2009.

[83] D. Stoppa et al., "Ultra Compact and Low-power TDC and TAC Architectures for Highly-Parallel Implementation in Time-Resolved Image Sensors," in *International Workshop on ADC Modelling,Testing and Data Converter Analysis and Design and IEEE ADC Forum*, Orvieto, Italy, 2011.

[84] I. Vornicu et al., "CMOS 0.18μm 64×64 Single Photon Image Sensor with In-Pixel 11b Time-to-Digital Converter," Semiconductor Conference (CAS), Sinaia , 2014.

[85] C. Favi, *Single-Photon Techniques for Standard CMOS Digital ICs,* EPFL, Lausanne, 2011.

[86] E. Charbon, *SPAD Pixel Detectors with High Time Resolution,* TU Delft.

[87] C. Niclass, M. Sergio and E. Charbon, "A Single Photon Avalanche Diode Array Fabricated in 0.35μm CMOS and based on an Event-Driven Readout for TCSPC Experiments," in *SPIE Optics East*, Boston, 2006.

[88] C. Niclass and E. Charbon, "A Single Photon Detector Array with 64×64 Resolution and Millimetric Depth Accuracy for 3D Imaging," in *Solid-State Circuits Conference, 2005. Digest of Technical Papers. ISSCC*, San Francisco, CA, 2005.

[89] N. Azemard and L. Svensson, Integrated Circuit and System Design. Power and Timing Modeling, Optimization and Simulation, 7th International Workshop, PATMOS 2007, Gothenburg: Springer Science & Business Media, 2007.

[90] M. S. University, "Electromagnetics Research Group," [Online]. Available: http://www.egr.msu.edu/em/research/goali/notes/module3_signals_and_spectra.pdf. [Accessed 3 12 2015].

[91] T. Williams, EMC for Product Designers: Meeting the European EMC Directive, Butterworth-Heinemann Ltd, 1992.

[92] S. Jha, Cayenne Consulting, [Online]. Available: http://www.caycon.com/blog/2014/05/price-your-product-to-capture-the-value-you-create/. [Accessed 22 9 2015].

[93] G. s. Alliance, "4Q14 Wafer fabrication pricing executive summary," www.gsaglobal.org, 2014.

[94] D. De Vries, "Investigation of Gross Die Per Wafer Formulas," *Semiconductor Manufacturing, IEEE Transactions,* vol. 18, no. 1, p. 4, 2005.

[95] S. Edge, "Die Per Wafer Estimator," [Online]. Available: http://www.silicon-edge.co.uk/j/index.php/resources/die-per-wafer. [Accessed 13 9 2015].

[96] E. Wein and J. Benkoski, "Hard Macros will revolutionize SoC Design," EE times, [Online]. Available: http://www.design-reuse.com/articles/8513/hard-macros-will-revolutionize-soc-design.html. [Accessed 13 9 2015].

[97] J. Lien, M. Hong and J. Shen, "TSMC shifts to 8-inch processing to produce fingerprint sensors for next-generation iPhone," DigiTimes, [Online]. Available: http://www.digitimes.com/news/a20140211PD207.html. [Accessed 13 9 2015].

[98] J. Hruska, "Extremtech," [Online]. Available: http://www.extremetech.com/extreme/163372-atom-everywhere-intel-breaks-ground-on-first-450mm-fab. [Accessed 15 9 2015].

[99] O. C. Ferrell and M. Hartline, Marketing Strategy, South Western, 2014.

[100] I. Kalb, "Business Insider," Marshall School of Business, USC, [Online]. Available: http://www.businessinsider.com/3-powerful-pricing-strategies-businesses-should-always-consider-2013-10?IR=T. [Accessed 15 9 2015].

[101] "Investopedia," [Online]. Available: http://www.investopedia.com/terms/c/cogs.asp. [Accessed 15 9 2015].

[102] J. Pinto. [Online]. Available: http://www.jimpinto.com/writings/priceparadigms.html. [Accessed 2015 9 15].

[103] C. L. Niclass, "Single-Photon Image Sensors in CMOS Picosecond Resolution for Three-Dimensional Imaging," 2008.

[104] M. W. Fishburn, "Fundamentals of CMOS Single-Photon Avalanche Diodes," 17 Semptember 2012. [Online]. Available: http://books.google.com/. [Accessed 10 April 2015].

[105] T. I. Incorporated, *LIDAR System Design for Automotive/Industrial/Military Applications,* 2011.

[106] P. Kumar, E. Charbon, R. B. Staszewski and A. Borowski, "Low Power Time-of-Flight 3D Imager System in Standard CMOS," Delft University of Technology, Delft, 2012.

[107] "Michigan State University," [Online]. Available: http://www.egr.msu.edu/em/research/goali/notes/module3_signals_and_spectra.pdf. [Accessed 27 08 2015].

[108] N. G. Einspruch, VLSI Electronics: Microstructure Science, New York: Academic Press, 1982.

[109] A. v. Beringe, *Performance evaluation of a Range Camera SR4000,* Vienna: University of Technology Vienna, 2012.

[110] "Halbleitertechnologie von A bis Z," [Online]. Available: http://www.halbleiter.org/waferherstellung/wafer/. [Accessed 13 9 2015].

[111] E. Webster et al., "A Single-Photon Avalanche Diode in 90-nm CMOS Imaging Technology With 44% Photon Detection Efficiency at 690 nm," *IEEE Electron Device Letters,* vol. VOL. 33, p. 3, 2012.

[112] S. Han et al., "A 413×240-Pixel Sub-Centimeter Resolution Time-of-Flight CMOS Image Sensor with In-Pixel Background Canceling Using Lateral-Electric-Field Charge Modulators," *ISSCC 2014 / Session 7 / Image Sensors / 7.4,* p. 3, 2014.